

OPTICAL PROPERTIES OF THIN  
BARRIER GaAs-Al<sub>x</sub>Ga<sub>1-x</sub>As  
SUPERLATTICES

By

JOHN MATTHEW JACOB

Bachelor of Arts

Hendrix College

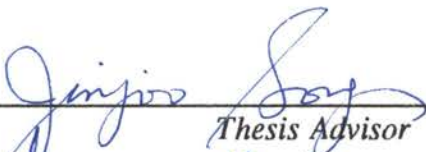
Conway, Arkansas


1987


Submitted to the Faculty of the  
Graduate College of the  
Oklahoma State University  
in partial fulfillment of  
the requirements for  
the Degree of  
DOCTOR OF PHILOSOPHY  
July, 1993


OPTICAL PROPERTIES OF THIN  
BARRIER GaAs-Al<sub>x</sub>Ga<sub>1-x</sub>As  
SUPERLATTICES


Thesis Approved:

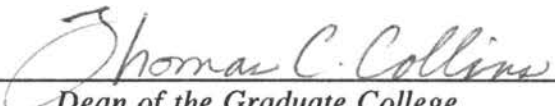
  
\_\_\_\_\_  
*Thesis Advisor*

  
\_\_\_\_\_

  
\_\_\_\_\_

  
\_\_\_\_\_

  
\_\_\_\_\_

  
\_\_\_\_\_  
*Dean of the Graduate College*

## PREFACE

Optical properties of thin barrier GaAs/Al<sub>x</sub>Ga<sub>1-x</sub> superlattices are investigated with tunable laser spectroscopy. In chapter I, basic concepts in superlattice physics emphasizing the unique features of coupled quantum well structures (superlattices) is presented. In addition a comprehensive introduction to the origins of optical spectra in superlattices is discussed. Chapter II treats the inhomogeneous broadening of optical spectra caused by random structural disorder. The effects that well-to-well coupling in a superlattice has on the broadening of excitonic transitions is the emphasis of this chapter. A multiple scattering theory based on a Greens function technique is presented to support experimental findings. Chapter III discusses several effects of the unique subband properties of superlattices using a variety of spectroscopic techniques. Chapter IV treats hot carrier relaxation in Al<sub>x</sub>Ga<sub>1-x</sub>As alloys as investigated by picosecond Raman spectroscopy. Finally, chapter V concludes this thesis with a summary of results.

There are many people who have played an important role in the completion and success of this thesis. I am especially grateful to my thesis advisor, Dr. Jin-Joo Song for giving me the great opportunity to work in her laboratory. I deeply appreciate her guidance, patience and support through the duration of this work. I am also indebted to her for the concerns of finding me the best possible job prospects, of which I could not possibly obtain on my own. I would also like to acknowledge the

members of my thesis committee, Dr. George Dixon, Dr. Bob Hauenstein, Dr. Xin-Cheng Xie, and Dr. Jerzy Krasinski. I appreciate their careful review of all my work as well as insightful discussions.

I wish to acknowledge Dr. Charles W. Tu at the University of California, San Diego for providing me with the superlattice and alloy samples used in this thesis work. In addition I am grateful to Dr. H. Morkoç at the University of Illinois, Urbana for also providing some of the alloy samples studied. I wish to acknowledge Dr. Y.C. Chang at the University of Illinois, Urbana for his theoretical support on the exciton line narrowing work. I acknowledge Dr. Dai-Sik Kim for his invaluable aid on the hot phonon work in this thesis. This chapter would have never existed in my thesis without his diligence and hard work. I am also thankful of Dr. Jin Fu Zhou, who worked with me closely for several years. He has been a good friend and teacher. I would like to thank Dr. P.S. Jung and Seon-ju Hwang for use of some of the figures in this thesis.

I am grateful to the physics department, Dr. Song, the Office of Naval research, Oklahoma Center for the Advancement of Science and Technology, and the United States Department of Education for providing all of the financial support during my six years of graduate studies at Oklahoma State University.

I would like to acknowledge Dr. Richard Rolleigh, chairman of physics at Hendrix College. He was largely responsible for my decision to pursue a doctorate in physics. He has always been my mentor, and I view him as a true master of academic sciences and the art of teaching.

Most of all I wish to acknowledge my family for all of their loving support. My parents Roy and Gerri Jacob have always stood behind my decisions, given me invaluable guidance and instruction, and aided me to the best of their abilities. My older brother Paul, and sister Debbie have always put my needs before theirs. Last but not least, my twin sister Jane who is a large part of my happiness. My family has always been the primary source of my motivation and has given me the necessary encouragement to pursue all of my college degrees.

There are many close friends which have been a great source of entertainment, relaxation, and encouragement. I will always cherish the times we had together and look forward to future reunions. Above all I wish to acknowledge my best friend and Great Dane, Jude, the Gentle Giant. My thesis is dedicated to this four-legged beast.

## TABLE OF CONTENTS

Chapter		Page
I.	INTRODUCTION .....	1
	Crystal Structure .....	2
	Electronic Band Structure .....	6
	Superlattice Subband Properties .....	11
	Excitons in Superlattices .....	19
	Optical Spectra in GaAs/Al <sub>x</sub> Ga <sub>1-x</sub> As Superlattices .....	23
II.	EXCITON LINE NARROWING IN THIN BARRIER SUPERLATTICES .....	25
	Interface Roughness .....	25
	Experimental Setup .....	33
	Experimental Results .....	36
	Exciton Linewidth Theory .....	40
	Results and Discussion .....	54
III.	MULTIPLE RESONANT RAMAN SCATTERING AND FANO-TYPE RESONANCES IN THIN BARRIER SUPERLATTICES .....	59
	Optical Phonons in Superlattices .....	61
	Electron Phonon Interactions .....	64
	Raman Tensors and Selection Rules .....	67
	Experiment and Results .....	72
	Discussion .....	87



## LIST OF TABLES

Table	Page
I. Character table for point group $T_d$ .....	3
II. Character table for point group $D_{2d}$ .....	3
III. Band structure parameters in $Al_xGa_{1-x}As$ .....	10
IV. Dye laser performance record .....	35
V. Subband energy properties .....	36
VI. Raman backscattering selection rules .....	69
VII. Alloy samples .....	110



## LIST OF FIGURES

Figure	Page
1. Bravais lattice for zinc-blende and superlattice structures .....	4
2. Brillouin zones for zinc-blende and superlattice structures .....	5
3. Energy band structure for GaAs .....	7
4. Schematics of a multiple square well potential .....	9
5. Critical points in the band structure of solids .....	13
6. Density of states in 2D and 3D systems .....	14
7. Wavefunction amplitudes in quantum wells and superlattices .....	15
8. Conduction subband structure in superlattice .....	17
9. Subband width versus well and barrier widths .....	18
10. Quantum well exciton binding energy versus well widths .....	21
11. Theoretical and experimental optical spectra in Al <sub>x</sub> Ga <sub>1-x</sub> As superlattices .....	24
12. Interlayer and Intralayer fluctuations in quantum well structures .....	27
13. Interface roughness and the corresponding luminescence spectra .....	30
14. Experimental PL and PLE set-up .....	34
15. PL spectra from a series of superlattices .....	38
16. PLE spectra from a series of superlattices .....	39

Figure	Page
17. Diagram representations of Green's functions and Self Energies .....	46
18. Numerical solution for Coherent Potential Approximation applied to exciton line narrowing in superlattices .....	53
19. Experimental and theoretical FWHM of exciton lineshapes .....	55
20. Experimental and theoretical FWHM of exciton lineshapes .....	56
21. Bulk GaAs and AlAs optic phonon dispersion .....	62
22. Comparison of PL and PLE in a thin barrier superlattice .....	75
23. 1 LO phonon assisted PL and PLE .....	78
24. 2 optic phonon assisted PL and PLE .....	79
25. First order doubly resonant Raman profile .....	80
26. 1HH and 1LH exciton intensities versus the barrier width .....	83
27. Multiple resonant Raman spectra .....	85
28. Phonon assisted PLE .....	86
29. Calculated subband structure of thin barrier superlattice .....	88
30. Schematics of multiple scattering process .....	89
31. Triply resonant Raman profile .....	94
32. Gamma valley excess energy of photoexcited carriers .....	100
33. Hot LO phonon occupation versus phonon wavenumber .....	103
34. Experimental hot phonon set-up .....	107
35. Excess energy of 2.33eV photoexcited electrons versus alloy composition .....	109
36. Picosecond Raman spectra .....	112

Figure	Page
37. Hot phonon occupation versus laser power .....	114
38. Hot phonon generation efficiency versus alloy composition .....	115
39. Schematic diagram of hot phonon generation in GaAs .....	118
40. Schematic diagram of hot phonon generation in $\text{Al}_{0.39}\text{Ga}_{0.61}\text{As}$ .....	119

## CHAPTER I

### INTRODUCTION

The group III-V binary semiconductor crystals GaAs and AlAs, together with their ternary  $\text{Al}_x\text{Ga}_{1-x}\text{As}$  alloy compound, form one of the most widely studied quantum well structures, namely GaAs/ $\text{Al}_x\text{Ga}_{1-x}\text{As}$  superlattices. The advent of molecular beam epitaxy (MBE) has advanced crystal growth techniques into producing high quality semiconductor structures grown by alternating layers [1]. These ultrathin layers in superlattices grown along the [001] crystal axis contain two sublayers of Ga (Al) or As totaling one-half of the bulk lattice constant. It was first proposed by Esaki and Tsu in 1970, that alternating ultrathin layers of two semiconductors with significantly different energy bandgaps (such as GaAs and AlAs) would lead to two-dimensional (2D) quantum well (QW) structures [2]. Since then a great amount of attention has been given to the study of these heterostructures to investigate the underlying physics and to explore potential device applications in such areas as electro-optics and photonics [1,3,4]. Most of the traditional studies in this area have concentrated on single QW or multiple QW structures separated by thick barriers. However, with the accumulation of QW studies and improved sample quality much interest has been with the multiple-coupled quantum well structure commonly referred to as the superlattice (SL).

## Crystal Structure

The Bravais lattice cell of both GaAs and AlAs is zinc-blende structure as shown in figure 1(a), with a lattice constant  $a \approx 5.6 \text{ \AA}$ . When these two semiconductors form a  $(\text{GaAs})_m/(\text{AlAs})_n$  superlattice, the Bravais lattice will contain one or two unit cells. The choice depends on the number of monolayers  $m$  and  $n$  in the superlattice period,  $d = (m + n) a/2$ . The unit cell of the Bravais lattice is simple tetragonal if  $m + n$  is even and is body-centered tetragonal if  $m + n$  is odd as shown in figure 1(b). The corresponding Brillouin zones for a  $(\text{GaAs})_m/(\text{AlAs})_n$  superlattice are shown in figure 2, together with the Brillouin zone for bulk III-V zinc-blende structures. The bulk crystals have cubic ( $T_d$ ) symmetry which is lowered to tetragonal symmetry ( $D_{2d}$ ) for superlattice structures caused by the new periodicity along the superlattice growth direction. The group theory character tables for  $T_d$  and  $D_{2d}$  point group symmetries, are given in table I and table II [5]. These are fundamental in determining physical properties in the semiconductor as determined from experiments such as Raman spectroscopy.

TABLE I  
CHARACTER TABLE FOR POINT GROUP  $T_d$

		E	$8C_3$	$3C_2$	$6\sigma_d$	$6S_4$
$(R_x, R_y, R_z)$ $(x, y, z)$	$A_1$	1	1	1	1	1
	$A_2$	1	1	1	-1	-1
	E	2	-1	2	0	0
	$T_1$	3	0	-1	-1	1
	$T_2$	3	0	-1	1	-1

TABLE II  
CHARACTER TABLE FOR POINT GROUP  $D_{2d}$

			E	$C_2$	$2S_4$	$2C'_2$	$2\sigma_d$
$x^2 + y^2$ $z^2$		$A_1$	1	1	1	1	1
	$R_z$	$A_2$	1	1	1	-1	-1
$x^2 - y^2$		$B_1$	1	1	-1	1	-1
xy	z	$B_2$	1	1	-1	-1	1
$(xz, yz)$	$(x, y)$ $(R_x, R_y)$	E	2	-2	0	0	0

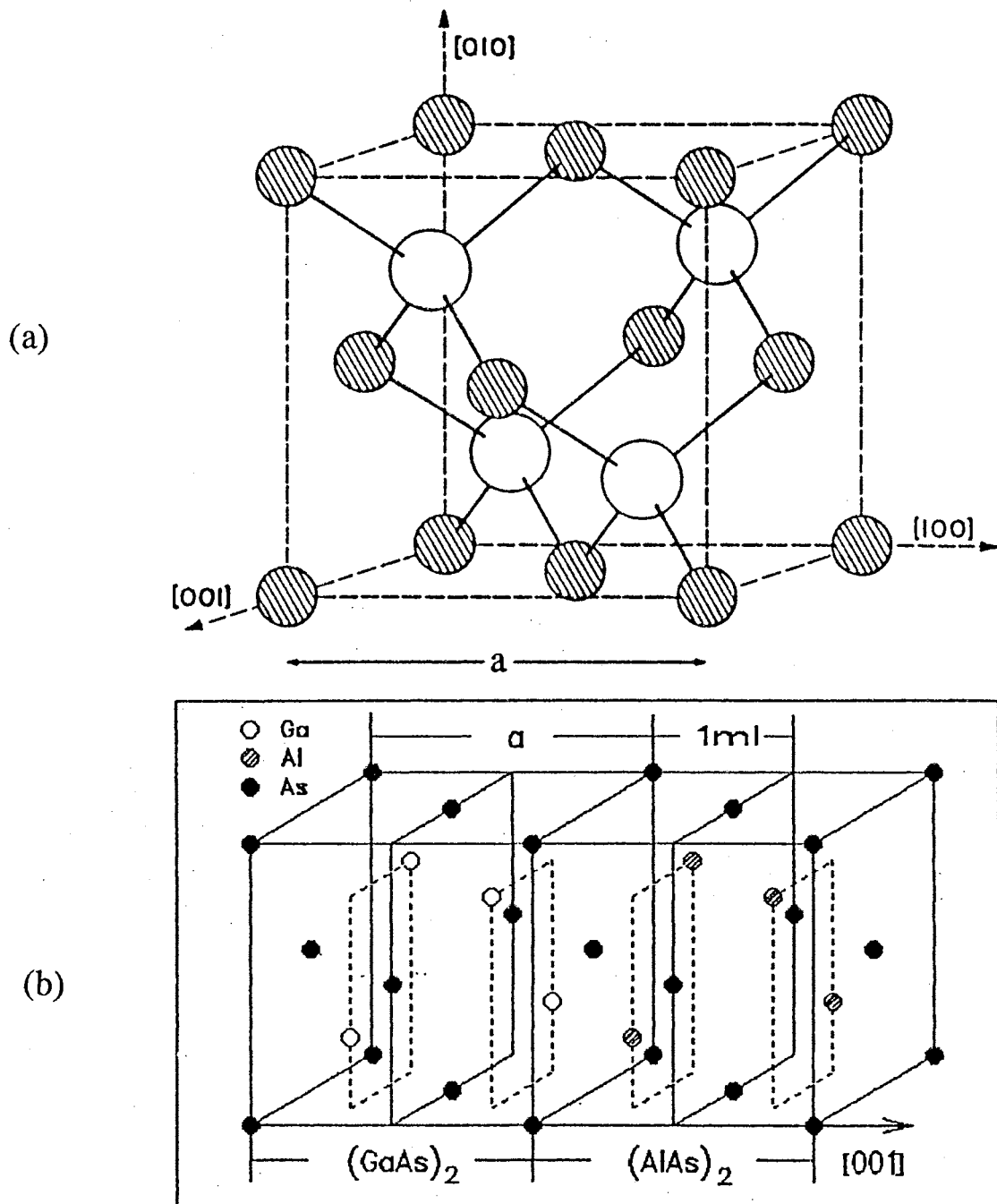


Figure 1. The Bravais lattice unit cell for (a) bulk GaAs or AlAs and (b) GaAs/Al<sub>x</sub>Ga<sub>1-x</sub>As superlattices. In (a) the unit cell has zinc-blende structure, whereas in (b) it is simple tetragonal for  $m+n$  even and body-centered tetragonal for  $m+n$  odd.

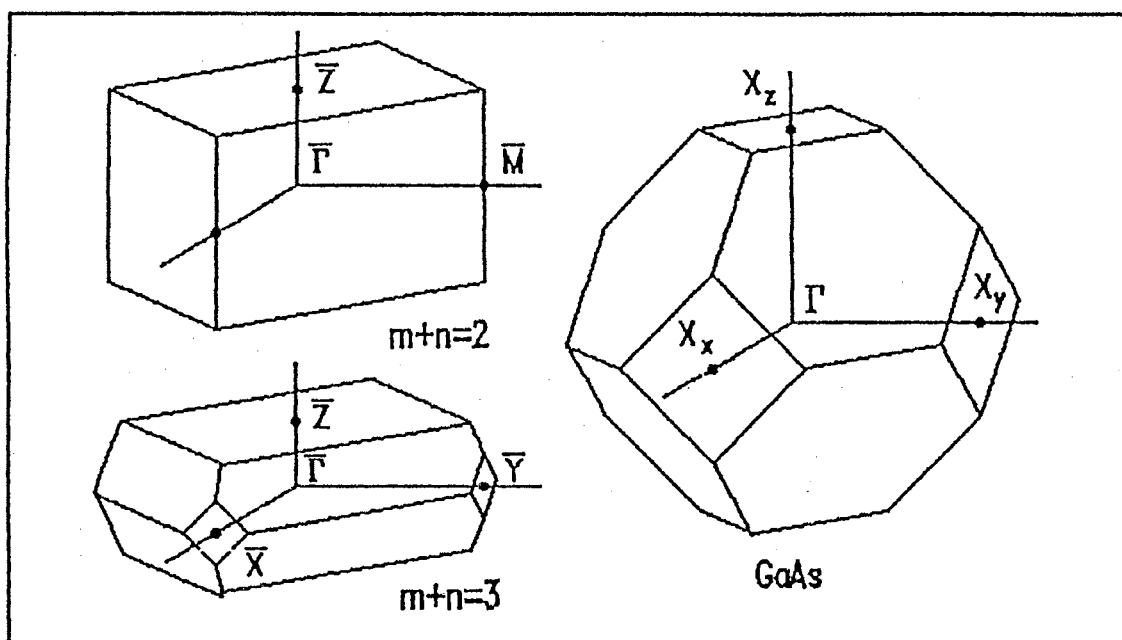


Figure 2. First Brillouin zones (Wigner-Seitz cell) of bulk zinc-blende and superlattice structures.



## Electronic Band Structure

The calculated energy band structure along the [100] and [111] directions in bulk GaAs is shown in figure 3. The curvature of band structures near points of high symmetry makes these points important in the optical studies of semiconductors. The first conduction band in GaAs consists of three valleys with minima at the high symmetry points given by;

$$\begin{aligned}
 \Gamma_{6c} \text{ point} \rightarrow \vec{k} &= (0, 0, 0) \frac{\pi}{a} \\
 X_{6c} \text{ point} \rightarrow \vec{k} &= (1, 0, 0) \frac{\pi}{a} \\
 L_{6c} \text{ point} \rightarrow \vec{k} &= (1, 1, 1) \frac{\pi}{a}
 \end{aligned} \tag{1}$$

The valleys denoted by these points are subsequently named  $\Gamma$ , X, and L valleys. The first valence band minima at the  $\Gamma_{8v}$  point is fourfold degenerate between the light-holes (LH) and heavy-holes (HH). The conduction band edge in GaAs is s-like with angular momentum states given by  $j = 1/2$ ,  $m_j = \pm 1/2$ . The degenerate valence band has angular momentum given by  $j = 3/2$ ,  $m_j = \pm 1/2$  for light-holes and  $m_j = \pm 3/2$  for heavy-holes. The degeneracy between the light- and heavy-hole states is lifted for  $k \neq 0$  by spin-orbit interactions.

When alternating ultra-thin layers of GaAs and  $\text{Al}_x\text{Ga}_{1-x}\text{As}$  are formed along the [001] growth direction, the energy bands of the heterostructure resemble that of a multiple finite square well potential as shown in figure 4. This quantum well formation lifts the valence band degeneracy at  $k = 0$  and quantizes the angular

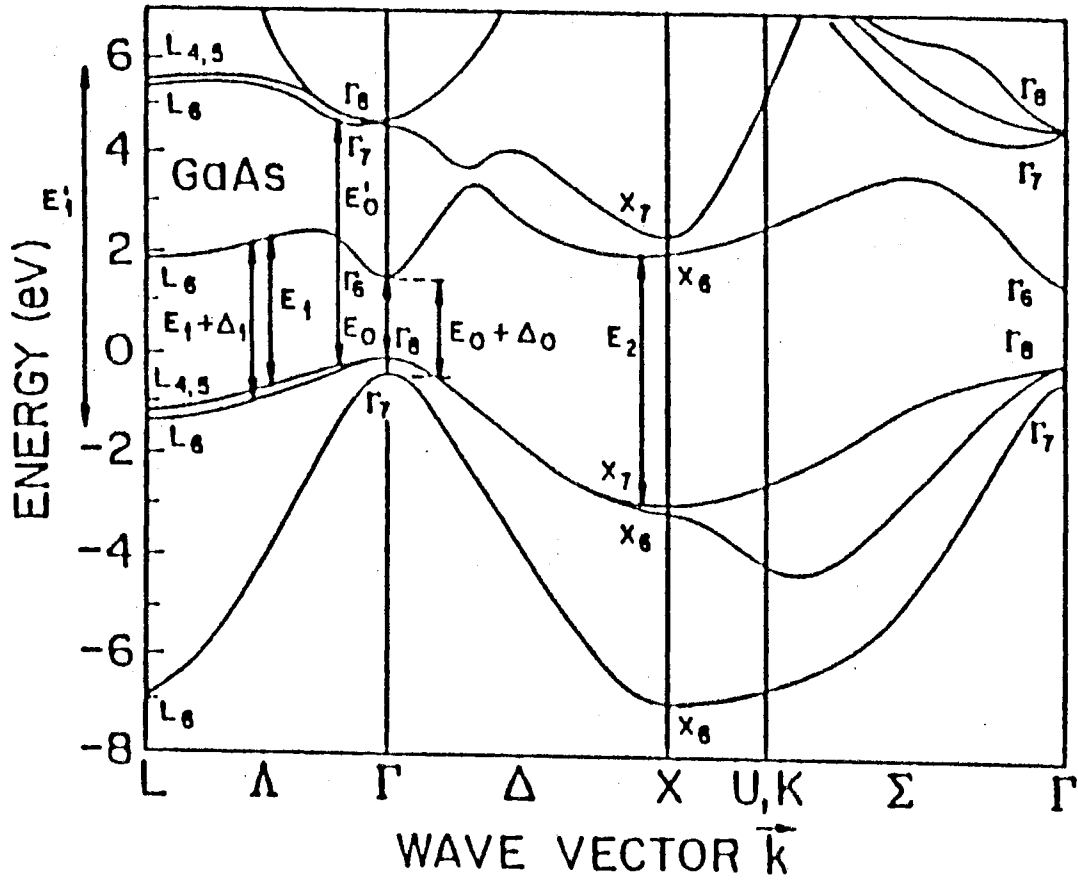


Figure 3. Energy band structure and symmetry points in GaAs.

momenta of the bands along the [001] superlattice axis [4]. The potential barrier heights of a GaAs/Al<sub>x</sub>Ga<sub>1-x</sub>As superlattice depends on the energy difference in the fundamental band gap of the two bulk materials. There are various forms of the energy band gaps in Al<sub>x</sub>Ga<sub>1-x</sub>As with respect to the Al concentration  $x$  which can be found in the literature. Those used in this thesis are listed in table III [6,7].

The difference between GaAs and Al<sub>x</sub>Ga<sub>1-x</sub>As band gaps does not evenly divide into the conduction and valence band barrier heights. The ratio of the difference between the conduction and valence band barrier heights is referred to as the valence band offset ratio. This ratio is often chosen between 65/35 and 70/30 for GaAs/Al<sub>x</sub>Ga<sub>1-x</sub>As superlattices. That is 65% of the difference between GaAs and Al<sub>x</sub>Ga<sub>1-x</sub>As band gap energies defines the conduction band barrier height. Al<sub>x</sub>Ga<sub>1-x</sub>As is a direct-gap semiconductor for  $x < \approx 0.45$  and the corresponding GaAs/Al<sub>x</sub>Ga<sub>1-x</sub>As superlattice is defined as a type I superlattice.

One of the most fundamental properties of quantum well (QW) structures is the spatial confinement of particles and quasiparticles (e.g. electrons, holes, excitons, phonons). In MQW's the sample parameters which influence confinement the most are the QW width ( $L_z$ ) and the barrier height, which is related to the Al concentration. However, when the barrier width ( $L_b$ ) becomes small, coupling between particles of adjacent QW's exists. Therefore in SL structures  $L_b$  is also an important parameter in the confinement of particles. The electronic confinement leads to a varying degree of energy band structures in superlattices. The ability to engineer electronic band structures in solids is an important issue in device

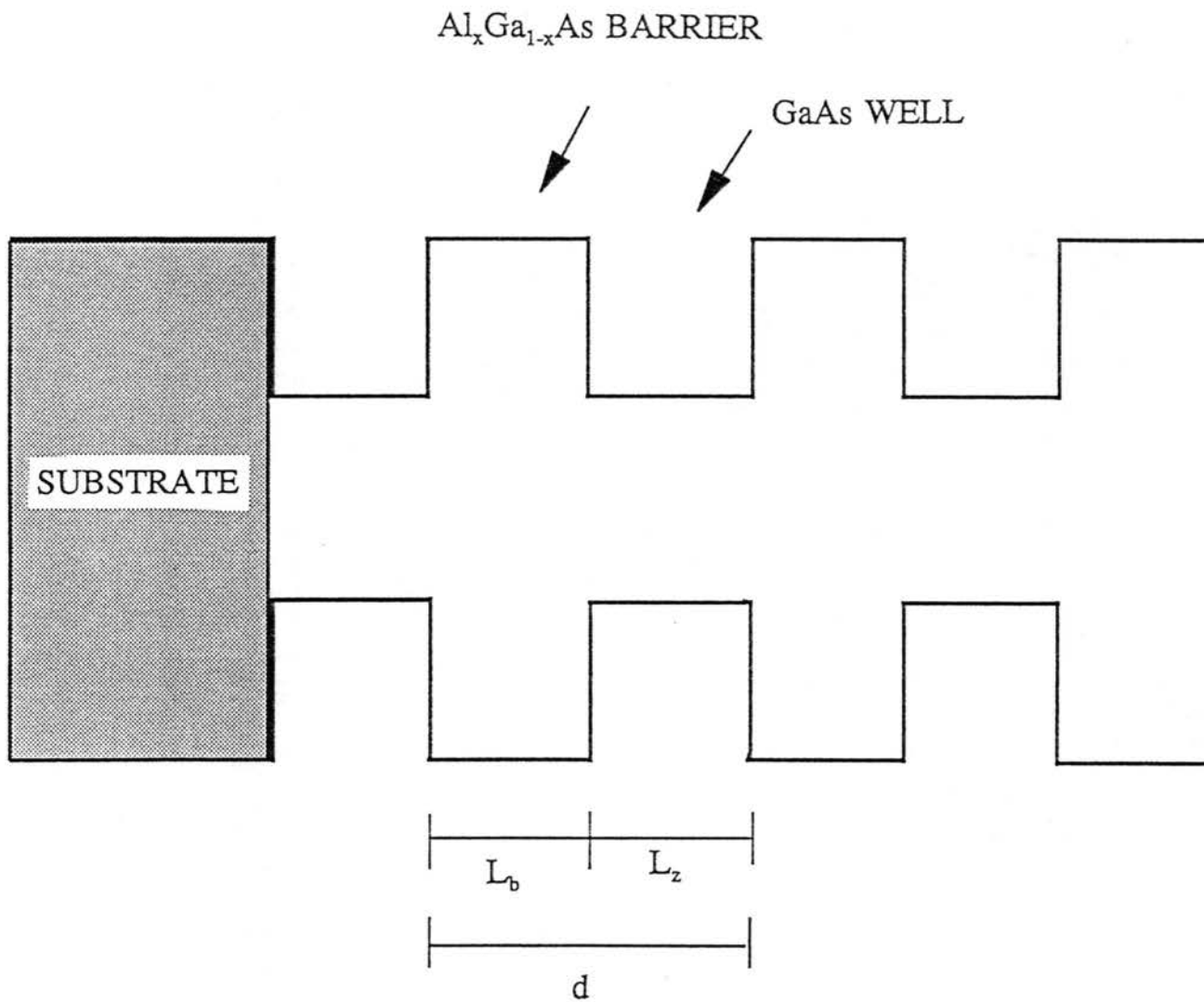


Figure 4. Schematics of the finite square well potential in semiconductor superlattices.

TABLE III  
BAND STRUCTURE PARAMETERS IN  $\text{Al}_x\text{Ga}_{1-x}\text{As}$

$E_g(\Gamma)$	$1.519 + 1.247x$	$T = 5\text{K}$
$E_g(\text{X})$	$1.995 + 0.125x + 0.143x^2$	$x < 0.45$
$E_g(\text{L})$	$1.803 + 0.642x$	
$x_c(\text{L-X})$	0.35	crossover of X and L bands
$x_c(\Gamma\text{-X})$	0.405	crossover of $\Gamma$ and X bands
$x_c(\Gamma\text{-L})$	0.432	crossover of $\Gamma$ and L bands
$m_n$	$0.067 + 0.083x$	density of states mass, $\Gamma$
	$0.85 - 0.14x$	density of states mass, X
	$0.56 + 0.1x$	density of states mass, L
$m_{p,h}$	$0.62 + 0.14x$	density of states mass, HH
$m_{p,l}$	$0.087 + 0.063x$	density of states mass, LH
$m_{soh}$	$0.15 + 0.09x$	density of states mass, SOH

technology, thus making superlattice structures good candidates for many potential applications [1,3,8].

The main differences between MQW and SL structures arise because of well-to-well coupling. To understand the importance of coupling consider the following simple example of electrons in QW's. The growth of a QW structure spatially confines the electrons in one of three dimensions, usually taken to be the z-direction. If the confinement scale ( $L_z$ ) is less than the mean free path, size quantization will occur. For QW's with infinite barriers the quantization results in two dimensional (2D) properties of the electrons. This may be seen in the following equations for the energy of an electron in a semiconductor quantum well [9].

$$E(\vec{k}) = \frac{\hbar^2}{2m^*} (k_x^2 + k_y^2 + k_z^2) \quad (2)$$

$$k_z = \frac{n\pi}{L_z}$$

$E_n$  represents the discrete energy levels originating from size quantization along the z-direction. The parabolic terms,  $k_x$  and  $k_y$  are similar to those in bulk semiconductors, and reveal the 2D freedom of electrons in QW's.

The joint density of states (DOS) between conduction and valence bands in a solid is defined as;

$$DOS \propto \int \frac{dE}{\nabla_k [E_c(\vec{k}) - E_v(\vec{k})]} \quad (3)$$

where  $E(\mathbf{k})$  denotes the band dispersion. Singularities in the DOS function (critical

points) often lead to the origins of optical spectra in semiconductors. The four types of critical points studied in solids are shown in figure 5. The DOS for bulk and superlattice structures are shown in figure 6. The 2D step-like function corresponds to QW structures and the parabolic density of states symbolizes the 3D freedom of electrons in bulk semiconductors. An effect of well-to-well coupling in the SL is to smoothen the sharp step-like features of the QW density of states as shown in figure 6. This results in many new and interesting features unique only to the coupling in superlattice structures. In addition to the  $M_0$ -type critical point which exists in QW and bulk structures, the SL subband structure also gives rise to  $M_1$ -type (saddle-point) critical points in the DOS function.

In real QW structures which are subject to experiments, the potential barriers are finite in height which influences the degree of electronic confinement. One effect is to limit the number of quantized energy levels bound to the quantum well [10]. The finite barrier height also allows for penetration of electronic wavefunctions into the barrier region, which lowers the quantized energy levels  $E_n$ . In a SL, the  $L_b$ 's are thin enough to allow electronic wavefunctions confined in adjacent wells to penetrate through the barriers and couple to one another. This is illustrated in the calculation of the wavefunction amplitudes for the  $n=1$  light- and heavy-holes in GaAs/ $Al_{0.3}Ga_{0.7}As$  QW structures shown in figure 7. The most pronounced effects of well-to-well coupling may be seen in the origins of subband dispersion as well as tunneling phenomena along the  $z$ -direction.

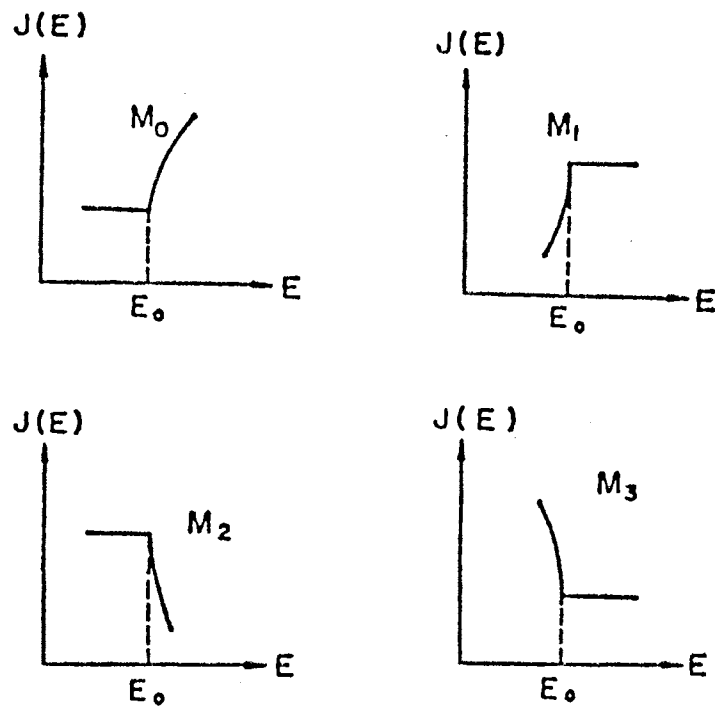


Figure 5. Various types of critical points occurring in band structure of solids.



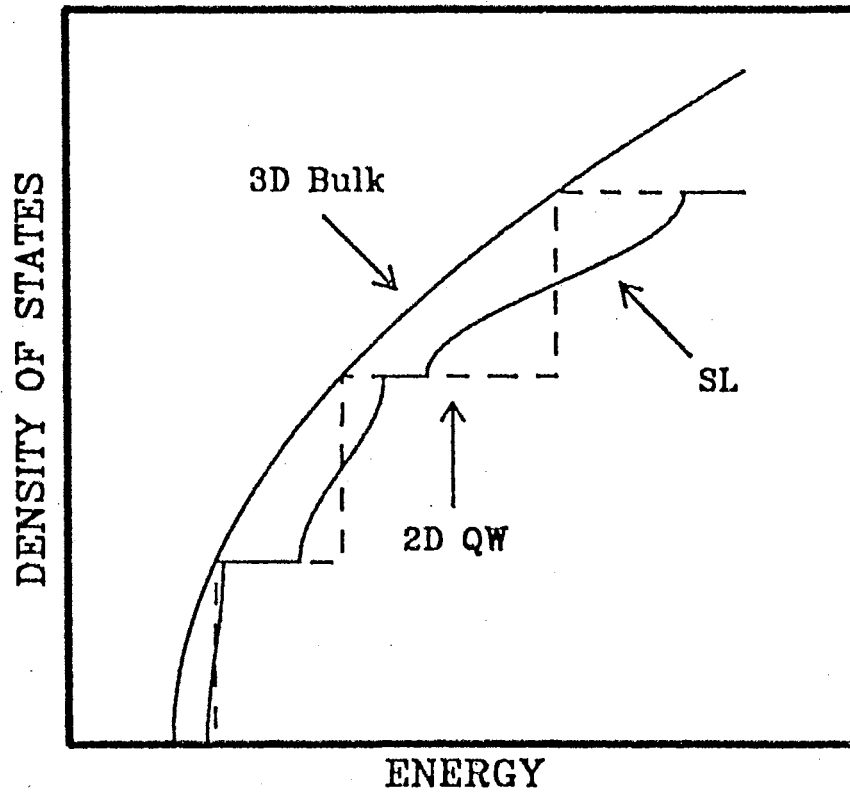


Figure 6. Schematic representation of the density of states in bulk, QW, and SL semiconductor structures. The effect of well-to-well coupling in the SL smooths out the sharp step-like features in the QW density of states.

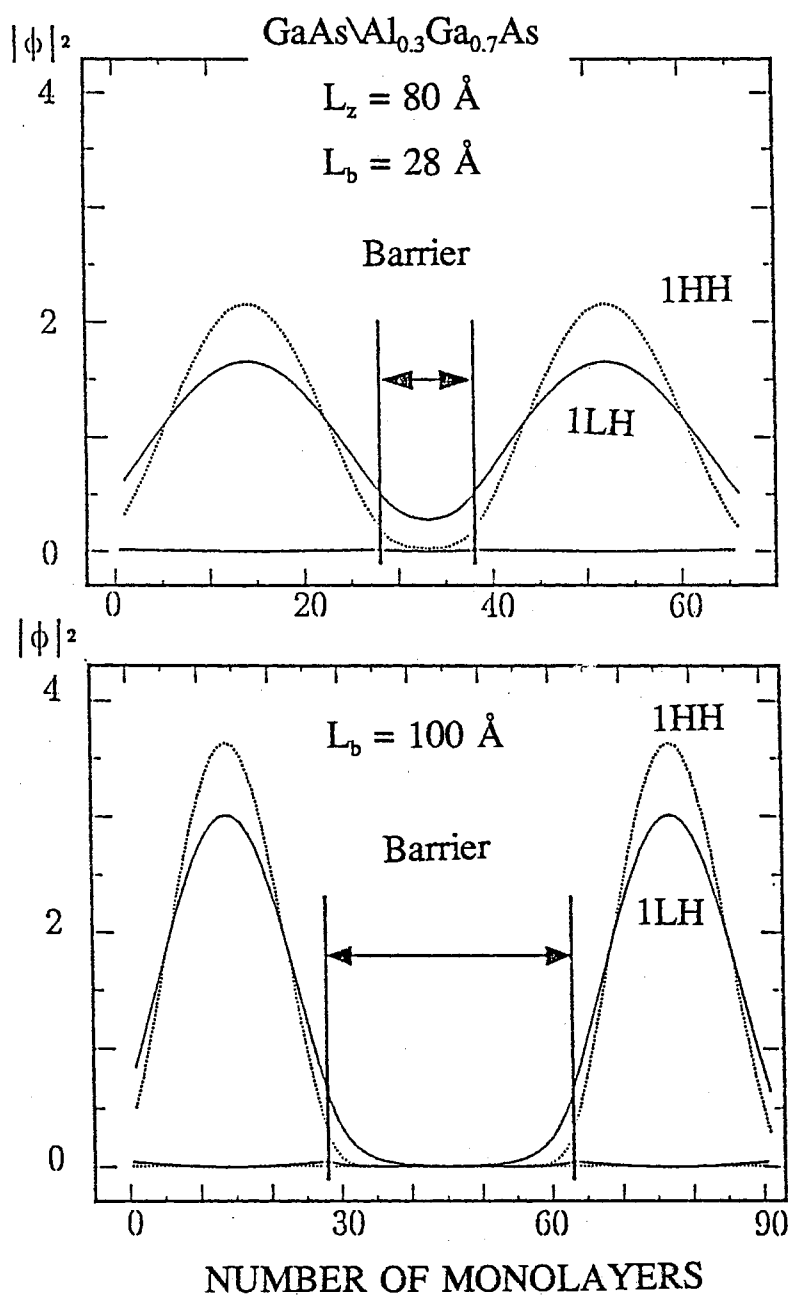


Figure 7. Calculated wavefunction amplitudes for  $n=1$  heavy- and light-holes in GaAs/Al<sub>0.3</sub>Ga<sub>0.7</sub>As superlattices. The  $L_z$ 's are fixed at 80 Å while the  $L_b$ 's are either 28 Å or 100 Å. As  $L_b$  decreases the larger spatial overlap between wavefunctions gives rise to stronger coupling.

Using a Kronig-Penney model in the envelope function approximation or a tight binding model [2,10,11], the subband dispersion along the z-direction may be expressed as;

$$E_n(k_z) = E_n^{QW} - \frac{W_n}{2} \cos(k_z d) \quad (4)$$

$E_n^{QW}$  is the quantized energy for the uncoupled QW, and  $W_n$  denotes the subband width. The period of the superlattice is given by  $L_z + L_b = d$ . In figure 8, the electron subband for a SL is shown in comparison to that of bulk and QW structures. The effect of well-to-well coupling on the band structures, results in the formation of minibands (subbands) from the dispersion along the  $k_z$  direction. The calculated widths of the subband dispersion for the combined  $n=1$  heavy-hole and conduction bands in GaAs/Al<sub>0.3</sub>Ga<sub>0.7</sub>As SL's are shown in figure 9. It can be seen that the width of this dispersion depends exponentially on the barrier thickness. For example, in thick barrier SL's,  $W_n$  is 0 meV, whereas it can be larger than 200 meV in thin barrier SL's.

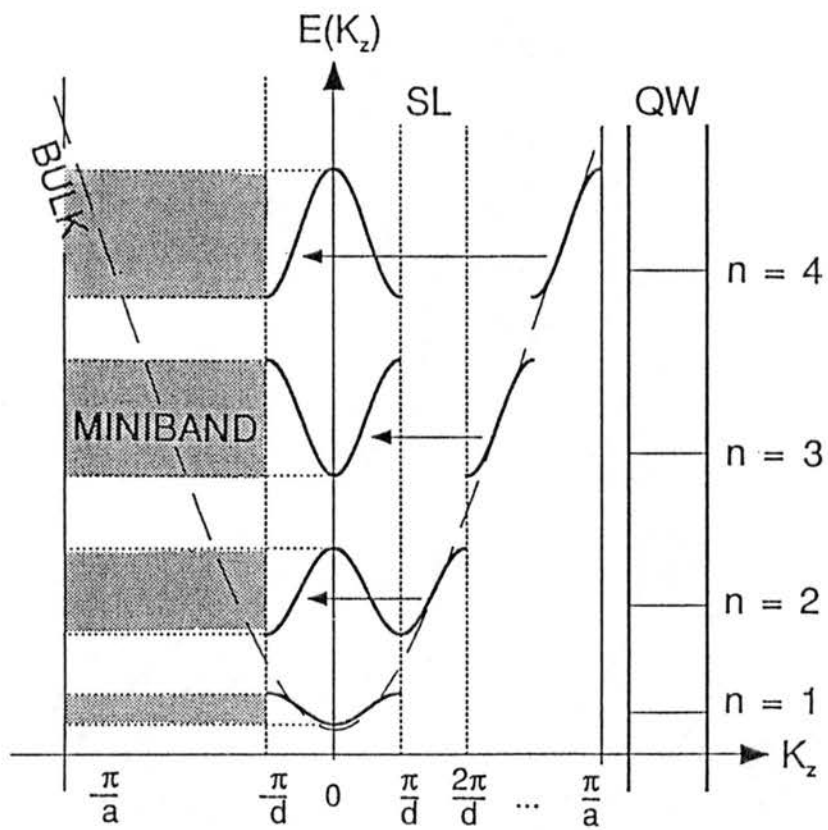


Figure 8. Conduction subband structure of an electron in a superlattice with period  $d$ .

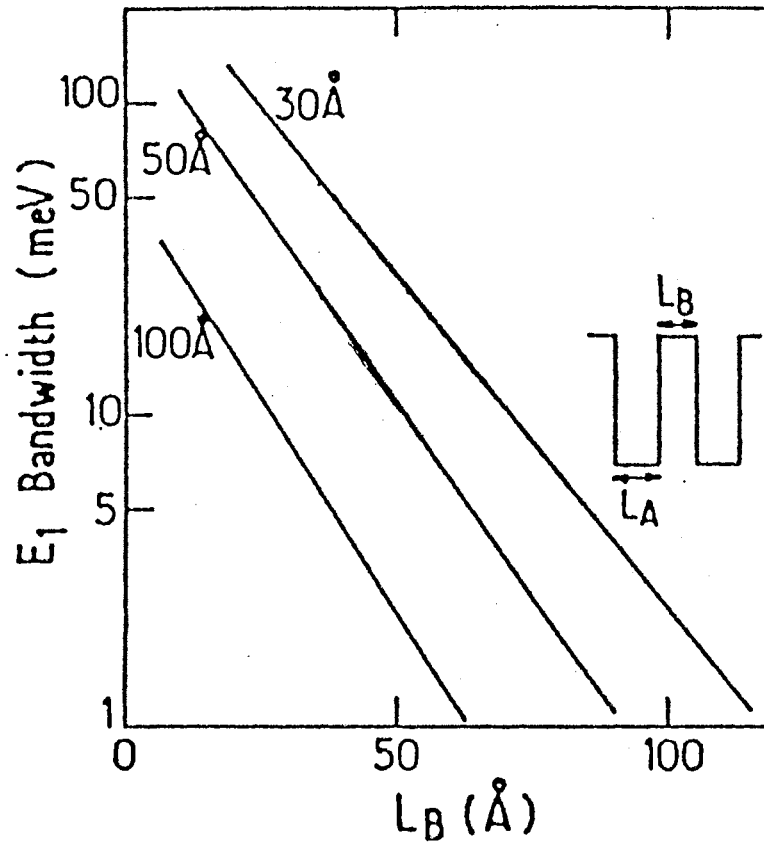


Figure 9. The combined bandwidth for the  $n=1$  conduction and heavy-hole subbands in GaAs/Al<sub>0.3</sub>Ga<sub>0.7</sub>As superlattices versus  $L_B$  for several fixed well widths. Figure copied from reference 11.

## Excitons in Superlattices

Photoluminescence (PL) and Photoluminescence excitation (PLE)

spectroscopies have been used extensively to investigate optical properties associated with band structures in superlattices. The most pronounced features in these optical spectra are those due to fundamental exciton states. An over simplified definition of an exciton is an electron-hole pair which revolve about their center of mass, and are bound by a Coulomb force. Excitons are considered to be discrete state quasi-particles below the band edges and are often the dominant features in optical spectra originating from critical points. In QW structures, the energies of individual exciton states are given by;

$$E_n^{ex} = E_n^{QW} - E_b \quad (5)$$

$E_n^{ex}$  is the optical transition energy of an exciton associated with the  $n^{\text{th}}$  subband .  
 $E_n^{QW}$  is the transition energy between the  $n^{\text{th}}$  conduction and valence subbands in an isolated QW.  $E_b$  denotes the exciton binding energy associated with the  $n^{\text{th}}$  subbands. An effect of subband dispersion in a SL is to shift the energies of excitonic spectra relative to that in an isolated QW. This shift results from a redistribution in the joint density of states arising from well-to-well coupling, as may be seen in the transition energies of excitonic states at  $k_z = 0$  in SL's given by;

$$E_n^{ex} = E_n^{QW} - \frac{W_n}{2} - E_b \quad (6)$$

where  $W_n$  represents the combined electron and hole subband width. Unlike QW's,

the excitonic peak positions given by equation (6) depend on  $L_b$  as well as  $L_z$  and the barrier height.

The binding energy has always been an important issue in the optical spectroscopies of semiconductor materials. In a superlattice, the spatial confinement of excitonic wavefunctions may strongly influence the exciton binding energies away from the corresponding bulk values. In an ideal QW structure, the exciton wave functions are perfectly confined within the well, i.e. an infinite square well. The perfectly confined 2D exciton then has a binding energy four times larger than that of the corresponding bulk material [12]. This implies that the binding energy of a 2D exciton in an ideal GaAs QW is approximately 16 meV. However, QW's used in practice have non-infinitesimal well widths and finite barrier heights so that the quantum confined excitons are of quasi-2D nature. The finite barrier height implies that exciton wavefunctions are not perfectly confined, which leads to penetration of the wavefunctions into the barrier regions. Thus the wavefunction extends along the z-direction covering the QW width ( $L_z$ ) plus the exciton penetration depth. The effect of this wavefunction distribution on exciton binding energies in GaAs can be seen in figure 10 [13]. When  $L_z$  is much larger than the exciton diameter in GaAs ( $\sim 300 \text{ \AA}$ ) [14], the exciton in the GaAs QW is essentially bulk-like and has a binding energy  $\approx 4 \text{ meV}$ . With a reduction in  $L_z$ , the exciton binding energy will increase to a maximum value somewhere between  $E_b(2D) \approx 16 \text{ meV}$  and  $E_b(3D) \approx 4 \text{ meV}$ . The maximum binding energy corresponds to the situation of strongest quantum confinement. Upon a reduction in  $L_z$  the penetration of the exciton

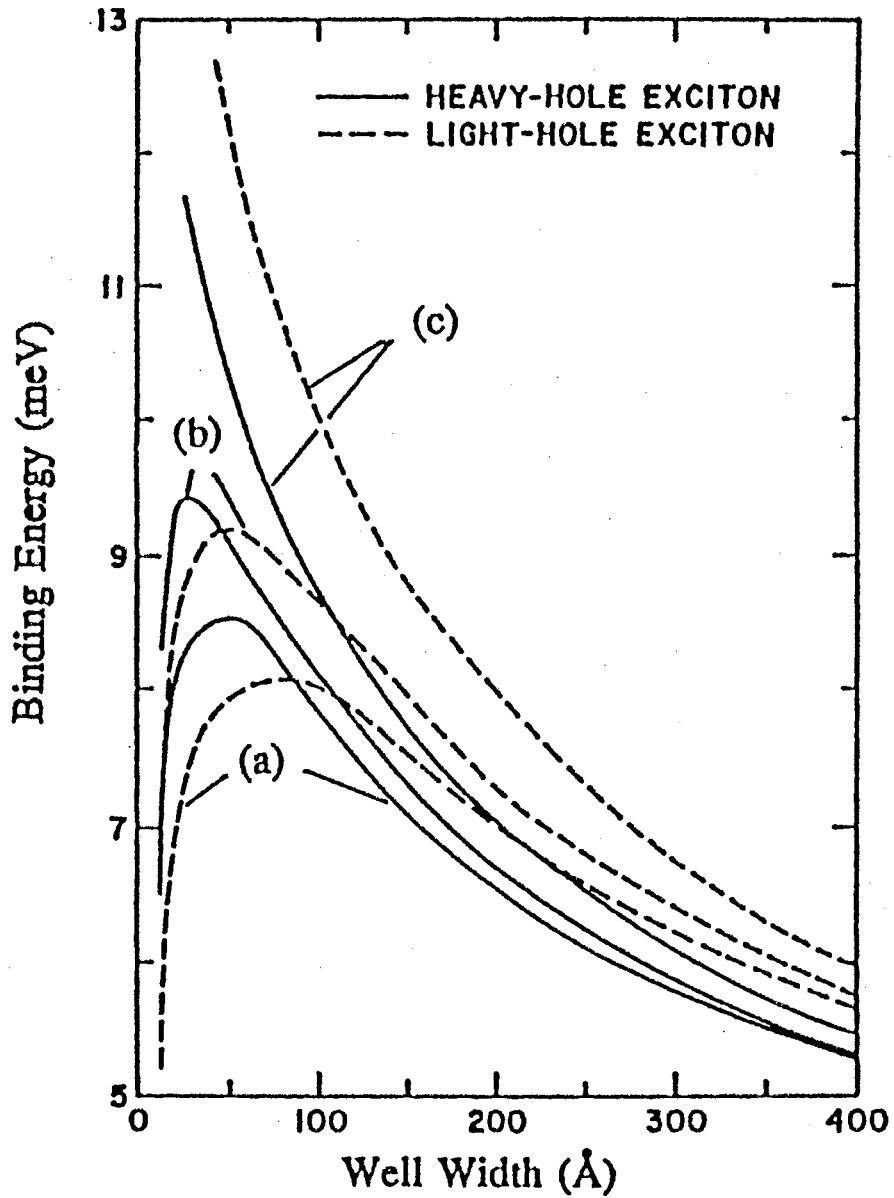


Figure 10. Calculated well-width dependence of the ground state binding energies for the  $n=1$  heavy- and light-hole excitons in GaAs/ $\text{Al}_x\text{Ga}_{1-x}\text{As}$  QW's. The barrier heights correspond to Al concentrations of (a)  $x=0.15$ , (b)  $x=0.3$ , and (c) for an infinite well [13].



wavefunctions into the barrier regions is enhanced since it lifts the confined energy levels toward the barrier height. This effect tends to reduce the strength of the confinement resulting in lower binding energies. Therefore in the limit of  $L_z \rightarrow 0$ , the exciton binding energy approaches the 3D bulk value of the barrier material [13]. Since the barrier heights strongly influence the wavefunction penetration depth, the binding energy will also depend on  $x$ . For a constant  $L_z$  the exciton binding energies decrease with smaller barrier heights. This arises from larger wavefunction penetration with decreasing barrier heights. In the case of a SL, the exciton wavefunctions in adjacent wells spatially overlap leading to the expectation that binding energies should be less than that in isolated QW's with the same  $L_z$  and  $x$ .

There have been many experimental results published concerning exciton binding energies in QW's [15-21]. In several cases, the binding energies are estimated using PLE [15-17] or magneto-optical spectroscopy [18-21]. In magneto-optical spectroscopy, the Landau levels associated with excitonic and band-to-band transitions have different characteristics, thus providing an estimate to the exciton binding energies in QW's. PLE spectroscopy is capable of resolving the energy difference between 1s and 2s excited exciton states. This also provides a good estimate of exciton binding energies in QW's, since it is believed that the 2s excited exciton state is very near the continuum of exciton states just below the band edge [15-17]. The exciton binding energies in SL's may be more difficult to experimentally estimate using the aforementioned techniques. This is because subband dispersion plays an important role in optical spectra of superlattices.

## Optical Excitation Spectra in GaAs/Al<sub>x</sub>Ga<sub>1-x</sub>As Superlattices

The theoretical and experimental studies of Chu and Chang [22], and Song et al. [23] have clearly identified the effects of subband dispersion on the  $n=1$  excitonic spectra in GaAs/Al<sub>x</sub>Ga<sub>1-x</sub>As SL's. Experimental PLE and theoretical photoabsorption lineshapes of specific superlattices are shown in figure 11. The peaks labelled 1HH and 1LH originate from fundamental excitonic transitions occurring at the  $M_0$  critical point in QW and SL structures. According to the theoretical lineshape, the peaks H and L are attributed to a mixture of  $2s$  exciton states and the band edge resonance arising from a redistribution of the oscillator strengths caused by the Coulomb interaction [22,23]. In a QW or SL with thick  $L_b$ , the peaks H and L are most likely  $2s$  excited exciton states merged into a step-like band continuum. However, in a SL with thinner  $L_b$ 's a significant portion of H and L arise from the lower subband edge resonances [22,23]. In contrast to the nearly symmetric lineshape of the fundamental exciton peaks, the peaks H and L have an asymmetric lineshape. The sharp rise of these peaks may be attributed to the  $2s$  excited states while the slowly decreasing tail is caused by subband edge resonances [23]. The origins of these spectra are described well by the theory of Chu and Chang. According to this model the energy separations between peaks 1HH (1LH) and H (L) may be used to derive a reasonable estimate to exciton binding energies in SL's. In addition, these energy separations decrease with thinner  $L_b$ , which implies that the exciton binding energy is also decreasing. These are important features which are used to explain the results in chapter III.

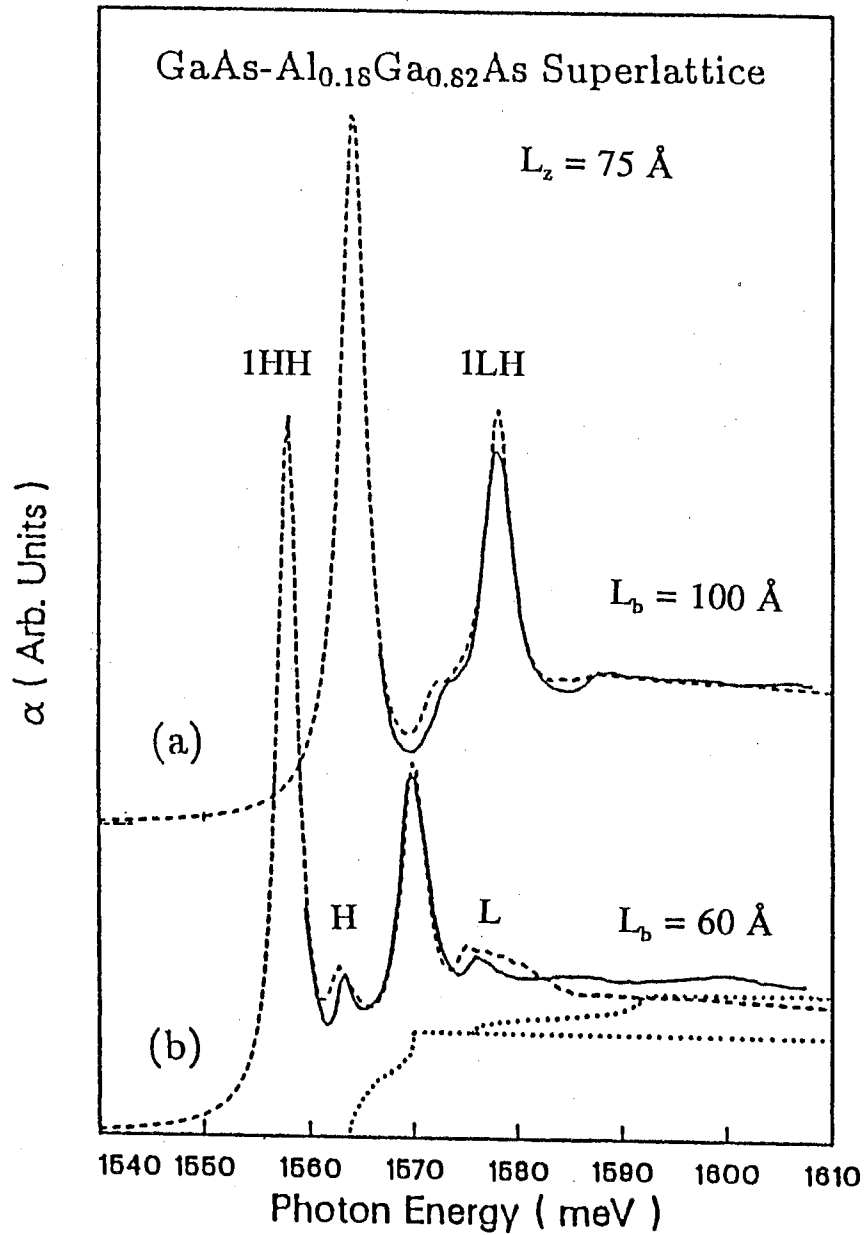


Figure 11. Theoretical absorption spectra (dashed curves) and experimental PLE data (solid curves) for GaAs/Al<sub>0.18</sub>Ga<sub>0.82</sub>As SL's with  $L_z=75 \text{ \AA}$  and  $L_b$ 's equal to  $100 \text{ \AA}$  and  $60 \text{ \AA}$ . The continuum states associated with 1hh and 1Lh subbands for  $L_b=60 \text{ \AA}$  are shown by the dotted lines [23].

## CHAPTER II

# EXCITON LINE NARROWING IN THIN BARRIER SUPERLATTICES

### Introduction

The optical linewidths associated with excitonic transitions in semiconductor quantum well structures are important in the development of certain devices such as optical switches and modulators. In these devices, an applied static electric field causes a shift in the excitonic transition energies. If the linewidth of an excitonic transition under consideration is on the order of the energy shifts produced by the applied field, the performance of the device could easily be restricted [24]. Therefore, it is of technological interest to know and understand the mechanisms which cause the broadening of excitonic transitions. These mechanisms can be categorized as homogeneous or inhomogeneous broadening effects. Homogeneous broadening can be due to several interactions such as exciton-exciton, exciton-carrier, or thermal broadening due to exciton-LO phonon interactions [25,26]. At low temperatures and low photoexcited carrier concentrations, the principal line broadening mechanism arises from inhomogeneous origins [24,27-30]. These broadening effects are caused primarily by structural or compositional fluctuations which occur during the growth of

heterostructures. Inhomogeneous broadening of excitonic transitions in single quantum well (SQW) and multiple quantum well (MQW) structures have received much attention [24,27-37], but little has been given to superlattice (SL) structures [38-40]. The SL can differ significantly from the QW structures by unique features initiated from the coupling of excitonic or electronic states. As discussed in chapter I, this coupling leads to significant subband dispersion along the  $k_z$  direction forming minibands. In this chapter a systematic investigation on the effect that subband dispersion in a SL has on the inhomogeneous broadening of the fundamental  $n=1$  heavy-hole (1HH) and light-hole (1LH) excitonic transitions will be presented.

In the customary GaAs/ $\text{Al}_x\text{Ga}_{1-x}\text{As}$  MQW structures, the inhomogeneous broadening mechanism of most concern is due to structural disorder [24,27-30]. This disorder can be characterized by intralayer or interlayer fluctuations in the widths of the GaAs quantum wells [31,32]. Intralayer fluctuations occur along the x-y plane forming interface roughness, which can lead to significant growth islands of GaAs on an  $\text{Al}_x\text{Ga}_{1-x}\text{As}$  surface layer, for example. Interlayer fluctuations describe differences of an entire interface layer between the well and barrier widths along the growth direction (z-axis). Both types of fluctuations are described in figure 12, and are certain to exist to some extent in any superlattice structure grown by epitaxial methods such as MBE. The height of these fluctuations (i.e. size of fluctuation along z-direction) is usually quoted as one monolayer [28,29,31,32,34,35]. However some work suggests that excitonic linewidths are governed by an effective one-half monolayer height [33]. It has been shown that interface quality of MBE grown

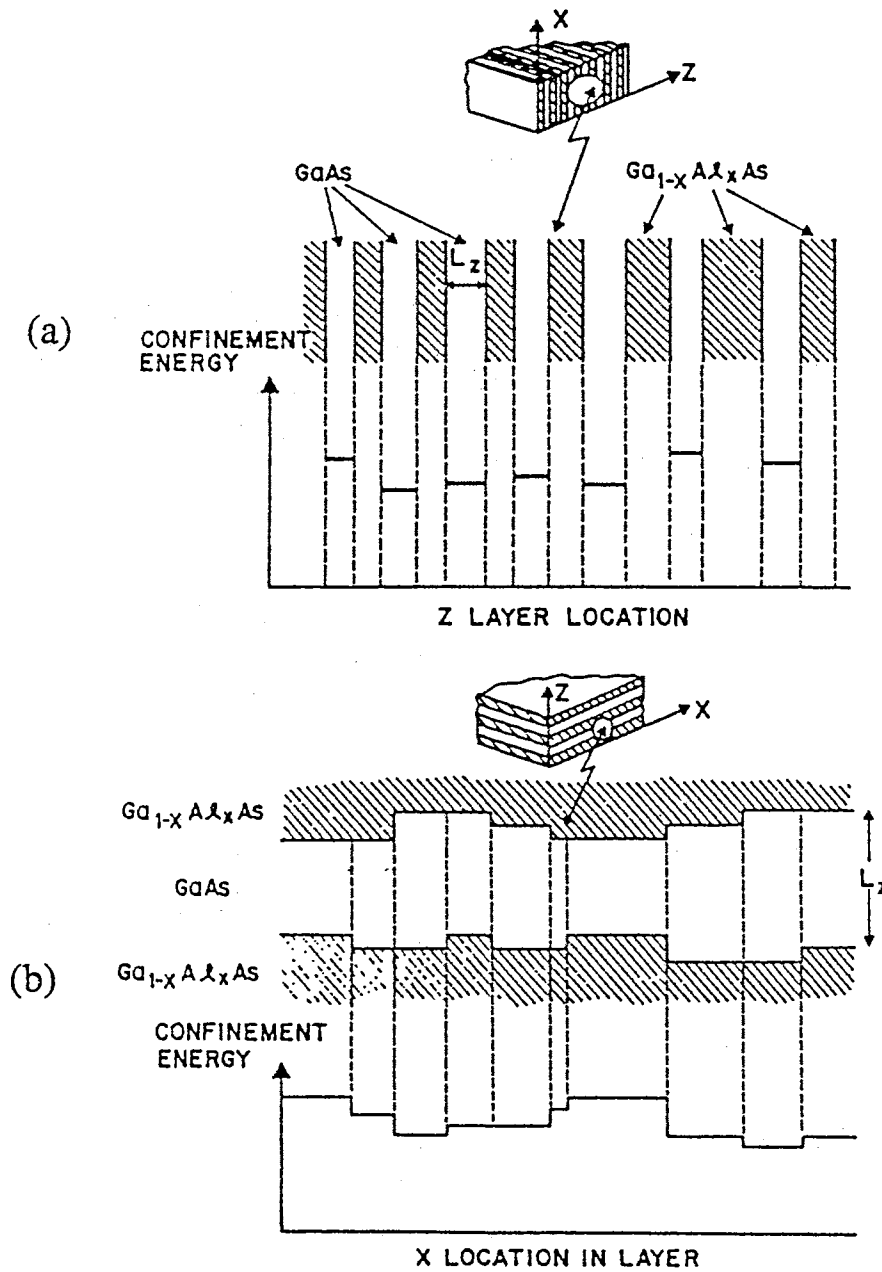


Figure 12. Schematic representation of (a) interlayer fluctuations and (b) intralayer fluctuations caused by structural disorder. The horizontal lines represent the energy levels in a specific quantum well. The disorder produces a distribution of these levels.

GaAs/ $\text{Al}_x\text{Ga}_{1-x}\text{As}$  quantum well structures depends strongly on the substrate (growth) temperature, and that island heights can reach five monolayers if improper temperatures are used [41,42]. Another significant source of interface roughness is due to the mechanical performance of a shutter used in MBE growth [43]. In practice the shutters are incapable of opening and closing with precise abruptness. The time involved in this process can initiate both intra- and interlayer fluctuations. This can lead to a layer of  $\text{Al}_x\text{Ga}_{1-x}\text{As}$  not being completely full before the GaAs layer is grown forming islands [43].

There are several experimental techniques which are capable of studying the quality of the interfaces. Those such as X-ray or transmission electron microscopy (TEM) measurements can determine approximately the interface quality [31,41], but optical techniques such as photoluminescence (PL), photoluminescence excitation (PLE) or absorption spectroscopy can provide useful quantitative results [24,27-35]. Although, the state-of-the-art experimental method for studying this type of problem is a digital chemical lattice imaging technique [43,44].

Optical techniques use the exciton as a probe of the interface roughness. Since in a MQW the Bohr radius of an exciton in the x-y plane is approximately  $150 \text{ \AA}$ , the exciton is able to characterize the lateral region of an interface covered by its spatial extent. It is well known that two or three sharp peaks can appear in the excitonic spectra of MQW's observed by PL, PLE or absorption measurements. These peaks typically differ by only a few meV, and are routinely associated with abrupt monolayer changes arising from intra- or interlayer fluctuations [34]. This idea was

first presented experimentally by Weisbuch and Dingle [31]. They interpreted their data as intralayer fluctuations creating growth islands with a height of one monolayer and a lateral extent  $\approx 300 \text{ \AA}$ . The effect of these growth islands on the PL or PLE spectra were found to be significantly reduced by introducing interrupted MBE growth methods, which led to a sharp narrowing of the excitonic lineshapes observed by optical techniques [35-37]. The cause of this line narrowing is due to the relative size in the lateral extent ( $\mathcal{L}$ ) of the intralayer growth islands to the diameter ( $D_{\text{ex}}$ ) of the exciton. Several basic models of interface roughness which qualitatively describe optical linewidths can be realized from a comparison between  $D_{\text{ex}}$  and  $\mathcal{L}$ . These are summarized in figure 13 [35]. If  $\mathcal{L} \sim D_{\text{ex}}$  the exciton will probe two or more well widths differing by a monolayer as shown in 13(a). The experimental exciton lineshape will be broadened due to the distribution of quantized energy levels within the space covered by  $\mathcal{L}$ . If  $\mathcal{L} \gg D_{\text{ex}}$  there will be at most two definite ground states probed by  $D_{\text{ex}}$  as shown in figure 13(b), resulting in sharp peaks. In a typical luminescence experiment, the laser spot size could be 0.3 mm, which is 10,000 times larger than an exciton diameter. Therefore, several sharp peaks are possible in the luminescence spectra. In cases where figures 13(a) and 13(b) apply, the peaks shapes may change with the location on the sample, however the peak positions are expected to remain fixed. If  $\mathcal{L} \ll D_{\text{ex}}$  the lineshape is expected to be narrow as a result of excitonic averaging of many islands. In this case, the interface possesses microroughness, as shown in figures 13(c) and 13(d) and multiple peaks appear in luminescence spectra [35]. In contrast to figure 13(b), the energies as well as peak



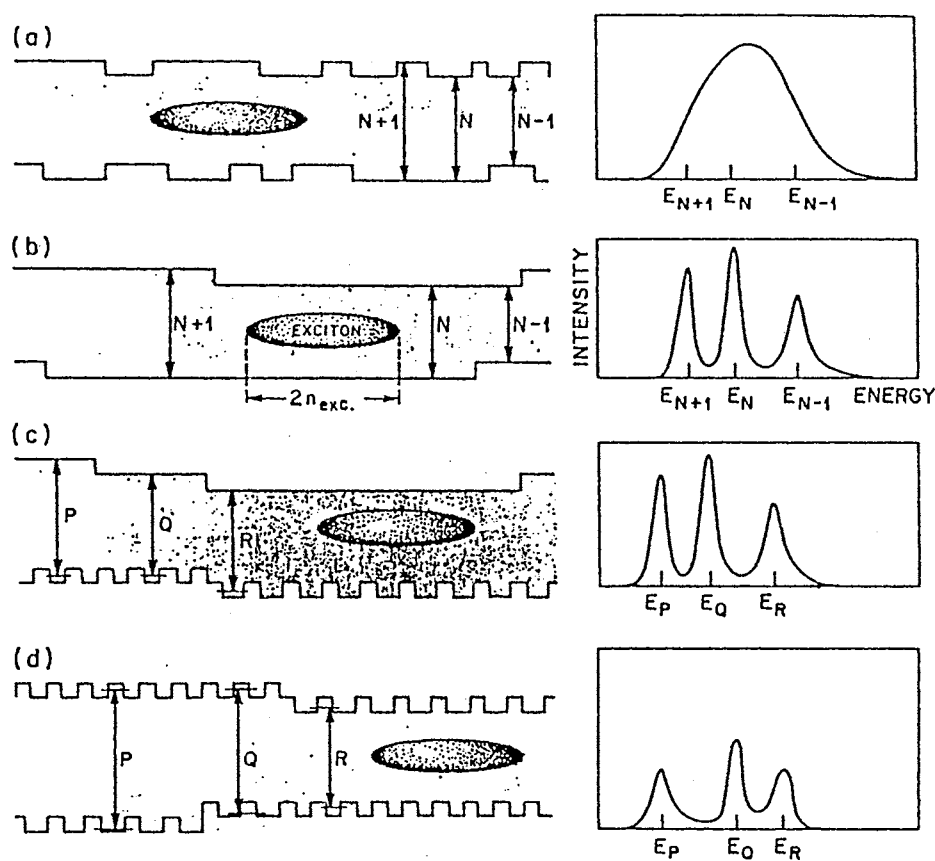


Figure 13. Schematic illustration of various interface roughness formed by intralayer fluctuations. The energy position of the luminescence spectra taken from various spots on the sample is expected to be fixed in formations (a) and (b), while it varies for those in (c) and (d) [35].

shapes are expected to be vary with location in the sample. The conditions described by figures 13(b) and (c) can be obtained using interrupted MBE growth techniques, which leads to extremely narrow linewidths [35-37]. Therefore if growth islands are much larger or smaller than  $D_{ex}$ , optical techniques suggest relatively smooth interfaces. However this only applies to intralayer fluctuations, and interlayer fluctuations in a MQW structure can still result in significant excitonic line broadening. It is difficult to experimentally distinguish between interlayer or intralayer fluctuations in individual MQW structures. Independent results of intralayer fluctuations can be obtained however in SQW strutures [27,35-37,43].

Because of the nature of the interface roughness a significant dependence of excitonic broadening on the well-widths ( $L_z$ 's) and barrier-widths ( $L_b$ 's) may be expected. The transition energy of an exciton in a GaAs/ $Al_xGa_{1-x}As$  quantum well measured in a luminescence experiment can simply be expressed as;

$$E_{ex} = E_c + E_h - E_b + E_{GaAs} \quad (7)$$

where  $E_{c,h}$  are the corresponding quantized energy levels for electrons and holes,  $E_b$  is the exciton binding energy, and  $E_{GaAs}$  is the band gap of bulk GaAs. The binding energy of excitons is not expected to vary significantly with small fluctuations in  $L_z$  or  $L_b$  [28,39,45]. Because of the ( $L_z^{-2}$ ) dependence of the quantized energy levels considerable variations in  $E_c$  and  $E_h$  can be expected with monolayer fluctuations, especially for smaller values of  $L_z$ . A notable reduction in the linewidths of the  $n=1$  heavy-hole (1HH) and light-hole (1LH) excitons was observed in the PLE spectra of GaAs/ $Al_xGa_{1-x}As$  MQW's with an increase in  $L_z$  [24]. This is easy to understand

realizing that the source of the line broadening is from monolayer fluctuations. This will give rise to a distribution of excitonic transition energies for any quantum well structure [24,27-29,31-33,38-40]. This distribution has been treated theoretically either by Gaussian or Lorentzian functions [38-40]. A simple expression for the variance of the distribution may be written as [40];

$$\sigma \approx \left[ \frac{\partial E_n}{\partial L_z} \right] \delta_z + \left[ \frac{\partial E_n}{\partial L_b} \right] \delta_b \quad (8)$$

where  $E_n$  is the quantized energy in the well and  $\delta_i$  is the height of the fluctuation in the well- ( $i=z$ ) or barrier- ( $i=b$ ) widths along the  $z$ -axis. The linewidth can then be determined from the variance of the distribution [40]. In the case of MQW's, the  $L_b$ 's are thick and the second term of equation (8) can be neglected. Since for smaller values of  $L_z$  the slope of the quantized energy versus the well thickness is larger, it is expected that the line-widths due to monolayer fluctuations will be broadened upon a reduction in  $L_z$ . This is true provided that the  $L_z$ 's are not too thin. It has been shown that in QW's with very thin GaAs layers, the linewidths become extremely narrow. This was explained as the effect of the ground state energy of the quantum well approaching the upper bound limit set by the finite potential barrier [36].

## Experimental Setup and Procedures

The experimental setup for the luminescence experiments is shown in figure 14. It consists of a Spectra Physics model 171 argon ion laser which can produce up to 15 Watts of continuous wave (cw) power. This laser is used to pump two Spectra Physics model 375B dye lasers. Each dye laser is equipped with slightly different optics so that a broad wavelength range can be obtained. A summary of the performance of the laser dyes used are given in table IV. The output from a dye laser is guided and focused onto the sample located in a closed cycle He gas refrigerator capable of lowering the lattice temperature to approximately 10 K. The luminescence is collected and focused into a SPEX 1877 triplemate spectrometer with silver coated mirrors for high throughput in the near infrared. Either one or two lens combinations may be used as the collection optics, as long as the f number matches close to that of the triplemate ( $1/f \sim 4$ ). The luminescence intensity is recorded by computer using either a Photometrics model PM512 liquid nitrogen cooled charge coupled device (CCD) or a Hamamatsu GaAs photomultiplier tube (PMT) and photon counting electronics. The dye lasers and spectrometer can be individually scanned by a personal computer. A simple He-Ne laser (not shown) is also used for alignment as well as an excitation source in photoluminescence measurements.

Photoluminescence is simply a measure of the radiative decay of electron-hole pairs (excitons). Electrons (holes) which are photoexcited into the conduction (valence) band relax non-radiatively to the band minima. Provided there are no traps induced by defect or impurity states, the electrons and holes then recombine

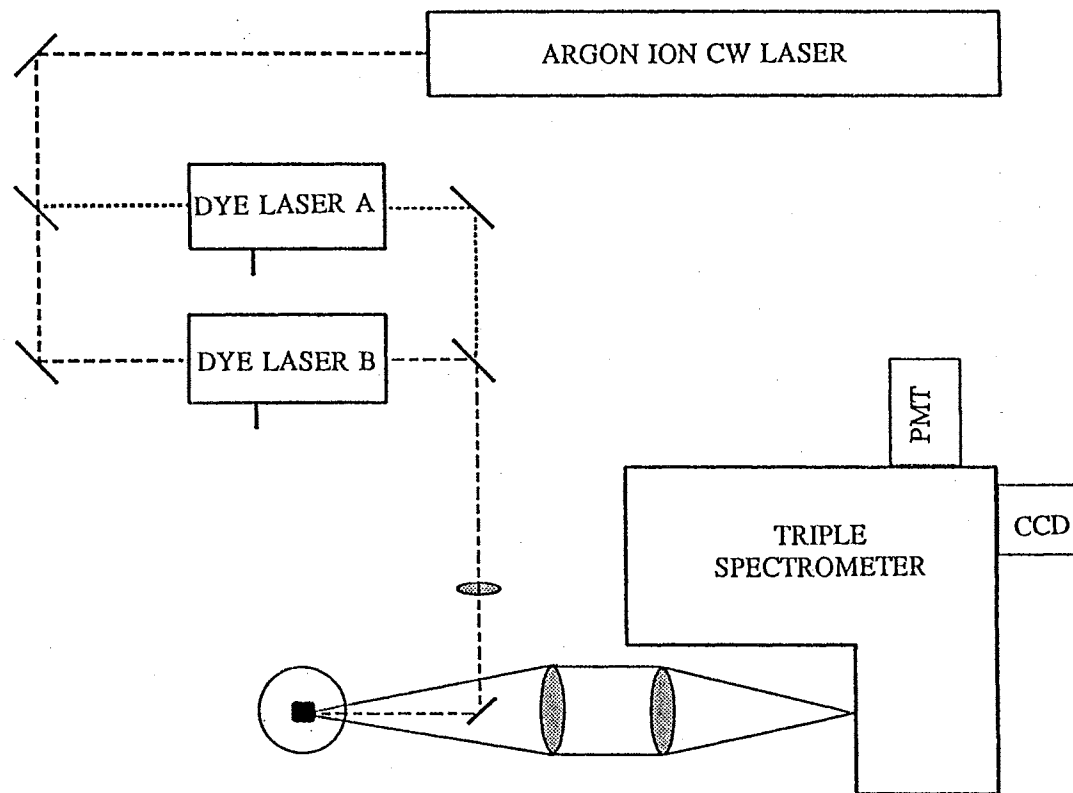


Figure 14. Schematic diagram of PL and PLE experimental setup.

TABLE IV  
DYE LASER TUNING RANGES AND OUTPUT POWERS

DYE NAME	RANGE (nm)	RANGE (eV)	PEAK OUTPUT	†PUMP POWER
DCM	610-690	1.80-2.03	300 mW	3.5 W
PYRIDINE 1	695-770	1.61-1.78	150 mW	2.5 W
STYRYL 8 (LDS751)	730-810	1.53-1.70	300 mW	3.5 W
STYRYL 11 (LDS798)	770-825	1.50-1.61	150 mW	4 W

† These values are for a 5145 Å pump wavelength.

at the band minima emitting luminescence. In superlattices, the PL signal is usually attributed to the decay of the 1HH exciton. In contrast to photoluminescence experiments (PL), photoluminescence excitation (PLE) involves a continuous change in the excitation energy while monitoring the PL intensity. When the excitation energy matches an excited state which has efficient absorption or relaxation to the ground state, the PL intensity is strongly enhanced. The PLE spectra is a trace of the PL intensity as a function of excitation energy. In this way, various optical transitions in the quantum well structure may be identified (see for example chapter I).

In this experiment a series of high quality MBE samples were grown with constant  $L_z$  and  $x$ , while the  $L_b$ 's vary. The sample parameters were carefully chosen so as to produce a significant change in subband dispersion ( $W_n$ ) within the

TABLE V  
SUBBAND ENERGY PROPERTIES

SAMPLE	A	B	C	D	E
$L_b$ (Å)	130	99	71	51	31
$W_{1e}$ (meV)	1.4	4.8	7.6	19.9	40.8
$W_{1lh}$ (meV)	1.3	4.1	6.4	15.8	30.8
$W_{1hh}$ (meV)	<0.1	0.1	0.1	0.9	3.5
$\Delta_{1e}$ (meV)	2.4	2.4	2.4	2.5	2.9
$\Delta_{1lh}$ (meV)	1.3	1.3	1.3	1.4	1.6
$\Delta_{1hh}$ (meV)	0.9	0.9	0.9	0.9	1

series. The  $L_b$ 's are given in table V for the series examined in this work. In each sample  $L_z = 59$  Å and  $x = 0.14$ . The layer widths were accurately determined by transmission electron microscopy (TEM) measurements, and the aluminum concentration was determined from PL measurements of a bulk  $\text{Al}_{0.14}\text{Ga}_{0.86}\text{As}$  sample grown in series with the superlattices. The amount of subband dispersion (miniband width) is given by  $W_n$ , where  $n=1e, 1lh$ , or  $1hh$  denotes the first confined electron, heavy- and light-hole subbands respectively. This quantity is determined from a tight-binding calculation using a 65/35 valence band offset [47].

The PL and PLE spectra taken from these samples are shown in figure 15 and figure 16 respectively. It is evident that a sharp narrowing of the exciton spectra

occurs with a reduction in the  $L_b$ 's, especially in the PLE spectra. This trend is qualitatively in disagreement with that predicted by equation (8). Since the second term in equation (8) becomes important in superlattices, the variance becomes larger with a reduction in  $L_b$  from the MQW limit to the SL limit. (i.e. the onset of significant coupling between quantum wells). If the energy of an electron or hole is given by  $E_{QW}(L_z, L_b)$ , a fluctuation of one monolayer in the well and barrier widths will result in an energy given by  $E_{QW}(L_z \pm \delta, L_b \mp \delta)$ , where the period of the superlattice is assumed constant. In table V, the shifts in energy defined as  $\Delta_n = E_{QW}(L_z, L_b) - E_{QW}(L_z + \delta, L_b - \delta)$  are given for the  $n=1$  electron, light-, and heavy-hole states at the minizone center ( $k_z = 0$ ). For a well width of 59 Å and an aluminum concentration of 14%,  $\Delta_n$  is nearly constant for all values of  $L_b$  used in this study. Therefore, equation (8) would predict only a slight increase in the linewidths upon a reduction in  $L_b$  from 130 Å to 31 Å. In reference 40, a reduction in the linewidths seen in PL spectra of GaAs/Al<sub>x</sub>Ga<sub>1-x</sub>As quantum well structures was observed upon a decrease in  $L_b$ . It was suggested that the line narrowing was a result of coupled excitons extending over many superlattice periods and thus averaging the effects of monolayer fluctuations [40]. This is a simple idea which applies qualitatively to our experimental results. This present study however, independently measures the line widths of both heavy- and light-hole excitons which PL studies are incapable of doing. In addition the samples selected form a consistent series unlike those in reference 40, which used various  $L_z$ ,  $L_b$ , and  $x$ .



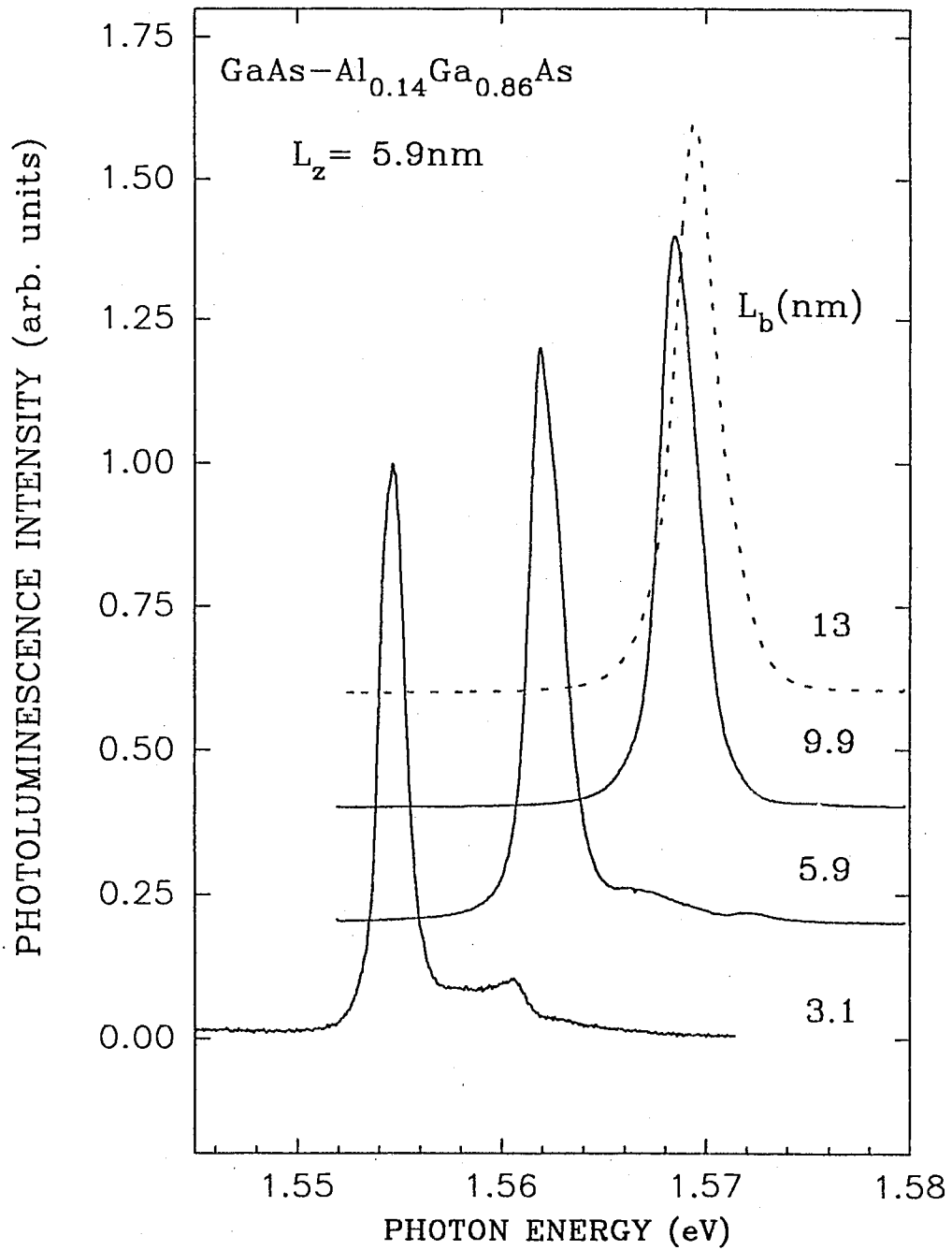


Figure 15. Photoluminescence spectra from a series of MBE grown GaAs/ $\text{Al}_x\text{Ga}_{1-x}\text{As}$  superlattices demonstrating line narrowing. The well widths ( $L_z$ 's) are all fixed at 59 Å and the aluminum concentration is 14%. The barrier widths are given in the figure.

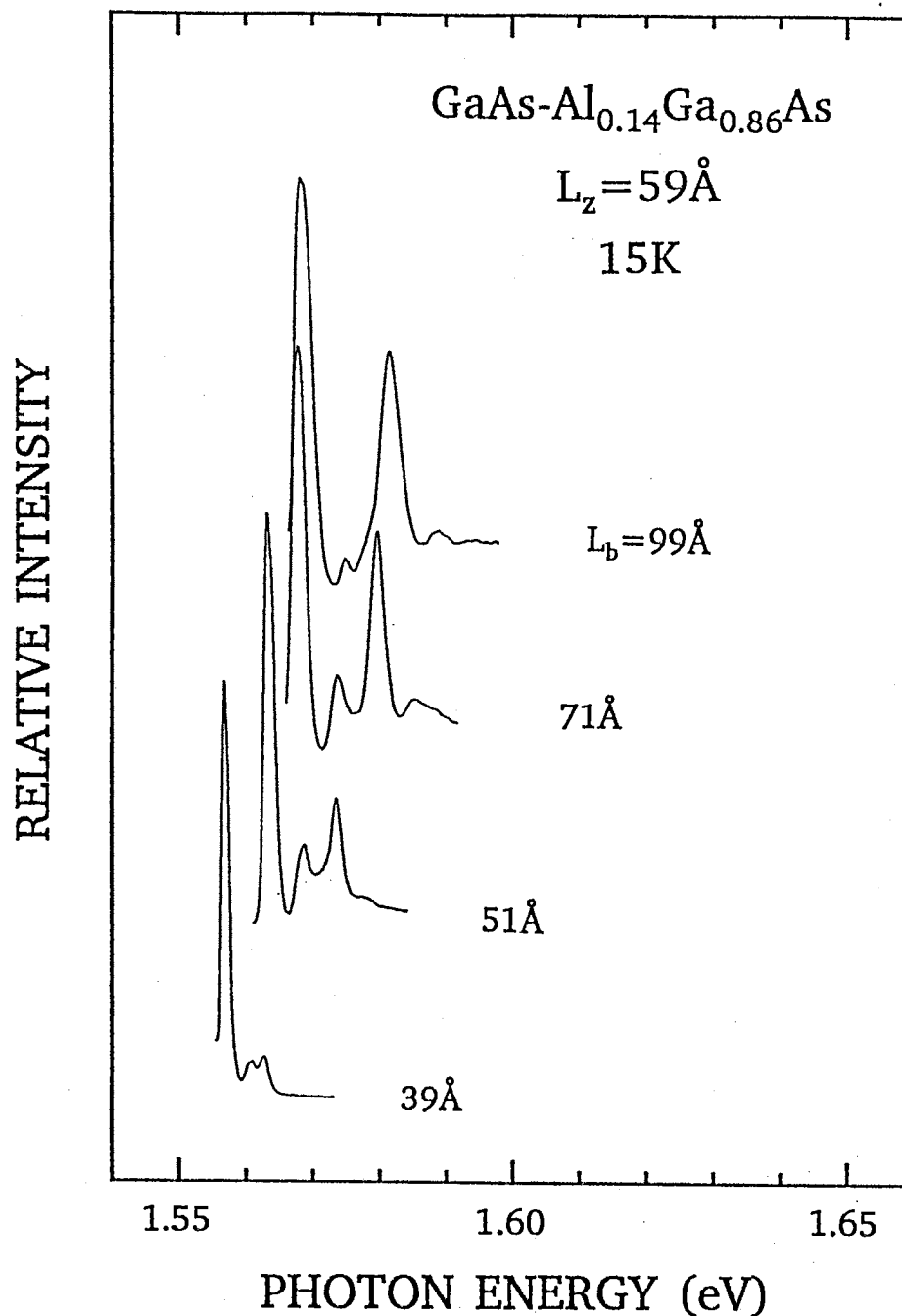


Figure 16. Photoluminescence excitation spectra from the series of samples described in table V. The  $n=1$  heavy- and light-hole excitons are denoted by 1HH and 1LH, respectively. The spectrum for the  $L_b = 130 \text{ \AA}$  sample is similar to that with  $L_b = 99 \text{ \AA}$ , and is not shown. It is evident that a sharp narrowing of the PLE spectra occurs with a reduction in  $L_b$ . The fine structure in the spectra are explained in chapter I.

## Exciton Linewidth Theory

The line narrowing can be correctly modeled from a multiple scattering theory using only electron and hole subband states. It will be shown that in the weak scattering limit, broadening of the excitonic transitions due to monolayer fluctuations is proportional to the subband density of states. Since the subband dispersion along  $k_z$  increases with a reduction in  $L_b$ , the corresponding density of states is smaller. This leads qualitatively to a narrowing of the  $n=1$  excitonic transitions with a reduction in the barrier-widths.

The theoretical treatment of this problem is similar to that for an infinite 1-dimensional crystal with random defects. If the random defects are assumed to be homogeneously distributed on a macroscopic scale, a multiple scattering theory based on a Green's function technique may be used to treat the disorder [48]. Detailed discussions on disordered crystals and the corresponding properties of phonons, electrons and excitons determined by multiple scattering theories may be found in references 48-54. In the theoretical treatment of exciton line narrowing in superlattices, only the effects of disorder on electron and hole subband states caused by interlayer fluctuations are considered. The superlattice is viewed as an infinite 1-dimensional chain of coupled quantum wells. The distribution of energies originating from interlayer fluctuations are treated as an on-site disorder. Thus, at each quantum well site a Lorentzian distribution of energies for each of the  $n=1$  subbands is placed. This distribution is centered at  $E_{QW}(L_z, L_b)$  and has a half-width,  $\Delta_n$  given in table V.

The effects of this random disorder on the individual electron and hole states generally will shift and broaden the optical transitions involving these states. In a weak scattering limit, the shifts in energy are expected to be small in comparison to  $E_{QW}(L_z, L_b)$  and only the broadening becomes important [49]. In the following, a multiple scattering theory using Green's functions will be discussed which accurately calculates the broadening of electronic states caused by interlayer fluctuations.

To begin this discussion the Green's function used is formally called a double-time retarded Green's function,  $G_R(t, t')$  defined as [48];

$$G_R(t, t') = \frac{2\pi}{i\hbar} \theta(t-t') \langle [A(t), B(t')]_{\eta} \rangle \quad (9)$$

$$\equiv \langle\langle A(t); B(t') \rangle\rangle$$

$A(t)$  and  $B(t')$  are operators of the system under consideration, and  $\eta$  is equal to +1 (-1) in the commutation of these operators for fermions (bosons). The theta function insures that the cause at time  $t$  is preceded by the effect at time  $t'$ . The brackets  $\langle \rangle$  enclosing the commutator of the two operators symbolizes the statistical average [48]. If the Green's function is defined in terms of Heisenberg operators, the time dependence of  $G_R(t, t')$  will depend only on the difference between the times  $t$  and  $t'$ . It is often convenient to work with the Fourier transform of  $G_R(t-t')$  given by;

$$G_R(\omega) = \frac{1}{2\pi} \int_0^{\infty} G_R(t) \exp[i\omega t] dt \quad (10)$$

where  $t' = 0$  and  $\omega$  is a complex variable such that the retarded Green's function is analytic in the upper half plane of  $\omega$  (i.e.  $\Im\omega > 0$ ). The Green's function defined in

equation (9) must satisfy the Heisenberg equation of motion

$$i\hbar \frac{\partial}{\partial t} G_R(t) = 2\pi \delta(t) \langle [A(t), B(0)]_\eta \rangle + \langle\langle [A(t), H(t)]_\eta; B(0) \rangle\rangle \quad (11)$$

where  $H(t)$  is the Hamiltonian of the system.

A perfect crystal with translational symmetry has a single particle Hamiltonian which can be represented in terms of Wannier functions as [48,49];

$$H_0 = \sum_{\alpha, s} E_\alpha(\vec{r}_s) a_\alpha^\dagger(\vec{r}_s) a_\alpha(\vec{r}_s) + \sum_{\alpha\alpha', ss'} W_{\alpha\alpha'}(\vec{r}_s, \vec{r}_{s'}) a_\alpha^\dagger(\vec{r}_s) a_{\alpha'}(\vec{r}_{s'}) \quad (12)$$

The operators  $a_\alpha$  and  $a_\alpha^\dagger$  are destruction and creation operators respectively,  $\alpha$  and  $s$  are indices for labeling the different bands and sites in the crystal. Since the  $n=1$  subbands are the only ones considered and each conduction and valence band is treated separately the index  $\alpha$  will be dropped. The Green's function of interest to this problem is the single particle Green's function defined by [48];

$$G(\vec{r}_s, \vec{r}_{s'}, t) = \langle\langle a(\vec{r}_s, t); a^\dagger(\vec{r}_{s'}, 0) \rangle\rangle \quad (13)$$

It has the physical meaning of creating a particle at site  $s'$  when  $t'=0$ , and at a later time  $t$ , destroying the particle at site  $s$ . Because of this the single particle Green's function is often referred to as a propagator. Inserting the single particle Green's function into the Heisenberg equation of motion, and performing time and space

Fourier transforms an equation for the Green's function may be expressed as;

$$G_o(E, \vec{k}) = [EI - H_o]^{-1} \quad (14)$$

where by definition of the Green's functions each term represents a matrix. In this equation the identity matrix I is introduced. The poles of the Green's functions are the energies given by the Hamiltonian. In the perfect crystal, these energies lie on the real axis of the complex  $\omega$  plane. This would correspond to excitations with a delta function width [49].

Because of the random structural disorder in the 1-dimensional superlattice, it is expected that a broadening effect will at least be introduced into the energies of the excitations. This simply means that in a weak scattering limit the poles of the Green's functions will be near the real axis in the complex  $\omega$  plane [48]. The multiple scattering theory follows from perturbation theory in which the solutions to the Hamiltonian are expressed in a power series of the interaction [49]. For the problem discussed here only the scattering of a single particle with the potential represented by the on-site disorder is considered. Two body interactions such as carrier-carrier and electron-phonon scattering can be neglected in the treatment provided that the carrier densities and lattice temperatures are low.

For simplicity, the unperturbed Green's functions will be written as  $G_o(1,2)$  where the numerals 1 and 2 each indicate the positions and times described by the propagation of a particle. If the on-site disorder is represented by U, then the new Green's function to be found may be written as  $G(1,2;U)$ . This Green's function will describe a particle propagating in space and time under the influence of the random

potential. In general multiple repeated scatterings at one site are possible and all of them must be properly accounted for in the corrections to the particle energies. In perturbation theory, the solutions to the Hamiltonian  $H_0 + U$  would be written as a power series in  $U$  involving the solution to  $H_0$ . In a similar fashion, the Green's function  $G(1,2;U)$  may be expanded as [49];

$$\begin{aligned}
 G(1,2;U) &= G_0(1,2) + G_0(1,1') U(1') G_0(1',2) \\
 &+ G_0(1,1') U(1') G_0(1',2') U(2') G_0(2',2) + \dots \quad (15) \\
 &= G_0(1,2) + G_0(1,1') U(1') G(1',2;U)
 \end{aligned}$$

This expansion may be expressed in terms of diagrams shown in figure 17(a) which are interpreted similar to those developed by Feynman.  $G(1,2;U)$  is represented as the dark solid line which describes the propagation of a particle from 2 to 1 in the presence of multiple scattering. The first term in the expansion is the unperturbed Green's function  $G_0(1,2)$  which describes the propagation from 2 to 1 without any scattering by  $U$ . The next term describes the propagation from 2 to  $1'$  without any scattering, then a single scattering occurs at  $1'$  and the particle propagates from  $1'$  to 2 without any further scatterings. As this expansion continues an additional scattering is involved with each successive term. To use these diagrams one simply writes down the unperturbed Green's function for each propagator, includes a factor of  $U$  at each vertex (represented by  $x$  in a diagram) and integrates the corresponding variables  $(1,2,\dots)$  over all time and space.

The assumption of a homogeneous distribution of defects on a macroscopic

scale can be treated by replacing  $G(1,2;U)$  with the ensemble average of many systems having the same concentration of defects [48]. This is what experiments usually measure and is denoted as  $\langle G(\mathbf{r},\mathbf{r}') \rangle$ . Since the perfect crystal Green's function is independent of the concentration or distribution of defects, the quantity  $\langle G(1,2;U) \rangle$  consists only of terms given by  $\langle U(2) \rangle$ ,  $\langle U(2)U(3) \rangle$ ,  $\langle U(2)U(3)U(4) \rangle$  etc. The average of a single scattering just adds a constant potential to the local site of the scattering, therefore the term involving  $\langle U(2) \rangle$  may be set equal to zero without any loss of generality [48]. The diagram representing the expansion of the average Green's function in powers of  $U$  is shown in figure 17(b). The term representing a single scattering event has been taken as zero. This expansion is given in terms of the Green's functions defined by equation (13), which represents propagation in space and time. Instead of working with this Green's function, Fourier transforms will allow for an expansion involving scattering events in momentum and energy. This expansion defines a quantity known as the self energy  $\Sigma$ , and is given by;

$$\langle G(\vec{k}, \omega) \rangle = G_o(\vec{k}, \omega) + G_o(\vec{k}, \omega) \Sigma(\vec{k}, \omega) \langle G(\vec{k}, \omega) \rangle \quad (16)$$

The corresponding diagrams for this expansion are shown in figure 17(c). With this definition the average Green's function for multiple scattering of single particles is;

$$\begin{aligned} \langle G(\vec{k}, \omega) \rangle &= [G_o^{-1}(\vec{k}, \omega) - \Sigma(\vec{k}, \omega)]^{-1} \\ &= [\hbar\omega - E(\vec{k}) - \Sigma(\vec{k}, \omega)]^{-1} \end{aligned} \quad (17)$$

The quantity  $E(\mathbf{k})$  in equation (17) is the energy dispersion determined by the unperturbed Hamiltonian. The poles of  $\langle G(\mathbf{k},\omega) \rangle$  are at  $\hbar\omega = E(\mathbf{k}) + \Sigma(\mathbf{k},\omega)$ ,



(a)

$$\begin{aligned}
 \overline{2 \rightarrow 1} &= 2 \rightarrow 1 + 2 \rightarrow \overset{X}{1'} \rightarrow 1 \\
 &+ 2 \rightarrow \overset{X}{2'} \rightarrow \overset{X}{1'} \rightarrow 1 + \dots
 \end{aligned}$$

(b)

$$\begin{aligned}
 \langle G(1,1') \rangle &\equiv \overline{1' \rightarrow 1} \\
 &= 1' \rightarrow 1 + 1' \rightarrow \overset{X}{3} \rightarrow 2 \rightarrow 1 \\
 &+ 1' \rightarrow \overset{X}{4} \rightarrow 3 \rightarrow 2 \rightarrow 1 + 1' \rightarrow \overset{X}{5} \rightarrow 4 \rightarrow 3 \rightarrow 2 \rightarrow 1 + 1' \rightarrow \overset{X}{5} \rightarrow 4 \rightarrow 3 \rightarrow 2 \rightarrow 1 \\
 &+ 1' \rightarrow \overset{X}{6} \rightarrow 5 \rightarrow 4 \rightarrow 3 \rightarrow 2 \rightarrow 1 + 1' \rightarrow \overset{X}{5} \rightarrow 4 \rightarrow 3 \rightarrow 2 \rightarrow 1 + \dots
 \end{aligned}$$

(c)

$$\begin{aligned}
 \overline{1' \rightarrow 1} &= 1' \rightarrow 1 + 1' \rightarrow \overset{\text{arc}}{3} \rightarrow 2 \rightarrow 1 \\
 \Sigma(1,2) &\equiv \overset{\text{arc}}{2} \rightarrow 1 = \overset{X}{2} \rightarrow 1 + \overset{X}{2} \rightarrow 1 + \overset{X}{2} \rightarrow 1 \\
 &+ \overset{X}{2} \rightarrow 1 + \overset{X}{2} \rightarrow 1 + \overset{X}{2} \rightarrow 1 + \dots
 \end{aligned}$$

Figure 17. Diagram representations of Green's functions and the self energy used in multiple scattering theory.

where  $\Sigma = \Sigma_0 + i\Sigma_1$  is complex in the  $\omega$  plane.

The local density of states  $\rho$ , can be determined from the imaginary part of  $\langle G(\mathbf{k}, \omega) \rangle$  given by;

$$\begin{aligned} \rho(\omega) &= -\frac{1}{\pi} \Im \langle G(\vec{k}, \omega) \rangle \\ &= \frac{\frac{\Sigma_1}{\pi}}{[\hbar\omega - E'(\vec{k})]^2 + \Sigma_1^2} \end{aligned} \tag{18}$$

This has the form of a Lorentzian distribution where the half-width is given by the imaginary part of the self energy,  $\Sigma_1$ . Therefore, the problem of line narrowing in the multiple scattering theory is to properly calculate the imaginary part of the self energy. The real part of the self energy contributes to a shift in the energies given by  $E'(\mathbf{k}) = E(\mathbf{k}) - \Sigma_0$ . In a weak scattering limit, this energy shift is expected to be small. It is now evident that the broadening is dependent on the density of states, and if  $|\hbar\omega - E'(\mathbf{k})| > \Sigma_1$  then the broadening will be proportional to the density of states.

The difficulty in this problem is determining the self energy resulting from all possibilities of multiple scattering. A self consistent approximation referred to as the coherent potential approximation (CPA) is used to solve for the self energy and is developed from the average T-matrix approximation (ATA) [48,50]. To understand this, let  $U(\omega)$  be defined as the time Fourier transform of the on-site disorder. The simplest approximation is called the virtual crystal approximation (VCA). In the VCA,

the Green's function may be expressed as;

$$\langle G(\omega) \rangle = G_o(\omega) + G_o(\omega) \langle U(\omega) \rangle \langle G(\omega) \rangle \quad (19)$$

$$\Sigma(\omega) = \langle U(\omega) \rangle$$

As discussed previously, the term  $\langle U(\omega) \rangle$  only adds a constant to the energies given by the unperturbed Hamiltonian. This average is real in the complex plane thus not contributing to the linewidths. This approximation is naive in that it considers only single scattering from a defect and neglects all possible repeated scatterings. In general the multiple scattering consists of repeated scatterings at one site in addition to the various scatterings between sites. In the superlattice problem, only the repeated scatterings at one site contribute to the multiple scattering. This is also the case for impurity scattering provided that the concentration of defects is small [52]. It is these repeated scatterings at each site which give rise to the line broadening caused by the disorder (interlayer fluctuations). The ATA is developed as a first order approximation to treat the repeated scatterings. By definition the T-matrix is expressed as a series in  $U(\omega)$  given by;

$$T = U(\omega) + U(\omega) G_o(\vec{k}, \omega) U(\omega) + \dots$$

$$\dots + U(\omega) [G_o(\vec{k}, \omega) U(\omega)]^n \quad (20)$$

$$T = U(\omega) G(\vec{k}, \omega) G_o^{-1}(\vec{k}, \omega)$$

The matrix representing  $G_o$  has in general non-zero diagonal and off diagonal elements. The diagonal elements represent the scatterings at one site, while the off diagonal elements represent scatterings from site to site. In the ATA, it is assumed

that  $\langle T \rangle$  is statistically independent of site-to-site scattering and that the T-matrix can be defined for each site as the repeated scatterings at that site. In the superlattice problem, it is a good assumption that site-to-site scattering is negligible since the quantum wells at each site have significant spatial separation on an atomic scale. Therefore, the Green's functions considered for the exciton line narrowing problem have only diagonal elements. The T-matrix has the general form given by;

$$T = U(\omega) [1 - G_o(\omega) U(\omega)]^{-1} \quad (21)$$

Using the definitions above it can be shown that the average Green's function and the self energies are related to the average T-matrix by;

$$\begin{aligned} \langle G \rangle &= G_o + G_o \langle T \rangle G_o \\ \Sigma &= \langle T \rangle [1 + G_o \langle T \rangle]^{-1} \end{aligned} \quad (22)$$

The ATA approximation ignores correlations in scatterings between both  $G(\omega)$  and  $T$ . The coherent potential approximation (CPA) takes the ATA logically one step forward. The idea is to start with an average Green's function to determine self energies or the T-matrix and use this to recalculate the average Green's function. Performing this self consistently results in finding an average Green's function such that  $\langle T \rangle$  vanishes. This method self consistently corrects itself until there are no further scatterings from a single site. It is believed that this method is the most accurate for studying disorder from a Green's function approach, however it is difficult to find physical problems where the solutions to CPA are easily determined [48]. One approach to solving this is an iterative (IATA) method to the ATA. It has been shown that in the weak

scattering limit, the IATA method rapidly converges to the CPA limits, and in some instances the ATA model is a good approximation [54]. According to IATA method, the self energy is given by;

$$\Sigma = \sigma + \langle T \rangle [1 + G \langle T \rangle]^{-1} \quad (23)$$

where  $\sigma$  is a complex reference potential which is adjusted until  $\langle T \rangle$  vanishes. An iteration at each site can be performed by the following expression;

$$\Sigma^{n+1} = \Sigma^n + \langle T^n \rangle [1 + \langle T^n \rangle G^n]^{-1} \quad (24)$$

In the weak scattering limit, good agreement between the IATA and the CPA can be found after a few (<10) iterations.

The application of the multiple scattering theory, derived from the subband electron and hole states, to exciton lineshapes can be done by viewing the exciton states as a linear combination of electron and hole product states at wavevector  $\mathbf{k}$  given by;

$$|\Psi\rangle = \sum_{\vec{k}} F(\vec{k}) |C, \vec{k}\rangle |V, \vec{k}\rangle \quad (25)$$

where  $|C, \mathbf{k}\rangle$  and  $|V, \mathbf{k}\rangle$  represent the conduction and valence subband states of the superlattice. In the weak scattering limit, the expansion function  $F(\mathbf{k})$  is assumed constant [38]. The matrix elements of the exciton self energy is then represented as a sum of the individual electron and hole self energies.

This is expressed as;

$$\langle \Psi | \Sigma | \Psi \rangle = \sum_{k_p, k_z} |F(k_p, k_z)|^2 (\langle k_z | \Sigma_e | k_z \rangle + \langle k_z | \Sigma_h | k_z \rangle) \quad (26)$$

where the wavevector  $\mathbf{k}$  has been decomposed into components parallel ( $k_p$ ) and perpendicular ( $k_z$ ) to the plane of the interface. The matrix elements for the electron and hole self energies are independent of  $k_p$  if only scattering from interlayer fluctuations are considered.

The electron and hole states in a 1-dimensional coupled quantum well array of infinite length can be expressed as a linear combination of "localized orbitals" one in each quantum well. In the LCAO or tight-binding models with only nearest neighbor interactions the subband dispersion is given by;

$$E(k_z) = E_0 + \frac{W}{2} [1 - \cos(k_z d)] \quad (27)$$

where  $E_0$  is the zone center subband energy,  $W$  is the band width, and  $d$  is the period of the superlattice.

The fluctuation of the barrier and well width in a SL gives rise to a random distribution of orbital energy shifts,  $U$ . In this calculation the Lorentzian distribution,  $P(U)$  truncated at three times the half width is used, where;

$$P(U) = \frac{\Delta_n}{\pi} \frac{1}{U^2 + \Delta_n^2} \quad \text{for } |U| < 3\Delta_n \quad (28)$$

The average T-matrix can then be expressed as;

$$\langle T \rangle = \int dU P(U) (U - \sigma) [1 - G_o (U - \sigma)]^{-1} \quad (29)$$

where  $\sigma$  is a complex reference potential which is adjusted until  $\langle T \rangle$  vanishes.

Since the exciton self energy is given by the sum of electron and hole self energies the half-width of the exciton transitions are given by;

$$\Gamma \equiv \Gamma_e + \Gamma_h \approx \sum_{k_z} \Sigma_e [E(k_z)] + \Sigma_h [E(k_z)] \quad (30)$$

$$\Gamma_i = \Delta_{n,i} g \left[ \frac{W_i}{\Delta_{n,i}} \right] = \Delta_{n,i} g(r_i)$$

Where  $i=(e,h)$  denote electron or hole parameters. The function  $g(r)$  is a universal function obtained by solving the CPA equations. The numerical results for  $g(r)$  are shown in figure 18, and this function can be well fitted by the analytic function, viz;

$$g(r) \approx \left[ 1 + \frac{r}{0.7} \right]^{-0.4} \quad (31)$$

which is also shown in figure 18. From table V it is evident that for the samples used in this study the subband dispersion increases much faster than the shifts in orbital energies ( $\Delta_n$ ) due to interlayer fluctuations. For example, as  $L_b$  varies from 130 Å to 31 Å, the corresponding value of  $r$  for the  $n=1$  conduction band electron changes from about 0.5 to almost 20. From figure 18 this predicts dramatic narrowing of excitons upon a reduction in  $L_b$ .

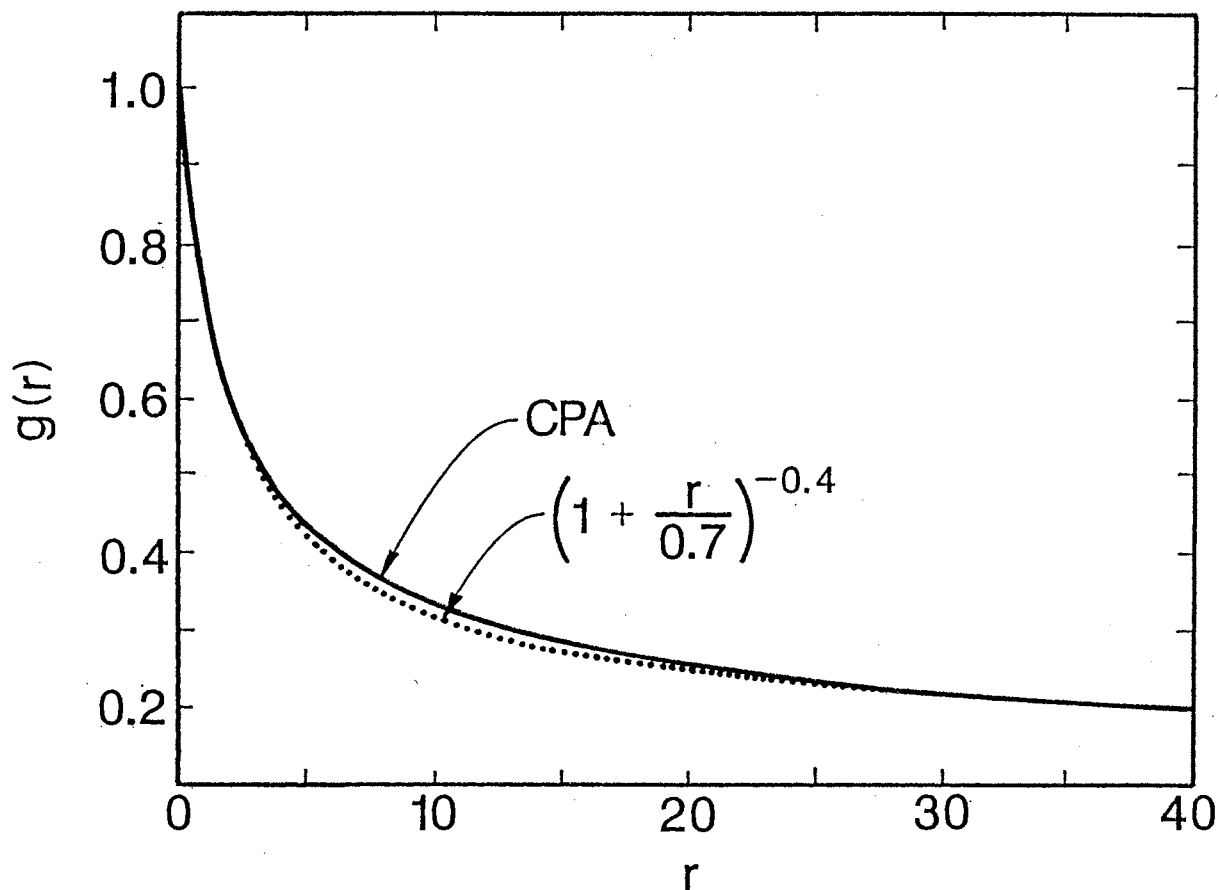


Figure 18. The numerical result for the universal function  $g(r)$  obtained by solving the CPA equations. The argument  $r$  is the ratio of the subband width to the half-width of the on-site distribution. As  $L_b$  varies from 130 to 31 Å, the value of  $r$  varies from  $\sim 0.5$  to  $\sim 17$  for the  $n=1$  conduction band (see table V). The excitonic line broadening is proportional to the function  $g(r)$ . An analytic function is also given which is a good fit to the CPA theory.



## Results and Discussion

In figures 19(a) and (b) the experimental full width at half maximum (FWHM) values for both 1HH and 1LH excitons are shown (circles) as a function of  $L_b$ . The linewidths predicted by the CPA model are given by  $2\Gamma$ . The comparison to the experimental data was made by using an adjustable parameter determined by fitting  $2\Gamma$  to the measured FWHM value of the heavy-hole exciton for the sample with  $L_b = 51 \text{ \AA}$ . The prediction given by the variance in equation (8) is shown in figure 20 along with the fit by  $g(r)$  for the 1HH exciton linewidths observed in PL data. Aside from the fact that this treatment predicts a slight increase in linewidths with a reduction in  $L_b$  it also overestimates the linewidths even in the thickest barrier samples where the subband dispersion is small. This is because the function  $g(r)$  is a rapidly changing function in the limit of zero dispersion. In the case that the dispersion is identically zero, the CPA model and the variance model are in complete agreement. The extended averaging scheme presented in reference 40 is also shown in figure 20. This is simply the period of the superlattice divided by the exciton diameter multiplied with the variance equation (8). It tends to fit the data for thicker barriers but increases away from the thinner barrier samples. This idea is naive, but its simplicity can be useful in a laboratory situation.

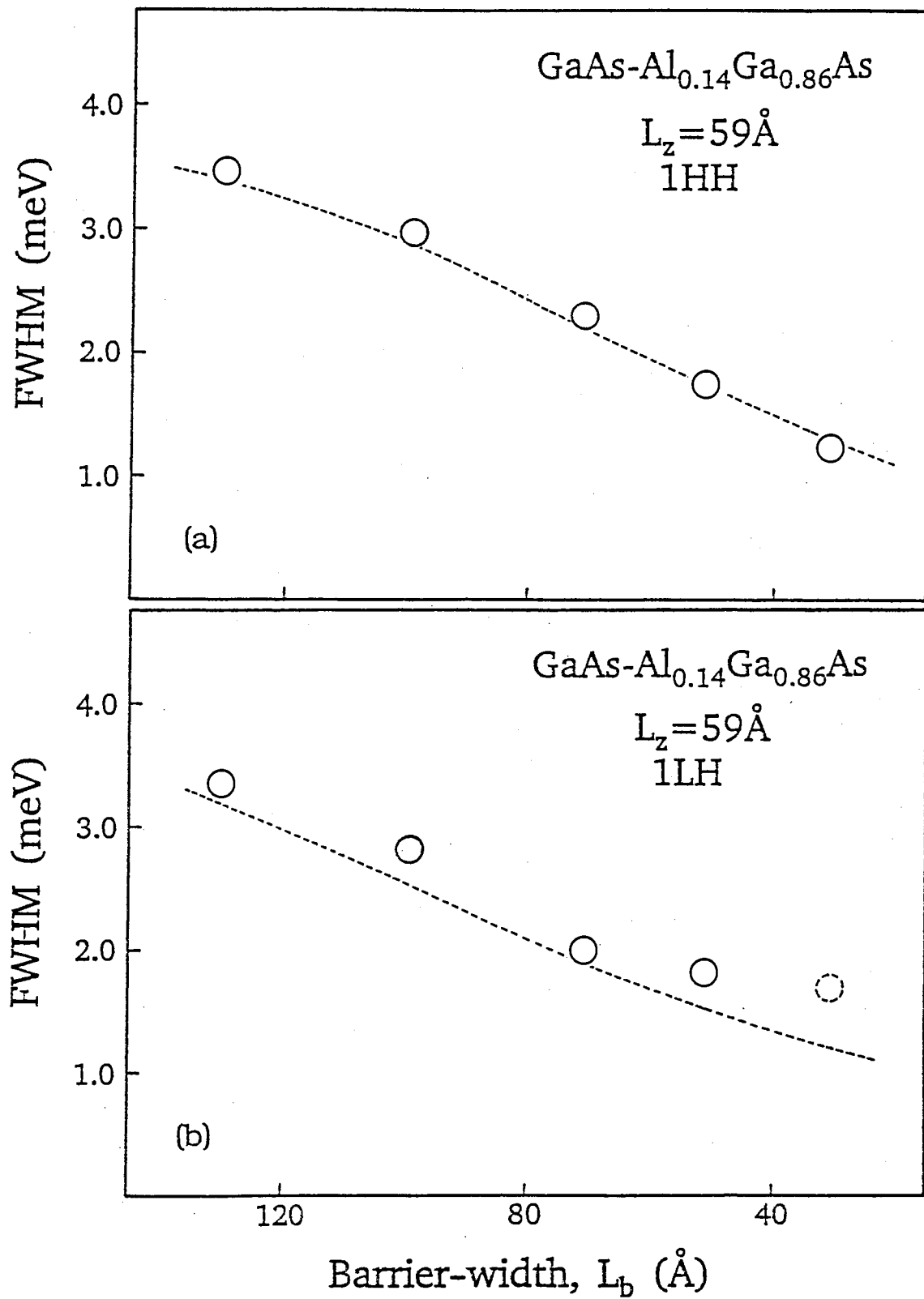


Figure 19. Experimental FWHM values and the theoretical CPA fit (dashed curve) for the (a) 1HH, and (b) 1LH excitons obtained by PLE.

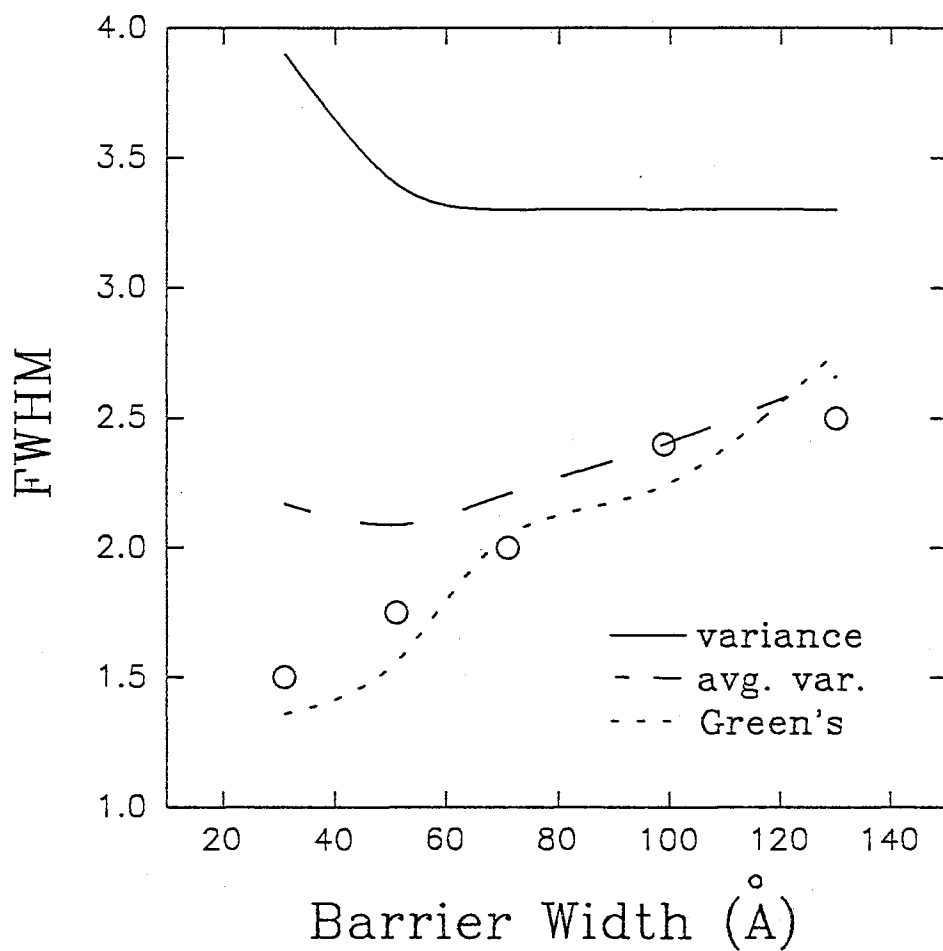


Figure 20. Experimental FWHM values of the PL (1HH exciton) taken with a He-Ne laser. The function  $g(r)$  is given by the short dashed curve. The variance fit and extended averaging scheme are shown as the solid and long dashed curves, respectively.

It is seen that the theoretical fit given by the CPA model is in excellent agreement with the results obtained experimentally. This is particularly so in the case of the  $n=1$  heavy-hole excitons. The agreement is not as good in the case of the  $n=1$  light-hole excitons. These excitons are near the excited heavy-hole exciton states and the subband continuum thus additional broadening mechanisms not discussed may be involved. The fit is not as good for the thinnest barrier light-hole exciton but this is partially due to the fact that the light- and heavy-hole exciton energies become increasingly close in addition to a reduction of the light-hole intensity as  $L_b$  decreases. The experimental linewidth for this point is then given as an upper bound estimate to the broadening caused by interlayer fluctuations.

In conclusion, a systematic study of disorder caused by interlayer fluctuations in the well and barrier widths have been studied in a series of GaAs/Al<sub>x</sub>Ga<sub>1-x</sub>As superlattices. It was found that the inhomogeneous broadening due to this disorder was dramatically reduced as the subband dispersion in a superlattice becomes larger. Qualitatively this can be understood from the fact that in the weak scattering limit the broadening will be proportional to the electronic density of states. Since the density of states becomes smaller with increasing subband dispersion, narrowing of excitonic transitions are expected with a decrease in  $L_b$  when  $x$  and  $L_z$  are held constant. Using a multiple scattering theory in the coherent potential approximation based on Green's functions excellent agreement with photoluminescence and photoluminescence excitation spectroscopy has been obtained. Since the  $n=1$  heavy-hole subband dispersion is very small compared to the other  $n=1$  subbands, in some instances the

linewidths of low temperature PL spectra may be used to estimate the  $n=1$  electron subband dispersion in high quality quantum well samples. It is always better to use PLE data to estimate subband dispersions as discussed in chapter I, however, in the event that tunable dye lasers are not available this method provides a reasonable estimate.

CHAPTER III

MULTIPLE PHONON AND FANO-TYPE  
RESONANCES IN THIN BARRIER  
SUPERLATTICES

Introduction

Resonant Raman spectroscopy (RRS) can be a useful method to study the properties of optical phonons, their interactions with excitons or carriers as well as the electronic band structure in semiconductors. The relations between these fundamental particles (or quasi-particles) are observed through the resonance Raman profile (RRP), which is defined as the intensity of the Stokes shifted Raman line plotted against the incident photon energy. Maxima are observed in the RRP when either the incident or scattered photon energy equals that of an optical transition between critical points in the band structure or that of an excitonic transition. In most cases, excitonic transitions play the dominant role in RRS as observed in both experiment and theory. If the incident (scattered) photon energy is resonant with an excitonic transition the process is called incoming (outgoing) resonance. Much work has been done where only one of the intermediate states in the Raman process is in resonance with either

the incident or scattered photons [55-68]. Several issues such as the red shift in RRP compared to photoluminescence excitation (PLE) spectra as well as differences between the strengths of incoming and outgoing resonance channels are now well understood in bulk as well as quantum well (QW) structures [65]. In addition comprehensive theoretical studies on RRS in QW structures have now been published based on recent advances in the theoretical description of optical phonons in these thin layered structures [55,56,60].

Of particular interest to this chapter is the experimental and theoretical works which have concentrated on multiple resonances, where both incident and scattered photon energies are resonant with optical transitions, and higher order Raman processes in QW structures [69-74]. Because superlattices enable the tailoring of band structures, it is possible to obtain separations between optical transitions differing by the energies of superlattice optical phonons. The few published works in this area have all concentrated on QW structures with relatively large  $\text{Al}_x\text{Ga}_{1-x}\text{As}$  barriers ( $x \approx 0.3$ ), such that the excitons, carriers, and phonons of interest are all mostly confined to the GaAs well region. In this chapter, the results of double resonance Raman scattering (DRRS) for first and second order Raman processes are presented in strongly coupled thin barrier GaAs/ $\text{Al}_x\text{Ga}_{1-x}\text{As}$  superlattices (SL's). In addition, all processes discussed involve scattering from the Brillouin zone edge to the Brillouin zone center, in contrast to those already published which involve scatterings mainly around the Brillouin zone center. The main excitonic features in this work are similar to those studied in the QW structures, however because of the unique band structure associated

only to SL's, new results are obtained which can be used to suggest the value of the exciton binding energy at the  $M_0$  critical point for 1HH excitons. In addition, structure in the PL spectra is observed higher in energy than the fundamental 1HH exciton. It will be shown that this structure results from strong mixing between the 1LH exciton and the 1HH subband continuum, similar to the effect which gives rise to the peak H discussed in chapter I. Using RRS the appearance of this structure in PL spectra and a dramatic reduction in the 1LH exciton intensity in the PLE spectra will be discussed as arising from this mixing plus the unique property of superlattices, namely subband dispersion along the  $k_z$  direction. Before proceeding with this, a lengthy introduction to Raman scattering in superlattices is presented.

## Optical Phonons in Superlattices

It has been well established both experimentally and theoretically that GaAs and AlAs optical phonons in GaAs/AlAs QW structures are confined to their respective layers (see reference 75 for a review on this topic). The origins of this confinement can be seen from the bulk phonon dispersion curves of GaAs and AlAs. As shown in figure 21, there is an energy gap between the dispersion curves of the optical phonons in GaAs and AlAs, and thus each mode is unable to propagate outside its respective layer width. Because of this, the optical phonons in GaAs/AlAs QW structures are confined on a length given by the well-widths ( $L_z$ 's) or barrier-widths ( $L_b$ 's). The GaAs and AlAs phonons wavevector component along the (001) growth direction is then given



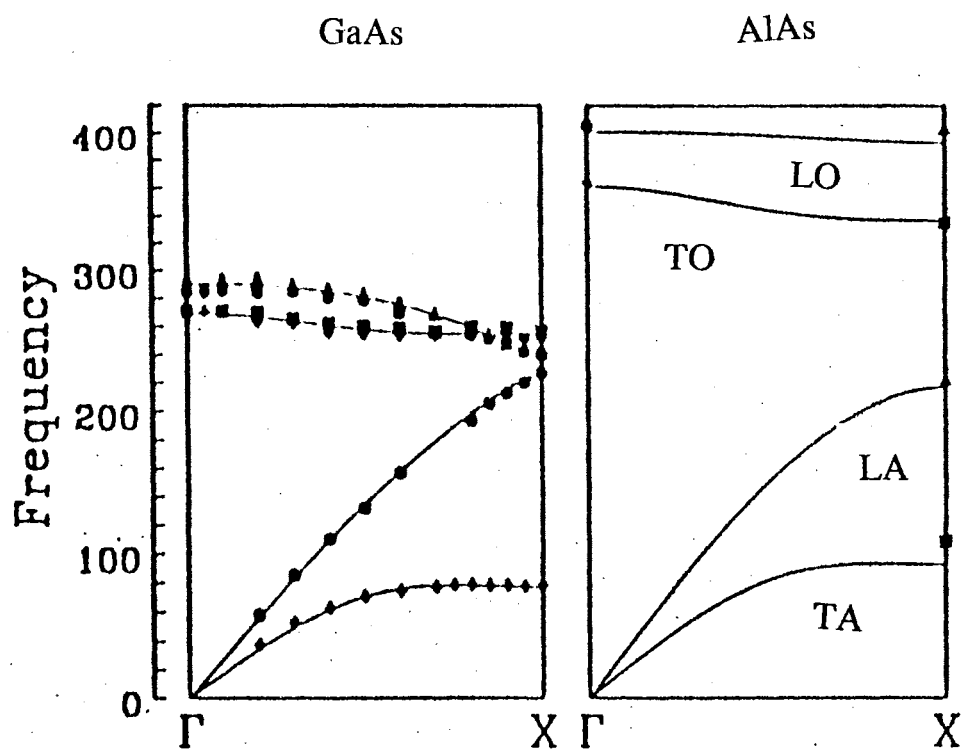


Figure 21. Dispersion curves of the optic phonons in bulk GaAs and AlAs. The gap between the dispersion curves of GaAs and AlAs phonons gives rise to optical phonon confinement.

by  $q = n\pi/L_z$  and  $q = n\pi/L_b$ , respectively, where the frequency of these modes have been shown to map well onto bulk phonon dispersion curves [58,75]. The optic phonons in GaAs/AlAs MQW's are almost perfectly confined to their respective layers as they are damped out within approximately one monolayer beyond the interfaces. It has recently been confirmed through time resolved Raman measurements and theoretical electron-phonon scattering models that the confined LO mode displacements are symmetric about reflection through the midplane of the GaAs or AlAs layers for the odd  $n$  modes, and they are antisymmetric about the same reflection for the even  $n$  modes [75-77]. These confined optic phonons in GaAs/Al<sub>x</sub>Ga<sub>1-x</sub>As superlattices have been the subject of much current debate.

In much the same way that electrons are considered to couple in superlattices by overlapping wavefunctions, the coupling of longitudinal optic (LO) phonons has been observed in GaAs/Al<sub>x</sub>Ga<sub>1-x</sub>As superlattices [78]. The effect of alloying on the optical phonon dispersion curves is to lower in energy and flatten out the dispersion, in addition to having modes similar to those in the binary GaAs and AlAs compounds, i.e. there exist two modes which are GaAs-like and AlAs-like in nature [75]. It was determined that in GaAs/Al<sub>x</sub>Ga<sub>1-x</sub>As superlattices, the penetration of the GaAs LO phonons into Al<sub>x</sub>Ga<sub>1-x</sub>As barriers ( $x \leq 0.4$ ) could be large enough that when the  $L_b$ 's decrease significant spatial overlap of the phonon wavefunctions exists. In addition for  $x < 0.2$ , the dispersion curves between the GaAs LO phonons and the GaAs-like LO phonons overlap significantly, such that the confined phonons are capable of propagating throughout the superlattice [78].

## Electron-Phonon Interactions in Polar Superlattices

The interaction of a carrier with a phonon mode in superlattices can be correctly modeled from two fundamental scattering processes, these are the deformation potential (DP) and the Fröhlich (F) interactions. The DP scattering process is caused by the local distortion of the lattice due to an optic phonon mode. This distortion perturbs the periodicity of the crystal potential that a carrier in the lattice is subject to. Using linear approximations, the change of the lattice periodic potential,  $U(\mathbf{r})$  can be expressed as the inner product between  $U(\mathbf{r})$  and the phonon displacement,  $\mathbf{u}$ . Consequently it can be shown theoretically that the DP interaction only operates on the hole subband states, and scatters only between states that differ in angular momentum,  $j$  by 1 [55]. For example, a heavy-hole  $j=3/2$  state can only scatter into a light-hole  $j=1/2$  state under the deformation potential. In this case, the valence band edge functions used to describe the hole states requires that the displacement of the phonon mode must be symmetric about the midplane of the layer for nonvanishing DP matrix elements. Because of this, only the odd  $n$  modes participate in DP scattering [55].

The Fröhlich (F) scattering process between a carrier and a phonon mode describes the interaction of a carrier with the macroscopic electric field associated only with LO phonons. It can be shown that this electric field is proportional to the phonon displacement, such that the gradient of the corresponding scalar potential is proportional to the LO phonon displacement. The Fröhlich Hamiltonian is just  $e\phi(\mathbf{r})$ ,

where  $e$  is the charge of an electron and  $\phi(r)$  is the macroscopic potential associated with the LO phonon. The ordinary intraband F-process can involve scattering of either conduction band electrons or valence band holes. Since the matrix elements of the F-process depends on the phonon wavevector,  $\vec{q}$  which is defined as the difference between the initial and final wavevectors of the carrier states defined by the intraband scattering, it is dipole forbidden in bulk semiconductors. In the dipole approximation for Raman scattering in solids, the phonon wavevector is defined by the difference in incident and scattered photon wavevectors and is practically zero. However, the intraband F-process is no longer dipole forbidden in superlattices because of the large phonon wavevector associated with confinement. In Raman scattering of phonons in superlattices, only the phonon wavevector components parallel to the growth direction are operative. Therefore, a phonon mode with  $q_z$  as large as the Brillouin zone can be Raman active as long as the parallel component,  $q_{xy}$  is nearly zero. Since the initial and final carrier states involved in the intraband F-process are by definition from the same subband states, only the symmetric phonon potentials (antisymmetric displacements) given by the even  $n$  modes can participate in the intraband F-process [55].

In superlattices, it is well known that strong mixing between the hole subband states is possible [55,70]. In most QW structures this may involve the mixing between the  $n=1$  light- and heavy-hole states at the Brillouin zone center. Also, the mixing between the  $n=1$  light-hole and  $n=2$  heavy-hole at the Brillouin zone edge has been clearly observed in MQW and SL structures [79]. In these cases, the band-mixing can

give rise to an F-process for the hole subbands involving the scattering between different subbands ( $\Delta n \neq 0$ ) similar to the DP process [55,68,69]. This forbidden interband F-process is unique only to superlattices and is observed for wavevectors  $\mathbf{k}$  such that the two different subbands are separated by the energy of an LO phonon in the superlattice. Since this interband F-process involves initial and final states from two different subbands, only the antisymmetric potentials associated with macroscopic electric field of LO phonons given by odd  $n$  can participate in the scattering process. In contrast to the DP process, the forbidden interband F-process makes no stipulation on the angular momentum of the initial and final hole states [55]. This is because the angular momentum of mixed light- and heavy-hole states should generally involve that of both hole states.

Finally, there is one more Fröhlich interaction which has been observed experimentally in both bulk and superlattice structures, and is described well theoretically [55,68,75]. This is the impurity induced Fröhlich (FI) process, which is an important scattering process in bulk polar semiconductors as well as superlattices. It is this FI-process which has been attributed to the cause of the asymmetry between incoming and outgoing resonances [62]. It has been shown theoretically that the FI-process has the same symmetry as the intraband F-process, such that only even  $n$  modes can participate in this scattering process for superlattice phonons.

## Raman Tensors and Selection Rules

In a Raman backscattering configuration where the incident photon wavevector is parallel to the superlattice axis (z-axis), the long wavelength optic modes of interest are polarized essentially along the z-axis for the LO modes. The TO modes are of two types, those which are parallel and perpendicular to the  $q_{xy}$  - z plane and will be denoted as TO1 and TO2 modes respectively. If  $q_{xy}$  is assumed to be along the y-axis of crystal, the TO1 modes are essentially polarized along the y-axis. These polarization features for the LO and TO1 modes are radically different from that in bulk materials. The LO modes are perpendicular rather than parallel to the operative wave vector, and the TO1 modes a polarized parallel rather than perpendicular to the operative wavevector. This is because the phonon wavevector component,  $q_z = n\pi/d$ , in the direction of confinement is purely formal [55].

In the  $D_{2d}$  point group described by table II in chapter I, the intraband F-process has  $A_1$  symmetry whereas the DP-process has  $B_2$  symmetry. The Raman tensors for the  $A_1$  and  $B_2$  phonons with respect to the (x,y,z) crystal axis are given by;

$$T_{A1} = \begin{pmatrix} a & 0 & 0 \\ 0 & a & 0 \\ 0 & 0 & b \end{pmatrix} \quad T_{B2} = \begin{pmatrix} 0 & d & 0 \\ d & 0 & 0 \\ 0 & 0 & 0 \end{pmatrix} \quad (32)$$

where the coefficients represent the Raman polarizabilities. The different coefficients a and b in the Raman tensor for the  $A_1$  phonons (intraband F-process) is due to superlattice anisotropy [58]. Therefore, the intrasubband F-process is expected to appear in polarized Raman spectra, whereas the DP-process is expected to appear in

depolarized Raman spectra. Let the polarization of the incident and scattered photons be denoted by  $x$  or  $y$ , and the incident and scattered photon wavevector directions be denoted by  $z$  and  $z'$  respectively, then the polarized spectra can be represented as  $z(x,x)z'$  and the depolarized spectra can be represented as  $z(x,y)z'$ . The definitions of the  $(x,y,z)$  crystal axis are usually given as  $x = [100]$ ,  $y = [010]$ , and  $z = [001]$ . The various allowed Raman scatterings for superlattice phonons in the different light scattering geometries are summarized in table VI. In backscattering geometries only the  $LO_n$  phonon modes are allowed to participate in either the F- or DP-processes. In addition to these light polarization selection rules, two other Raman selection rules must also be considered. These selection rules are statements of conservation of crystal momentum and energy and given respectively for Stokes Raman scattering by;

$$\vec{k}' - \vec{k} = \vec{q} \quad (33)$$

$$E' - E = \hbar \omega_{\vec{q}}$$

In the first expression,  $\mathbf{k}$  ( $\mathbf{k}'$ ) denotes the initial (final) particle states, and  $\mathbf{q}$  is the phonon wavevector. The conservation of crystal momentum given by this expression only applies if there exists translational symmetry. Since the phonon confinement along the superlattice axis destroys this symmetry, this selection rule is relaxed for Raman scattering processes involving  $q_z = n\pi/L$ . Therefore only the parallel component  $q_{xy}$  is operative in superlattice Raman scattering. The second expression is a statement of conservation of energy, and simply requires that the energies of the initial and final particle states in Raman processes be separated by the scattering phonon energy. For example, if the electron subband dispersion along the superlattice

TABLE VI  
 ALLOWED RAMAN SCATTERINGS FOR  
 VARIOUS PHONON MODES, SCATTERING  
 PROCESSES AND POLARIZATIONS

Polarization	Phonon and Parity	Interaction
(xx)	LO even n	F
(yy)	LO even n	F
(zz)	LO even n	F
(xy)	LO odd n	DP
(yx)	LO odd n	DP
(xz)	TO <sub>1</sub> odd n	DP
(zx)	TO <sub>1</sub> odd n	DP
(yz)	TO <sub>2</sub> even n	DP
(zy)	TO <sub>2</sub> even n	DP

axis is greater than  $\hbar\omega_{LO}$  Raman scattering by the F-process will be allowed for any value of  $q_z = n\pi/L$  satisfying the conservation of energy requirement.

The dimensionless Raman tensor for first order (one phonon) scattering by phonons is usually expressed as [55];

$$\vec{R} = N^{-\frac{3}{2}} m_e^{-1} \sum_{\alpha, \beta} \frac{\langle 0 | H_R^s | \beta \rangle \langle \beta | H_{ph} | \alpha \rangle \langle \alpha | H_R^i | 0 \rangle}{(E_o - E_\beta - \hbar\omega_q) (E_o - E_\alpha)} \quad (34)$$

where 0,  $\alpha$ , and  $\beta$  denote the particle ground state and two excited states.  $E_o$  is the incident photon energy, and  $E_\alpha, E_\beta$  are the transition energies of the corresponding



intermediate states.  $H_R^i$  and  $H_R^s$  are the Hamiltonians for the absorption and emission of the incident and scattered photons, and  $H_{ph}$  is the particle-phonon interaction Hamiltonian. The numerator of this tensor describes the Stokes Raman scattering process as follows:

- (i) An incident photon is absorbed exciting a particle from its ground state into an intermediate state  $\alpha$ ;
- (ii) The particle in state  $\alpha$  is then scattered into a second intermediate state,  $\beta$  through the interaction with a phonon;
- (iii) The particle in state  $\beta$  then relaxes back to the ground state and emits scattered light differing in energy from the incident light by the scattering phonon energy.

If either intermediate state corresponds to an optical transition, then one of the corresponding terms in the denominator vanishes causing a strong resonant enhancement. In most Raman scattering experiments utilizing the resonant effect, the dominate features in the resonant Raman spectra are associated with excitonic states [60].

Resonant Raman scattering has been well studied both experimentally and theoretically in GaAs/Al<sub>x</sub>Ga<sub>1-x</sub>As superlattices [75]. In the backscattering geometry and in off-resonance situations, even  $n$  LO phonon modes are observed in the polarized spectra due to the F-process, and odd  $n$  LO modes are observed in the depolarized spectra due to the DP-process. However, it has been observed that only even  $n$  LO modes appear in the Raman spectra near resonance, and are dominant in

polarized configurations. Although, the even  $n$  LO modes can also be observed in the depolarized spectra near resonance. The standard F-process should only be observed in polarized spectra, therefore an additional scattering mechanism must be considered to explain the weaker depolarized spectra. It was suggested that the FI-process is responsible for the weak appearance of the even  $n$  LO modes in the depolarized spectra. In this case the Raman tensor in equation (34) has to be modified to include an additional matrix element in the numerator describing the exciton-impurity scattering as well as an additional energy denominator. The behavior of the depolarized spectra can then be explained in terms of double resonance effects. Both even and odd  $n$  TO modes have also been observed in the polarized spectra near resonance. These phonon modes are symmetry forbidden in Raman backscattering geometries, but experiments suggest that they become allowed under extreme resonance conditions. It is thought that the forbidden TO Raman scattering is also due to impurity scattering, as has been observed in bulk doped GaAs [55,58].

Using an iterative perturbation technique, the Raman tensor for second order (two phonons) Stokes scattering can be expressed as [68];

$$\vec{R} = N^{-\frac{3}{2}} m_e^{-1} \sum_{\alpha, \beta, \gamma} \frac{\langle 0 | H_R^s | \gamma \rangle \langle \gamma | H_{ph} | \beta \rangle \langle \beta | H_{ph} | \alpha \rangle \langle \alpha | H_R^i | 0 \rangle}{(E_\alpha - \hbar\omega_{q_2} - E_\gamma) (E_\alpha - \hbar\omega_{q_1} - E_\beta) (E_\alpha - E_\alpha)} \quad (35)$$

where the notation is the same as that in equation (34) but now there is an additional intermediate state,  $\gamma$ . Since two phonons participate in this process they are denoted as  $q_1$  and  $q_2$ , which in general need not be the same phonon mode. In second order Raman scattering, the F-process involving two LO modes is also forbidden in the

depolarized configurations, even when heavy- and light-hole mixing is taken into account [55]. Although, if multiple resonances occur this symmetry forbidden scattering can be observed in the depolarized configuration [69-71].

From equation (34) doubly resonant first order Stokes Raman scattering can occur if  $\alpha$  and  $\beta$  correspond to optical transitions at the critical points. Similarly, second order Stokes Raman scattering can be doubly or triply resonant depending on whether any two or all three intermediate states correspond to optical transitions at critical points. It is not absolutely necessary that an intermediate state corresponds to an optical transition at a critical point to have multiple resonances, provided that one of the scatterings involves the FI-process [68].

## Experiment and Results

Photoluminescence (PL), photoluminescence excitation (PLE), and resonant Raman scattering (RRS) spectroscopies have all been used to investigate the subband structure in a thin barrier GaAs/Al<sub>x</sub>Ga<sub>1-x</sub>As superlattice. The parameters of the SL structure were designed to produce significant well-to-well coupling between particle wavefunctions of adjacent quantum wells. The particular structure studied is described in table V as sample E (page 36). It is worthy to note that the calculated dispersion for the n=1 electron and n=1 light-hole subbands are very near the energies of bulk LO (36.6 meV) and TO (33.7 meV) phonons in GaAs. The calculations in table V are based on a tight binding approximation (TBA) using a band offset ratio of 65/35. If a

70/30 band offset ratio is instead used the corresponding subband dispersions for the electron and light-hole subbands are  $W_{1e} = 36.6$  meV and  $W_{1lh} = 33.4$  meV. The value used for this offset ratio in GaAs/Al<sub>x</sub>Ga<sub>1-x</sub>As superlattices is often in the range listed above. In principle, it can be expected that strong multiple resonant phonon scattering between particles at the  $M_0$  and  $M_1$  critical points of the  $n=1$  subband structure can occur in this SL.

Another intriguing issue to consider in any strongly coupled superlattice is the transition energies of the discrete excitons and continuum subband states. As the barrier-widths ( $L_b$ 's) decrease the exciton binding energies approach the limiting bulk GaAs value of  $\approx 4$  meV. In addition the energy separation between the heavy-hole and light-hole subbands at the Brillouin zone center ( $k=0$ ) will decrease until they practically merge as in bulk GaAs. Therefore, in strongly coupled GaAs/Al<sub>x</sub>Ga<sub>1-x</sub>As superlattices it is possible that the light-hole exciton transition energy to be nearly overlaps the 1e-1HH subband continuum energies at the zone center. This phenomena has been studied theoretically and can be categorized as a Fano-type resonance [80,81].

The experimental setup is identical to that in figure 14 of chapter II. The PLE spectra in the vicinity of the  $n=1$  excitons is taken using a photomultiplier tube (PMT) in conjunction with photon counting equipment. The dye laser is continuously scanned using stepper motors interfaced to a personal computer. The PL and RRS spectra are obtained using a liquid nitrogen cooled charge-coupled device (CCD) detector. The dye laser is tuned by hand to obtain the resonant Raman profile

determined by analyzing the CCD data.

## Results and Discussion

All of the spectra acquired using the various optical techniques have been obtained at temperatures near 15K. In figure 22(a) the PL spectra of sample E is shown using an excitation energy near 1.96 eV produced by a 5mW He-Ne laser. The strongest peak centered near 1.554 eV is associated with the decay of the 1HH exciton. This peak is often red shifted slightly from the 1HH transition observed in PLE spectra. In high quality GaAs/Al<sub>x</sub>Ga<sub>1-x</sub>As superlattices, this is generally the only QW related peak observed by conventional PL techniques at cryogenic temperatures. In this sample however, an additional weaker peak is clearly resolved at higher photon energies than the 1HH peak and is centered near 1.56 eV. The first reaction is to assign this peak to the 1LH exciton and try to understand why it appears in the PL spectra. One simple method to test this assignment is to employ circular polarization photoluminescence measurements. Using a Fresnel (FAD) prism assembly, the linear polarized light from a laser can be converted into circular polarized light and then used as the excitation source. Since the light-hole subband states differ from the heavy-hole subband states in their total angular momentum by  $\pm 1$ , the luminescence will be right hand (+) circularly polarized for light-hole excitons and left hand (-) circularly polarized for the heavy-hole excitons. The polarization of the PL can then

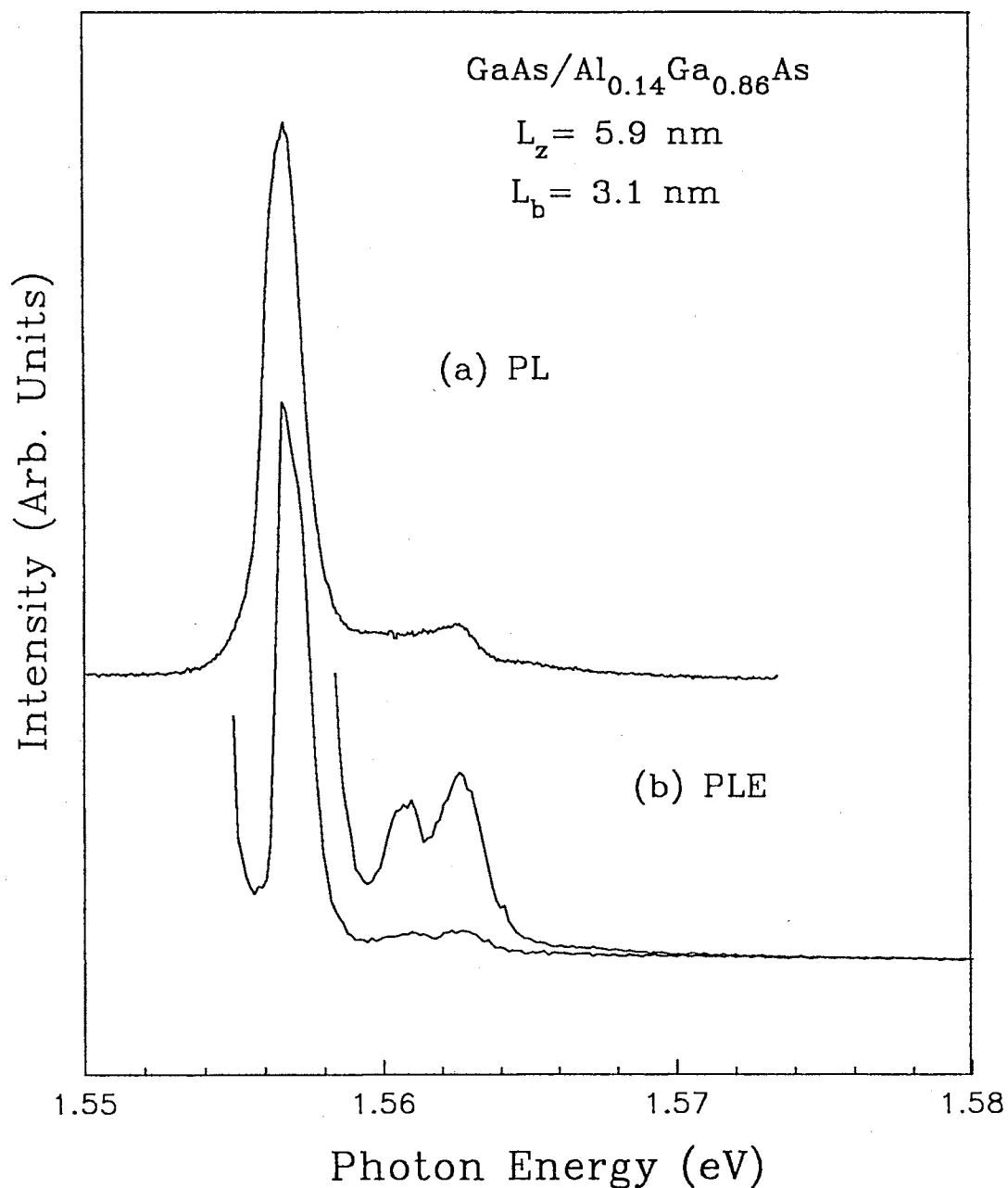


Figure 22. (a) Photoluminescence (PL) and (b) photoluminescence excitation (PLE) spectra taken from a thin barrier GaAs/Al<sub>0.14</sub>Ga<sub>0.86</sub>As SL. The PL spectra was obtained using a He-Ne laser and the PLE spectra used Styryl 8 dye in a tunable dye laser. The PL spectra is blue shifted slightly to coincide with the maximum of the 1HH exciton in the PLE spectra. The laser powers used are for both measurements are near 5mW.

be analyzed with a Babinet-Soleil compensator. Using the dye laser at photon energies near 1.6 eV and a He-Ne laser, tentative measurements indicate that the higher energy PL peak has circular polarization properties similar to that of the primary 1HH PL peak. However, because of the probable Fano-like resonance in this sample, the angular momentum associated with the light-hole exciton and 1e-1HH subband continuum may intermix similar to that occurring in the  $n=1$  light-hole and heavy-hole subband mixing.

Standard PL measurements are limited in the ability to describe superlattice band structures since the 1HH exciton is usually the only radiative recombination channel. In order to probe the higher energy quantum states of a superlattice, excitation spectroscopies such as PLE and RRS must be employed. In figure 22(b), PLE spectra clearly displays three peaks. The dominant low energy peak arises from the 1HH exciton. The two peaks near 1.56 eV are assigned to the 1LH exciton and the peak H originating from the mixture of the 2s excited 1HH exciton and heavy-hole subband continuum, (see chapter I). The separation between H and 1LH is  $\approx 1.8$  meV, and therefore a Fano-type resonance probably exists. A comparison of the PL and PLE spectra in figure 22, suggests that the higher energy structure in the PL spectra arises from the Fano-type resonance.

Scanning the dye laser output over the range from  $\approx 1.59$  eV to  $\approx 1.66$  eV in conjunction with a CCD detector allows for simultaneous excitation spectra involving phonon assisted transitions and the resonant Raman profile (RRP) to be obtained. Representative data with incident photon energies in the vicinity of the first and

second order multiple resonant Raman spectra are shown in figure 23 and figure 24 respectively. This 3-D excitation spectra will reveal excitation (PLE) spectra by plotting the intensity of any specific emission energy (wavelength). On the high energy side of the dominant PL peak in figure 23, a small dip can be observed in all spectra. This is an artifact produced by slow response of a pixel in the 2D CCD array and is a good guideline displaying the direction of the excitation spectra. The resonant Stokes shifted Raman line is seen sweeping to higher luminescence energies with increasing incident photon energy. The resonance resonant Raman profile (RRP) is obtained by plotting the intensity of the Stokes shifted Raman line versus the incident photon energies.

The RRP taken with photon energies in the vicinity of the first order multiple resonant Raman process is shown in figure 25. The lineshape of this spectral profile is nearly identical to the PL spectra taken in the off-resonance condition shown in figure 22(a) and is Stokes shifted by  $\approx 35.2 \pm 0.5$  meV. One noted feature is the shoulder on the high energy side of strongest peak, associated with resonances involving the 1HH exciton. The separation between the maxima of this peak and the high energy shoulder is  $\approx 1$  meV. It will be shown by the excitation spectra obtained from figure 23 that this dominant peak in the RRP is actually composed of three equally strong peaks each separated by  $\approx 0.5$  meV. The cause of this can be traced to monolayer fluctuations as discussed in chapter II. The fact that these peaks are so sharp is a direct consequence of smooth interfaces and large subband dispersion present in this high quality SL sample.



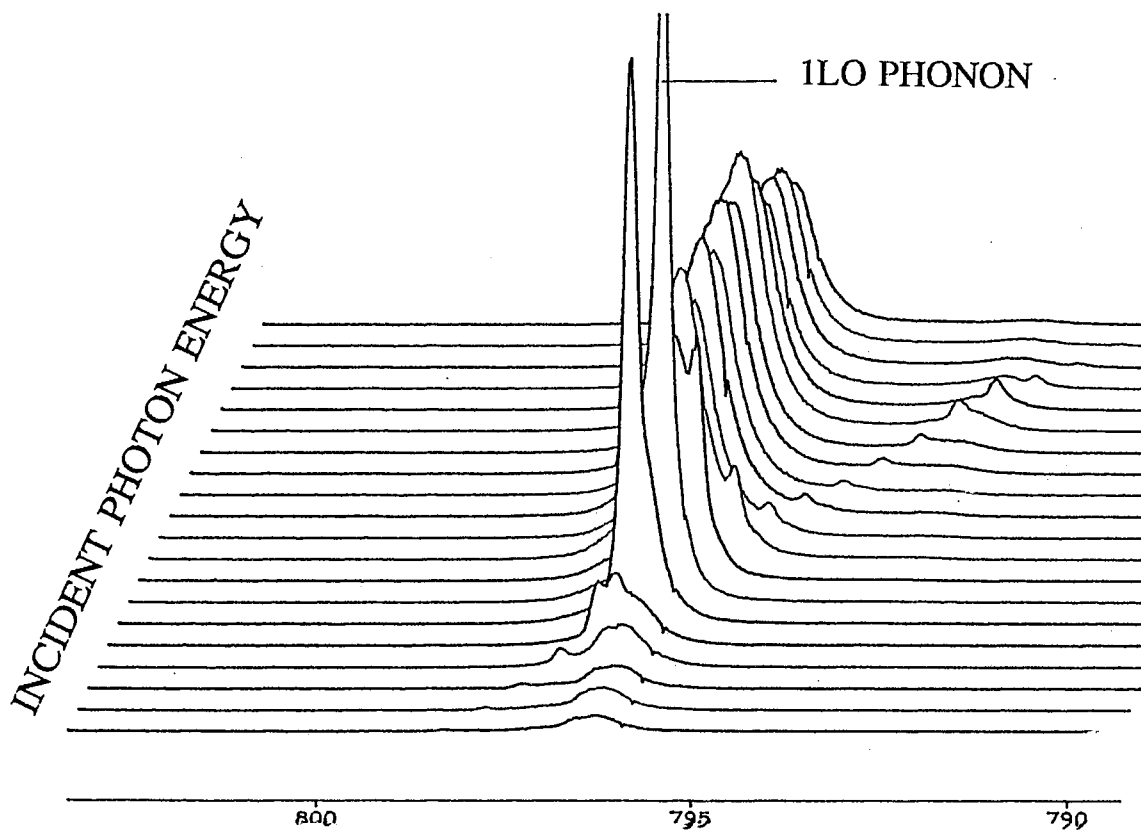


Figure 23. Photoluminescence spectra versus incident photon energies within the range from 1.58 eV to 1.61 eV. These photon energies are those in the vicinity of the first order multiple resonant Raman process. PLE excitation spectra is obtained by slicing this 3D plot perpendicular to the PL energy axis. The corresponding RRP is obtained by slicing this 3D plot along the line which is a constant phonon energy lower than the incident photon energy axis.

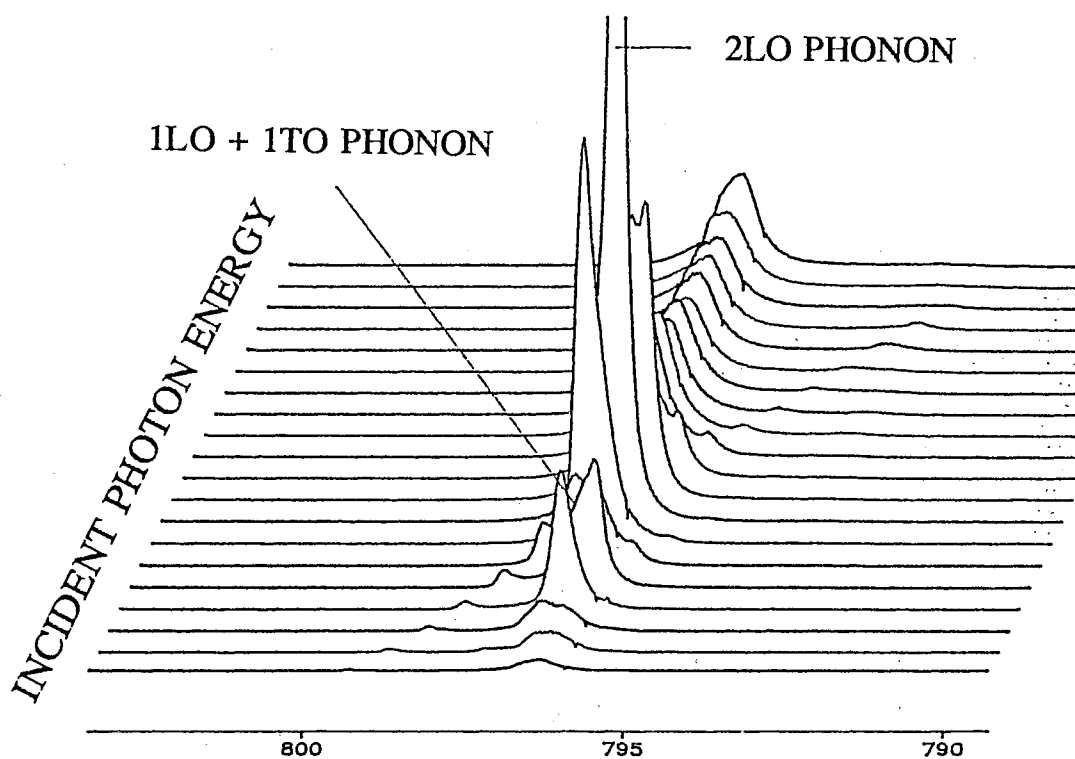


Figure 24. Photoluminescence spectra plotted versus incident photon energy within the range of 1.62 eV to 1.64 eV corresponding to the second order multiple resonant Raman process. The PLE spectra and RRP are obtained similar to that described in figure 23.

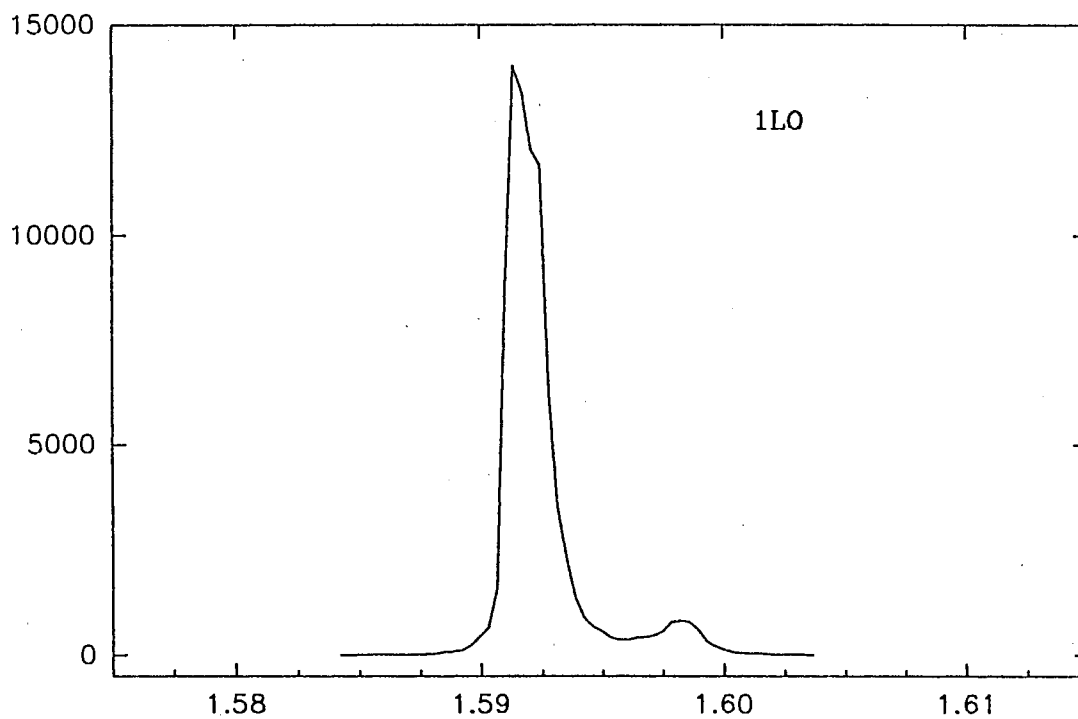


Figure 25. Resonant Raman profile obtained with incident photon energies corresponding to the first order multiple resonant Raman process. This process will be shown to involve simultaneous incoming and outgoing resonances associated with the  $1e$  and  $1hh$  subbands at the  $M_0$  and  $M_1$  critical points.

The most useful feature of this double RRP is seen in the fact that the relative intensity between the peaks associated with 1HH and the Fano resonant related peak is approximately the same as that observed in the PL. Resonant Raman profiles from singly resonant Raman scattering in GaAs/AlAs ( $L_z=46\text{\AA}$ ,  $L_b=41\text{\AA}$ ) superlattices have shown that the intensity of the outgoing 1HH exciton is 6000 times that of the 1LH exciton outgoing resonance, whereas PLE spectra revealed the corresponding intensity ratio to be no greater than 4 [65].

The cause of the 6000 times reduction in the RRP was said to be due to the decreased exciton phase coherence lifetime of the 1LH excitons. Since Raman scattering is a coherent, multistep process, its efficiency decreases with the lifetimes of the intermediate states involved. Excitons in quantum wells have a finite phase coherence lifetime, meaning the lifetime in a particular  $k$  state due to scattering, which defines the homogeneous linewidth [65]. In the particular RRP of reference 65, the scattering of excitons were suggested to be induced by acoustic phonons and structural or impurity disorder defect. From studies in GaAs/Al<sub>0.3</sub>Ga<sub>0.7</sub>As single quantum well structures using time-resolved degenerate four wave mixing (DFWM) the effects of acoustic phonons, incoherent excitons, and free carriers on exciton dephasing became clear [82]. The 1HH and 1LH dephasing rates are almost the same for thick  $L_z$ 's (300 Å), whereas the 1LH exciton dephasing rates in thin  $L_z$ 's ( $\leq 70\text{\AA}$ ) are larger than those of the 1HH exciton by nearly a factor of 5 [82]. A behaviour like this is expected when a well defined energy overlaps with a continuum of other states as described in the Fano-Anderson model [82]. Below  $L_z = 130\text{\AA}$  in single GaAs QW's

the 1LH exciton overlaps energetically with the heavy-hole continuum states and because of valence subband mixing away from the  $\Gamma$ -point a coupling of light and heavy-hole states exists. The light-hole exciton transition is then described by a Fano-type resonance [82]. The results of PL and PLE measurements shown in figure 22 suggest that a Fano-type resonance between the 1LH exciton and the 1HH subband continuum states is also present in this strongly coupled SL sample. Therefore, 1LH exciton transitions in this sample can be expected to involve shorter dephasing times than that of the 1HH exciton. Since the first order double resonance Raman profile is a coherent process, then the weaker higher energy peak may be attributed to 1HH subband-like states, because 1LH exciton-like states should be weak in the RRP due to the decreased exciton phase-coherence lifetime relative to that of the 1HH exciton. Therefore, we can conclude that the additional peak appearing in the PL of sample E arises from the Fano resonance between the 1LH exciton and the 1HH subband continuum. Much like the description of peak H in PLE (chapter I), this resonance is expected to cause a redistribution in the oscillator strengths of the 1HH subband continuum resulting in photoluminescence. In fact, the peak H is itself a Fano-type resonance involving the 2s excited state of the 1HH exciton and the 1HH subband continuum.

A plot of the PL intensities versus  $L_b$  is shown in figure 26 as the filled circles for the series of samples studied in this thesis. The decrease in intensity by more than three orders of magnitude can possibly be due to carrier diffusion from the QW region due to the strong overlap of wavefunctions. The intensities of the 1HH excitons

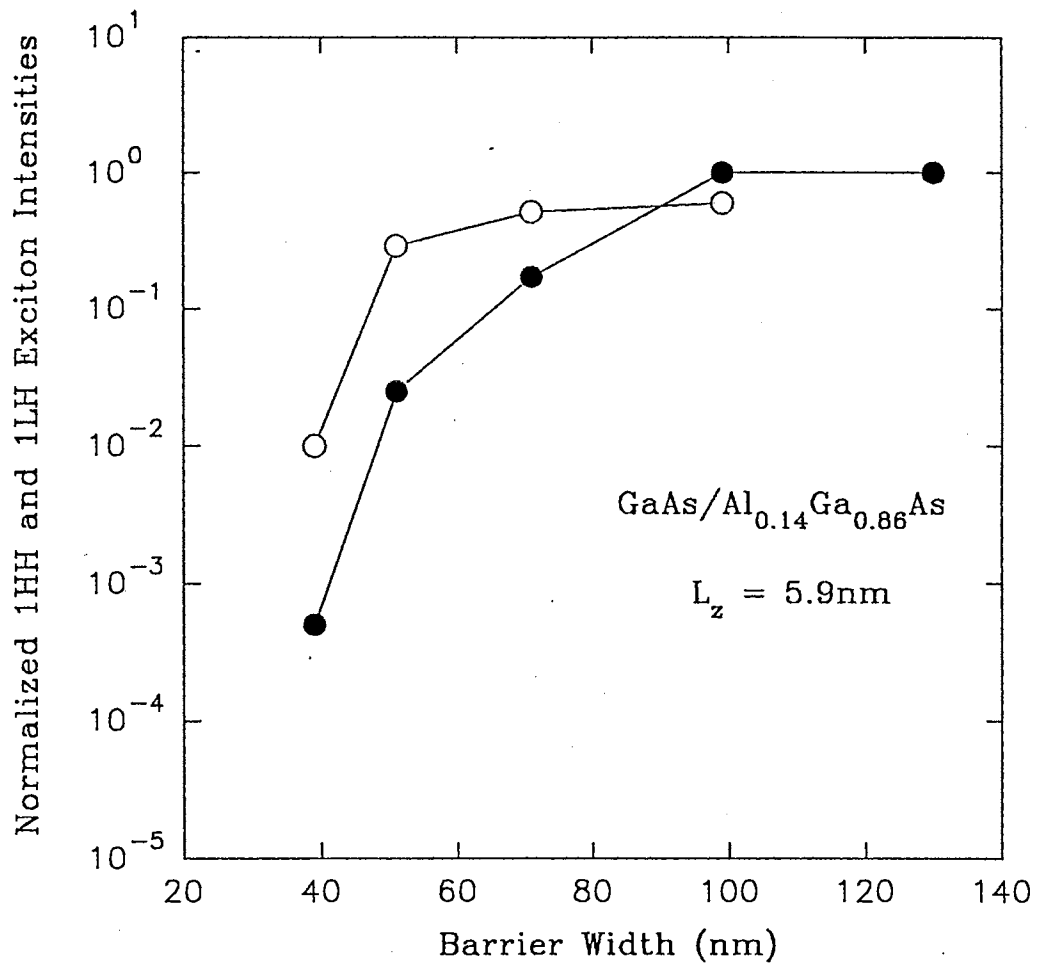


Figure 26. 1HH exciton intensities from PL (filled circles) and relative 1LH to 1HH exciton intensities from PLE (open circles) plotted against the barrier widths of the sample studied in this thesis.

relative to the 1HH excitons is also shown in this figure as the open circles. Below  $L_b = 50 \text{ \AA}$ , a nearly two order of magnitude decrease is observed for the 1LH exciton relative to the 1HH exciton. This difference has not been accounted for in present theories on exciton lineshapes. This work suggests that the additional reduction in the 1LH intensities could be due to the Fano resonance between the 1LH exciton and the 1HH subband continuum together with the SL subband dispersion.

The excitation spectra obtained from the raw data like figures 23 and 24 is shown in figure 27. Signatures of up to third order multiple resonant Raman processes involving allowed LO and forbidden TO phonon scattering were observed. In figure 27 the intensity of the PL emission energy  $\approx 1.556 \text{ eV}$  (796.6 nm) is plotted versus the incident photon energies. This PL emission energy corresponds to that of the 1HH exciton spectra maximum. In figure 28 a similar plot is given for the PL emission energy  $\approx 1.562 \text{ eV}$  (793.8 nm) corresponding to the small peak associated with the Fano-type resonant peak. The sharp peaks in figure 27 correspond to doubly resonant Raman scattering effects. Therefore, the energy positions of these peaks will move along with the monitored position. If any structure is related to optical transitions, their energy positions will remain constant regardless of the monitored PL positions. This was observed for all multiple RRS processes involved. This suggests that the broad structures on the high energy side of the sharp peaks are related to optical transitions.

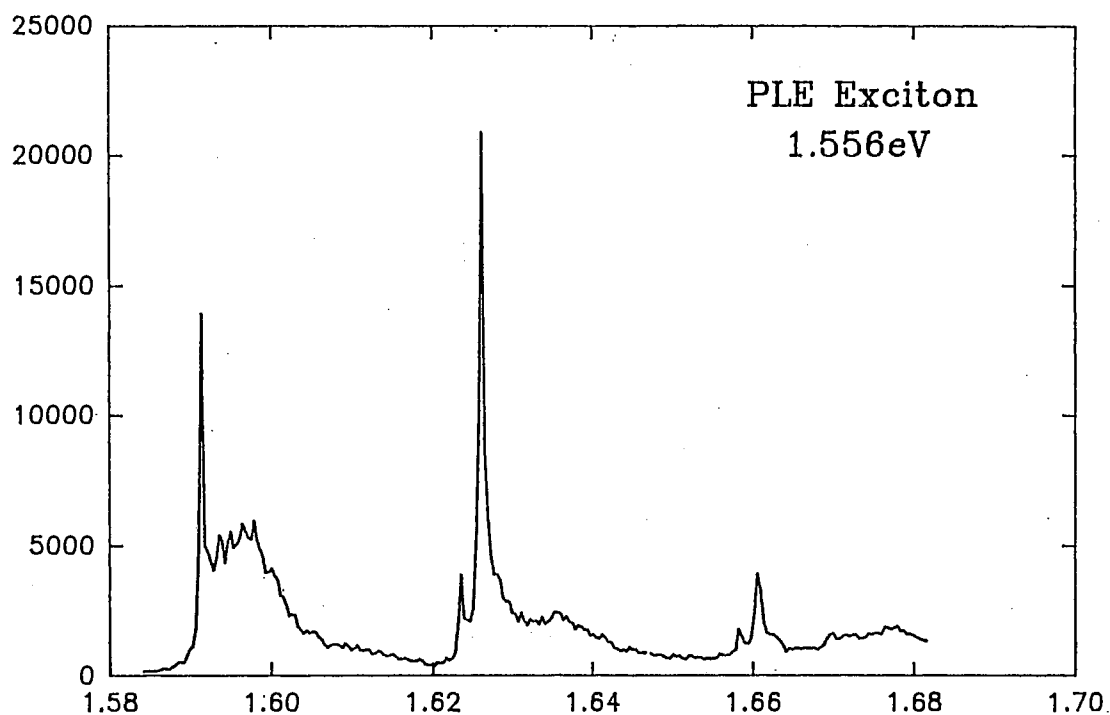


Figure 27. Phonon assisted PLE spectra obtained from 3D plots of combined PL and multiple RRS spectra versus incident photon energies (see Fig. 23 and Fig. 24). Up to third order multiple resonant phonon processes can be observed. The sharpest peaks in originate from strong resonances with excitonic states, whereas the broad structures in this figure are related to PL enhancement due to phonon assisted resonances with the subband states much like traditional PLE.



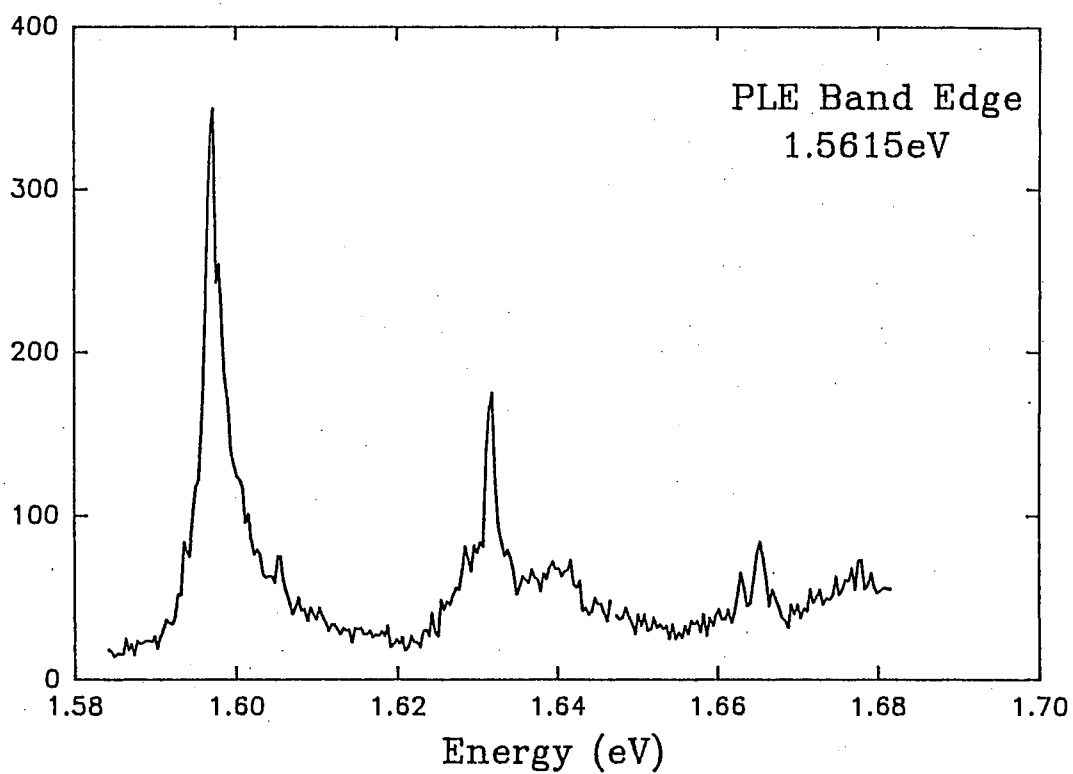


Figure 28. Phonon assisted PLE as in figure 27 monitored from 1.556 eV. This is suggested to be the 1hh subband continuum resulting from Fano-type resonances.

In order to aid in the determination of the origins of the multiple RR processes it is useful to examine the calculated subband structure in this SL. This is shown in figure 29 for the first three quantized level determined from tight-binding calculations. The following approximation representing the subband continuum states. Considering the first order process, the structure in figure 27 for this range can be explained by the following diagrams shown in figure 30. The curved lines represent the 1e and 1hh subband continuum states, whereas the small discrete lines below the subband symbolizes excitons which appear in optical spectra at the critical points. In (a) the case is shown when a double resonance occurs with the exciton states at the  $M_0$  and  $M_1$  critical points. This occurs when the incident photon energies are resonant (incoming) with the 1HH  $M_1$  saddle-point exciton transition energy, in addition to scattered photons (outgoing) resonant with the 1HH  $M_0$  exciton. Since the separation between the 1HH  $M_1$  and  $M_0$  excitons is determined by combined 1e-1hh subband dispersions as well as exciton binding energies at the respective critical points, it can be expected that they are separated by a phonon energy. In this case the first order double resonant Raman scattering involving the exciton states (sharp peak in figure 27) can be explained as follows. An incident photon is resonant (incoming) with the 1HH  $M_1$  saddle point exciton transition energy. The excited exciton is then scattered by an optical phonon to the  $M_0$  critical point such that the scattered photon is resonant (outgoing) with the 1HH exciton transition energy at the  $M_0$  critical point.

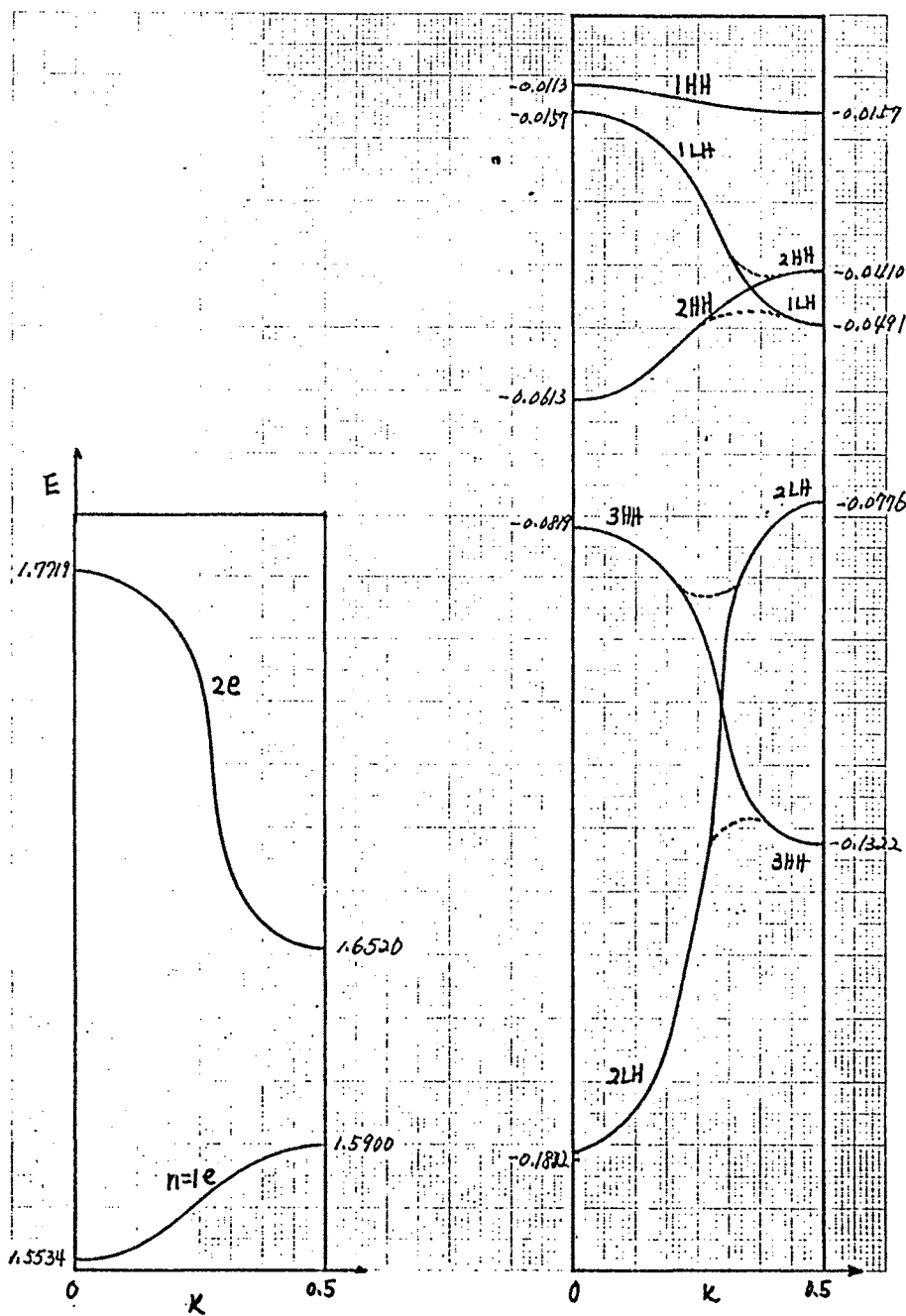


Figure 29. Calculated subband structure in a GaAs/Al<sub>0.14</sub>Ga<sub>0.86</sub>As SL with  $L_z = 59 \text{ \AA}$  and  $L_b = 31 \text{ \AA}$ . These were determined from a tight binding calculation assuming a 70/30 band offset ratio.

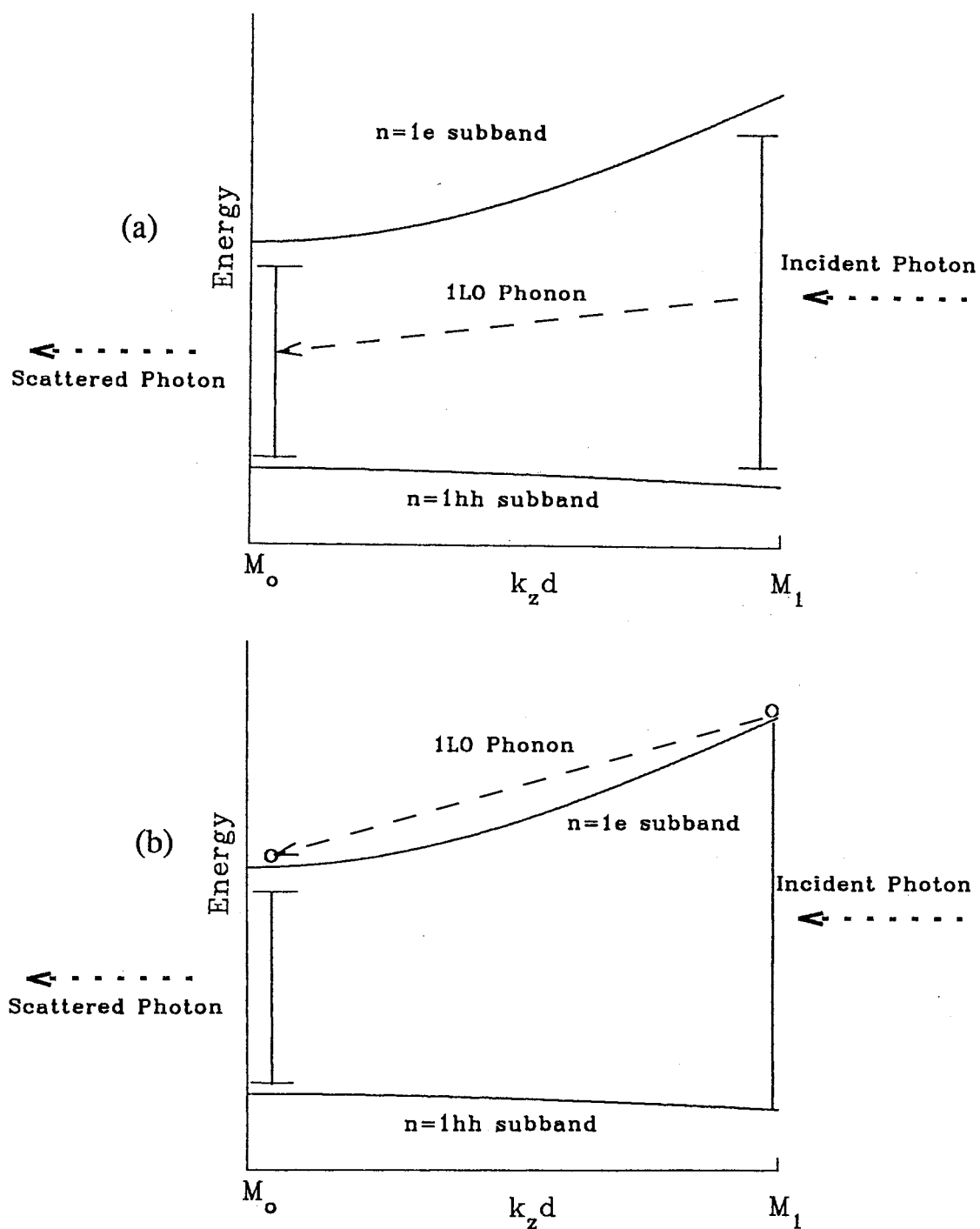


Figure 30. Schematic diagrams describing the origins of the first order double RR process. In (a) the process resulting in the sharp excitonic peak is given, and in (b) the origins of the higher energy broad structure is explained.

Figure 30(b) illustrates a slightly different situation in which the incident photons produce an incoming resonance with the  $1e-1hh$  subband transition energy at the  $M_1$ -type critical point. The corresponding scattered light in this instance is experimentally observed to appear energetically near the peak of the broad structure as seen in figure 23. Since the  $1e$  subband dispersion is roughly equal to some LO phonon energy of the superlattice, the photoexcited electron at the (BZE)  $M_1$ -type critical point is scattered by an LO phonon to the (BZC)  $M_0$ -type critical point. The effect of this resonant scattering of electrons produces an efficient relaxation channel and thus enhances the  $1HH$  exciton PL in much the same way as the  $1hh$  subband continuum does in producing the peak H in traditional PLE. The maximum of this broad peak in figure 27 determines the incident photon energy which gives the largest enhancement to the  $1HH$  exciton PL. This occurs when the electron is scattered to the  $1hh$  BZ-center. Therefore, the difference between the sharp exciton related peak and the broad structure can be used as a good estimate of the  $1HH$  exciton binding energy. This value is approximately 5.5 meV which is consistent with the separations between the corresponding structures observed in the spectra of PL and RRP measurements (see figures 22(a) and 25). This also supports identifying the higher energy structure in the PL as due to  $1hh$ -like subband states. According to the PLE spectra in figure 22(b), the separation between peaks  $1HH$  and H suggest binding energies approximately equal to 4.5 meV.

The phonon energy observed experimentally in the first order processes is approximately 35.2 meV, which is less than the 36.6 meV bulk GaAs LO phonon.

The scattering strengths of electrons or excitons with superlattice phonons depends on parity of the particle and phonon wavefunctions as well as the overlap between them. In this sample, the phonons, electron and excitons have extended wavefunctions. Therefore, several phonon modes originating from the GaAs layers or from the  $\text{Al}_{0.14}\text{Ga}_{0.86}\text{As}$  can be available for scattering. The GaAs-like barrier phonons are less dispersive as well as lower in energy than the GaAs well phonons and may give rise to the 35.2 meV phonon mode. The appearance of the 35.2 meV phonon indicates the energy separations dictating the strong resonances. Thus it may be inferred that the 1e subband dispersion is approximately 35.2 meV.

The only electron (exciton) - phonon interaction that explains this process is the intraband Fröhlich (F) process. Linear polarization measurements show the intensity of the polarized spectra is approximately three times that of depolarized spectra. It is a well known fact that the intraband F-process can appear in the forbidden depolarized spectra under resonant conditions. It has been shown theoretically that first order interband F-process under double resonant conditions can also lead to exciton scattering between the 1HH and 1LH excitons. This interband F-process is not allowed in singly resonant or second order processes. Using circular polarization techniques, the intraband F-process is allowed in (+ +) or (- -) polarized spectra whereas the interband F-process appears in (+ -) depolarized spectra due to the difference in the light-hole and heavy-hole angular momenta.

The second order process involves the same ideas but involves scattering by two phonons, which introduces additional steps. The band structure diagram in figure

30 shows that strong incoming resonances related to 1e-1lh subband and the 1LH exciton and will occur near 1.64 eV. Since resonances are most significant and critical-points. This suggests various interband and intraband scattering processes by the SL optical phonons can also give rise to multiple resonances. Consider only the two sharp exciton related peaks in this region shown in figure 27. One possibility is scattering of the 1LH exciton to the 1HH exciton at  $M_1$  by the deformation potential (DP) or interband F-process, then scattering to  $M_0$  by the intraband F-process. This process can involve symmetry allowed LO and forbidden TO phonon scattering under resonant conditions for the DP-process, and only LO phonon scattering for the intraband F-process. This means that the sharp peaks should be Stokes shifted by SL phonon energies given by LO + TO and 2LO. These two peaks are observed to be separated by  $\sim 2.4$  meV which is in good agreement with the LO-TO splitting of  $\sim 2.8$  meV in bulk GaAs. The two peaks are Stokes shifted by 67.2 and 69.6 meV respectively. As discussed previously, the superlattice phonon modes available for the scattering process are those which match strong resonant conditions, therefore the Stokes shifted frequencies do not need to match those in nonresonant conditions, or those used in the different order processes. Another possible process is the scattering from the 1LH saddle-point exciton to the zone center 1LH exciton. This process would involve simultaneous scattering of two LO phonons by the intraband F-process, since no exciton spin state changes occur in this scattering. This process however, is nonresonant with the 1HH exciton at  $M_0$ . Although it can be an efficient channel to this 1HH exciton caused by phonon assisted transitions. In published literature,

circular and linear polarization techniques describe how the relative contributions of some of these scattering processes can be obtained [69-71]. In some instances, interference between electron and hole scattering mechanisms can occur in higher order processes. This only occurs for those processes involving the same phonon parity. For instance, the 1LO F-process together with the 1LO (TO) DP-process would not be expected to interfere because they involve phonons of different parity.

The broad structure arising from phonon assisted transitions to the efficient PL relaxation channels are more involved than that for the first order process as can be seen in figures 27 and 28. In this case strong subband mixing effects between the 2HH and 1LH subbands occur near the Brillouin zone edge. These mixing effects which are seen in PLE spectra do not appear in the RRP. This is evident in the LO phonon RRP (figure 31) taken with incident photon energies in the vicinity of the second order processes. The separation between the observed structure is  $\sim 5.5$  meV and can be identified with that appearing in the first order RRP as well as PL spectra. That is it shows outgoing resonances with the 1HH exciton and the 1LH-H Fano-type resonance. The difference in intensities between these peaks is only a factor of 300, which is still more than an order of magnitude larger than that observed for singly outgoing resonances between 1LH and 1HH zone-center excitons. This could reflect the faster loss in coherence between the photoexcited e-1lh pair as compared to that in the first order processes.



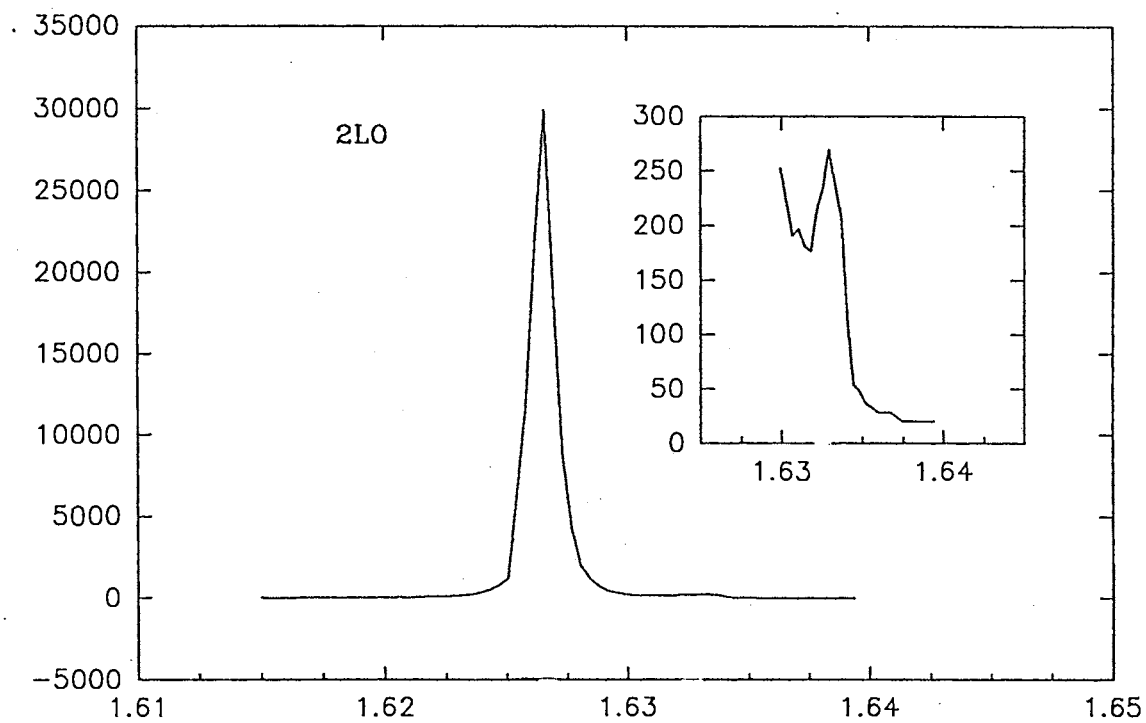


Figure 31. Triply resonant Raman profile in the vicinity of the second order scattering processes. It involves two noninterfering LO phonon scattering via the F- and D-processes. This process described in the text should be dominant.

The third order processes are much weaker and could be due to the fact that only singly resonant processes. Since the intensity reflects the number of resonant energy denominators. One interesting feature is the high energy shoulder on the stronger sharp peak. This may be related by effects as the exciton continuum states described by a recent RRS theory [56].

It has been discussed that the linewidths of the exciton related structures in figure 27 depend on the the LO phonon lifetime ( $\sim 3$  psec) as well as the exciton dephasing time [69-71]. Using this idea, the exciton dephasing times for scattering from  $M_1$  to  $M_0$  in our sample is seen to be longer than a few picoseconds.

CHAPTER IV

PICOSECOND RAMAN STUDY OF HOT  
PHONONS IN  $\text{Al}_x\text{Ga}_{1-x}\text{As}$  ALLOYS

Introduction

The ability to vary the energy band gap of  $\text{Al}_x\text{Ga}_{1-x}\text{As}$  alloys from about 1.4 eV to 2.0 eV, at room temperature, makes this ternary III-V compound an attractive candidate for electro-optical devices. However, because of the substitutional disorder associated with alloying, an effect referred to as alloy potential fluctuations (APF) may hinder the performance of such devices. The effects of APF on transport properties of  $\text{Al}_x\text{Ga}_{1-x}\text{As}$  alloys is believed to be a significant factor leading to reduced mobilities in these compounds [83-85]. In addition, it is believed that the asymmetric lineshapes of cw Raman experiments on these alloys are the result of APF. The study of this asymmetry has led to a debated discussion of whether the phonons in these alloys are localized on a scale of a few hundred angstroms. Thus study of localized phonon modes and their influence on carrier dynamics is an important issue which has received much attention, especially in GaAs/AlAs superlattices where it is well known that the LO phonons are localized.

Disorder induced by the APF can destroy the translational symmetry of a pure crystal, so that wavevector conservation is no longer valid. In Raman backscattering

experiments from crystals with translational symmetry, the Raman active modes have a phonon wavevector,  $\mathbf{q}$  very near the Brillouin zone center leading to a  $\mathbf{q} = 0$  Raman selection rule. It was first suggested that the asymmetric lineshapes observed in cw backscattering Raman experiments of LO phonons are caused by a relaxation in the  $\mathbf{q} = 0$  Raman selection rule induced by the APF [86]. If this relaxation leads to a large uncertainty in  $\mathbf{q}$ , localization of the Raman active phonon modes are expected. The asymmetry which appears on the lower energy side of the Stokes line, was interpreted as the non-zero  $\mathbf{q}$  modes becoming Raman active by relaxation of the  $\mathbf{q} = 0$  selection rule [86]. The uncertainty in  $\mathbf{q}$  could then be determined by the measured Raman linewidth. Based on a spatial correlation model, it was determined that the LO phonon wavefunctions are localized on a scale from about 40 to 150 Å depending on the aluminum concentration [86]. It was later shown from a time resolved Raman experiment that the wavevector conservation still holds in  $\text{Al}_x\text{Ga}_{1-x}\text{As}$  alloys and that localization does not occur on the 100 Å scale [87]. From a comparison of forward and backscattering measurements, conclusive evidence was given in support of wavevector conservation in  $\text{Al}_x\text{Ga}_{1-x}\text{As}$  alloys. However, this work only considered aluminum concentrations up to  $x=0.11$ . The authors of this work suggest that the asymmetry results from higher  $\mathbf{q}$  modes becoming Raman active by the APF and not by wavevector uncertainty leading to localization [87].

Experimental and theoretical studies have shown that the phonon dispersion curves in  $\text{Al}_x\text{Ga}_{1-x}\text{As}$  alloys are well defined [88,89]. The effect of alloying on the LO branch is generally to reduce the zone-center frequency and flatten out the dispersion

[89]. By treating the alloy as a disordered system, the dispersions have been calculated using the coherent potential approximation (CPA) discussed in chapter II. The results of this treatment demonstrated that a well defined downward dispersion can exist in the disordered alloy but that a finite energy width is associated with the curve [88]. The width associated with this dispersion fit well to the asymmetric lineshapes observed in cw Raman experiments [88]. Although, there currently exists some debate concerning LO phonon dispersions in  $\text{Al}_x\text{Ga}_{1-x}\text{As}$  alloys [90].

Picosecond Raman scattering is powerful method for studying LO phonon localization as well as hot electron dynamics. It has been shown by this technique that LO phonon lifetimes and total electron-phonon scattering rates of  $\text{Al}_x\text{Ga}_{1-x}\text{As}$  alloys ranging up to  $x=0.24$  are comparable to that in GaAs [91]. These results are in support of phonon wavevector conservation and thus no localization. This work also demonstrated that hot electron dynamics in  $\text{Al}_x\text{Ga}_{1-x}\text{As}$  alloys are similar to that in bulk GaAs and these alloys can therefore be advantageous in device applications using ballistic transport. In addition, this suggests that hot electron dynamics are not sensitive to alloying as is the case for normal transport properties [91].

In this chapter experimental work designed to study the possibilities of LO phonon localization covering the range of aluminum concentrations for direct band gap  $\text{Al}_x\text{Ga}_{1-x}\text{As}$  alloys is presented. Using the picosecond Raman scattering technique we can determine the generation rate of a nonequilibrium distribution of LO phonons. This rate is sensitive to the spatial extent of the LO phonons, and can therefore be used as a method to investigate localization [92,93]. Our results suggests that no

localization exists in these alloys. In addition, we have formed a complete picture of hot electron dynamics in GaAs and  $\text{Al}_x\text{Ga}_{1-x}\text{As}$  alloys for hot carriers generated by photoexcitation of  $> 2$  eV photons.

## Experiment and Results

### Introduction

Nonequilibrium carrier distributions in semiconductors can be created by picosecond optical pulses having sufficient photon energies. The energy difference between an excited state and the band minimum defines the carrier excess energy. This is demonstrated in figure 32, for an electron photoexcited into the  $\Gamma$  valley conduction band from the valence band. The carrier distribution has a temperature which is initially much larger than the lattice temperature, and is referred to as a hot carrier distribution. The average excess energy and temperature of the hot carrier distribution are related by;

$$E = \frac{3}{2}KT \quad (36)$$

where  $K$  is Boltzmann's constant. Since holes have larger effective masses, the majority of excess energy is given to the electrons in the conduction band. In polar semiconductors this hot electron distribution can lose energy or cool, by relaxing to lower  $k$  states via electron-electron or various electron-phonon interactions. Electrons can scatter to lower  $k$  states within the  $\Gamma$  valley by electron-electron scattering.

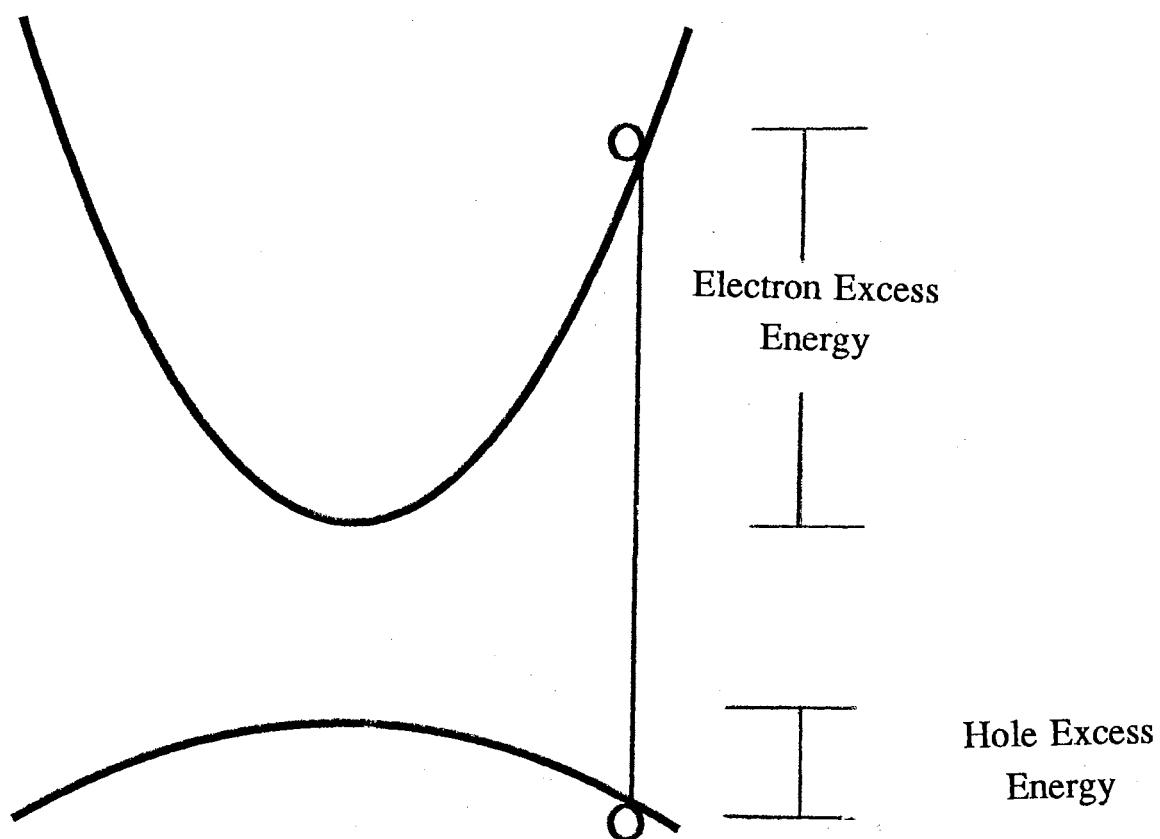


Figure 32. Schematic representation of the excess energy of photoexcited carriers in the  $\Gamma$ -valley of GaAs or  $\text{Al}_x\text{Ga}_{1-x}\text{As}$  alloys. Assuming parabolic bands, the total excess energy is divided between electrons and holes determined by the ratio of their effective masses at the zone center.

Electrons may also be efficiently removed from the  $\Gamma$  valley into the L or X satellite valleys by means of the deformation potential electron-phonon interaction. This intervalley scattering involves zone edge LO and LA phonons for  $\Gamma \rightarrow$  L transitions and only zone edge LO phonons for  $\Gamma \rightarrow$  X transitions [94]. The third dominant relaxation mechanism is the intravalley Fröhlich scattering caused by the interaction of an electron and the macroscopic electric field associated with a LO phonon. Since the excess energy of an electron is less and has a larger effective mass while in the L or X satellite valleys, the Fröhlich interaction is dominant in the  $\Gamma$  valley. From here on out the Fröhlich scattering will refer to intra- $\Gamma$ -valley relaxation of an electron.

There are two models used to describe the distribution of hot electrons during the relaxation process. The simplest model is referred to as the cascade model and assumes that the electron distribution remains monoenergetic throughout the intra- $\Gamma$ -valley relaxation. The second model is referred to as the instantaneous thermalization model. This model assumes that the electron distribution instantly thermalizes to a Fermi-Dirac distribution by electron-electron scattering. This distribution is in quasi-equilibrium and is still "hot" since its average energy is the initial excess energy and is related to the temperature of the distribution by equation (36). The difference in choosing between these two models depends upon the density of photoexcited carriers. It was thought by some that the cascade model was valid for densities of  $10^{17} \text{ cm}^{-3}$ , but recent work including ours suggests that the instantaneous thermalization model should be applied for carrier densities as low as  $10^{17} \text{ cm}^{-3}$ .

As the hot electron distribution relaxes via the Fröhlich interaction, a



nonequilibrium population of phonons are emitted. This population of phonons has a temperature which is also much larger than the lattice temperature and are called hot phonons. The hot phonon occupation number  $N_q$  is dependent upon the phonon wavevector  $q$  defined by the relaxation process. In figure 33, this distribution is shown for all relevant values of  $q$  [95]. Because of the conduction band structure, no nonequilibrium phonons can be generated in GaAs having  $q < 4.5 \times 10^5 \text{ cm}^{-1}$ . This distribution has a sharp peak since the matrix elements of the Fröhlich interaction are proportional to  $q^{-3}$  [95].

The initial relaxation of hot carriers in polar semiconductors is determined by the interplay between the various scattering processes discussed. Carrier-carrier scattering is mostly determined by the carrier density whereas intervalley scattering is very sensitive to the excess energy of an electron. Therefore depending on the density and excess energy of the carriers, either carrier-carrier scattering or intervalley scattering may dominate the initial relaxation process. In the extreme case of a very low carrier density ( $< 10^{16} \text{ cm}^{-3}$ ) and low excess energy, the Fröhlich intravalley scattering may dominate the initial relaxation process.

Picosecond (ps) and femtosecond (fs) optical spectroscopies have provided much of the information about these relaxation processes [92,95-105]. Both intervalley and intravalley scattering rates in several III-V systems have been determined using picosecond and subpicosecond Raman spectroscopy. In most of the time resolved Raman experiments, the nonequilibrium population of the Raman active LO phonon mode is created by photoexcited hot carriers. Those nonequilibrium

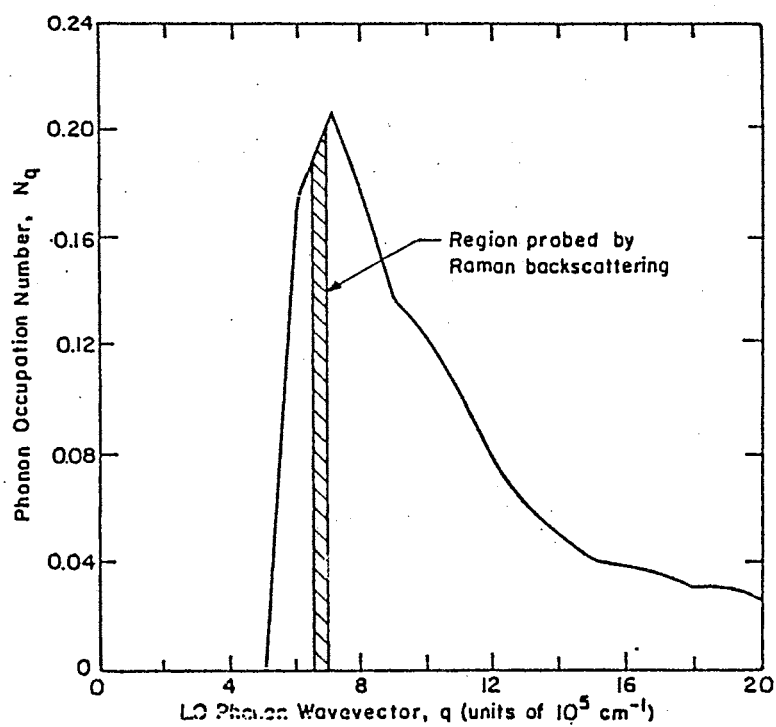


Figure 33. Plot of the LO phonon occupation number versus phonon wavenumber [95]. This plot is obtained for a time of 3 psec after photoexcitation using photon energies of 1.77 eV.

phonons are probed either as a function of time delay [96-99] or at a fixed time delay varying other parameters such as the laser photon energy or the carrier density [95,100]. Kash, Tsang and Hvam determined the Fröhlich scattering time in GaAs using a subpicosecond time-resolved Raman technique [96]. Collins and Yu have investigated the intervalley scattering rates in GaAs with picosecond Raman spectroscopy [95]. Kim and Yu have determined the intervalley scattering rates in GaAs and  $\text{In}_{1-y}\text{Ga}_y\text{As}$  using subpicosecond Raman scattering [100,101]. In some of these experiments, the simple cascade model was used to analyze the data [95,96]. In this model the effect of intervalley scattering was sometimes excluded even when the photoexcited electron energy was sufficient enough to enable the intervalley scattering [96]. In most of the analysis of the time-resolved Raman experiments, the generation of the hot LO phonons was assumed to be primarily from electrons in the  $\Gamma$  valley originating from the light- and heavy-hole bands [95,96,100]. However, in a recent femtosecond luminescence experiment in GaAs, it was suggested that the majority of the electrons in the  $\Gamma$  valley, within a few picoseconds after photoexcitation, come from the split-off band when the photon energy is  $\geq 2\text{eV}$  [102]. Most of the photoexcited electrons originating from the light- and heavy-hole bands are quickly transferred to the satellite valleys because of their large excess energy and the ultrafast intervalley scattering times. At a carrier density of  $\sim 10^{17}\text{ cm}^{-3}$  these photoexcited carriers will thermalize, by carrier-carrier scattering, to a nonequilibrium Fermi-Dirac distribution. Therefore it is possible for a small portion of electrons photoexcited from light- and heavy-hole bands to remain in the  $\Gamma$  valley because of thermalization. If we

consider thermalized hot electrons excited from the split-off band, most of these will not have enough excess energy to transfer to the satellite valley through the intervalley scattering. Therefore, a significant fraction of the hot phonons initially generated by the intra- $\Gamma$ -valley Fröhlich scattering should come from the electrons which have been photoexcited from the split-off hole band.

### Experimental Technique and Set-up

The experimental technique used in this chapter is referred to as one-beam-excite-and-probe ps Raman scattering [101]. In this technique the same excitation pulse which creates the hot electrons also probes the hot phonon occupation. The experimental Raman scattering intensities of the Stokes ( $I_s$ ) and anti-Stokes ( $I_{as}$ ) lines determine the LO phonon occupation number given by;

$$N_q = \frac{1}{\frac{I_s}{I_{as}} - 1} \quad (37)$$

provided that there is no appreciable resonant Raman scattering effects.

The picosecond optical pulses are generated by a pulse compressed Nd:YAG laser system manufactured by Spectra Physics. The portion of the system used in this experiment consists of a model 3800 cw Nd:YAG laser and a model 3695 optical pulse compressor and is shown in figure 33. The Nd:YAG laser is mode locked using an acousto-optic modulator. This provides 1064 nm optical pulses with a pulse width < 100 psec at an average power of 10 W and an 82 MHz repetition rate. The

1064 nm pulse is guided into the optical-pulse compressor. The average power after compression is 3.5 W having pulse widths less than 5 psec. Inside, the pulse compressor frequency doubling via a KTP crystal occurs at the last stage. The 532 nm pulses have an average power of 1 W and a pulse width of less than 3.5 psec. An INRAD autocorrelator is used to measure the optical pulse width. In these experiments, the pulse has a  $\text{sech}^2(x)$  pulse shape with a FWHM of 1.5 psec. The 2.33 eV pulses are used as the excitation in a Raman backscattering geometry. The wavevector of the phonon probed in this geometry is  $\sim 8.3 \times 10^{-5} \text{ cm}^{-1}$ , which is near the peak of the distribution given in figure 33. A polarization rotator constructed from two Fresnel-Rhomb prisms is used to control the polarization of the incident beam. The scattered light is collected by a two lens system having an f-number  $\approx 8$ , which matches that of a SPEX 1877 triplemate spectrometer. A Photometrics model PM512 liquid nitrogen cooled charge coupled device (CCD) detector was used to record scattered light intensities.

#### Pulse Width and Carrier Density Considerations

The hot phonon lifetimes in GaAs,  $\text{Al}_x\text{Ga}_{1-x}\text{As}$  and GaAs/ $\text{Al}_x\text{Ga}_{1-x}\text{As}$  QWs are all approximately 5 to 7 psec [96,98,108,110] and the time scales that the hot electrons emit LO phonons via the Fröhlich interaction are about 0.15 to 0.2 psec [96,111]. Therefore, the 1.5 psec duration time of the laser pulses is suitable for pumping and probing the hot phonon population.

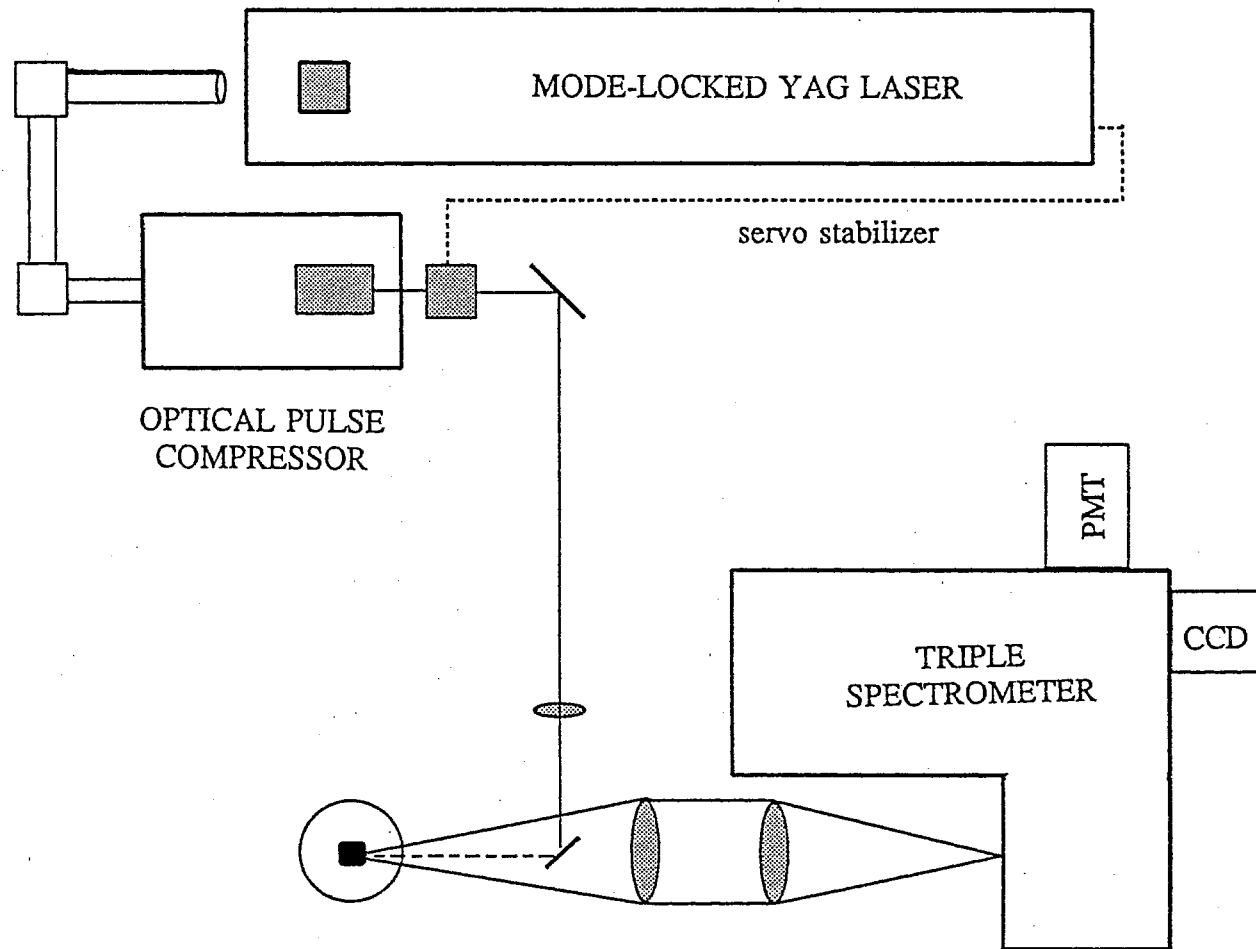


Figure 34. Diagram of Raman backscattering set-up.

In the experiments the dependence of  $N_q$  on the incident light power,  $P$  is measured. The carrier densities used are estimated to be  $\leq 10^{17} \text{ cm}^{-3}$ . Therefore the experimental  $N_q$  is linear with  $P$ , so as to increase the data redundancy and reduce the experimental errors. It has been reported that  $N_q$  is linear with electron densities up to  $2 \times 10^{17} \text{ cm}^{-3}$  and reaches its maximum value in 2-3 ps [91,95,96,100]. Considering the pulse duration and carrier densities used in the experiments, the linearity of  $N_q$  with  $P$  implies that the Raman active LO phonon occupation number has not reached its maximum so that there are no relaxation effects [96,100]. Thus  $\partial N_q / \partial P \propto \langle \partial N_q / \partial t \rangle$  is valid for a constant laser pulse width, and the experimental  $\partial N_q / \partial P$  values are defined as the phonon generation efficiency [92].

The samples studied are a series of MBE grown bulk  $\text{Al}_x\text{Ga}_{1-x}\text{As}$  alloys ranging in  $x$  from 0 to 0.39. The phonons in  $\text{Al}_x\text{Ga}_{1-x}\text{As}$  alloys are well known to display a two mode behavior. The GaAs-like and AlAs-like modes have zone center LO frequencies which become less with increasing aluminum concentration. The only other significant difference to consider among the series of samples is the excess energy due to the changing band gap. The excess energy, for electrons photoexcited from the heavy hole valence bands, in the  $\Gamma$ , X, and L valleys versus the aluminum concentration is plotted in figure 35 determined by the equations given by table III in chapter I. Since the excess energy of the satellite valleys changes slowly compared to that in the  $\Gamma$  valley, the intervalley scattering rates are expected to be nearly constant over the range of samples studied. In table VII, the series of samples are listed with several relevant parameters. The values of  $x$  are determined from photoluminescence

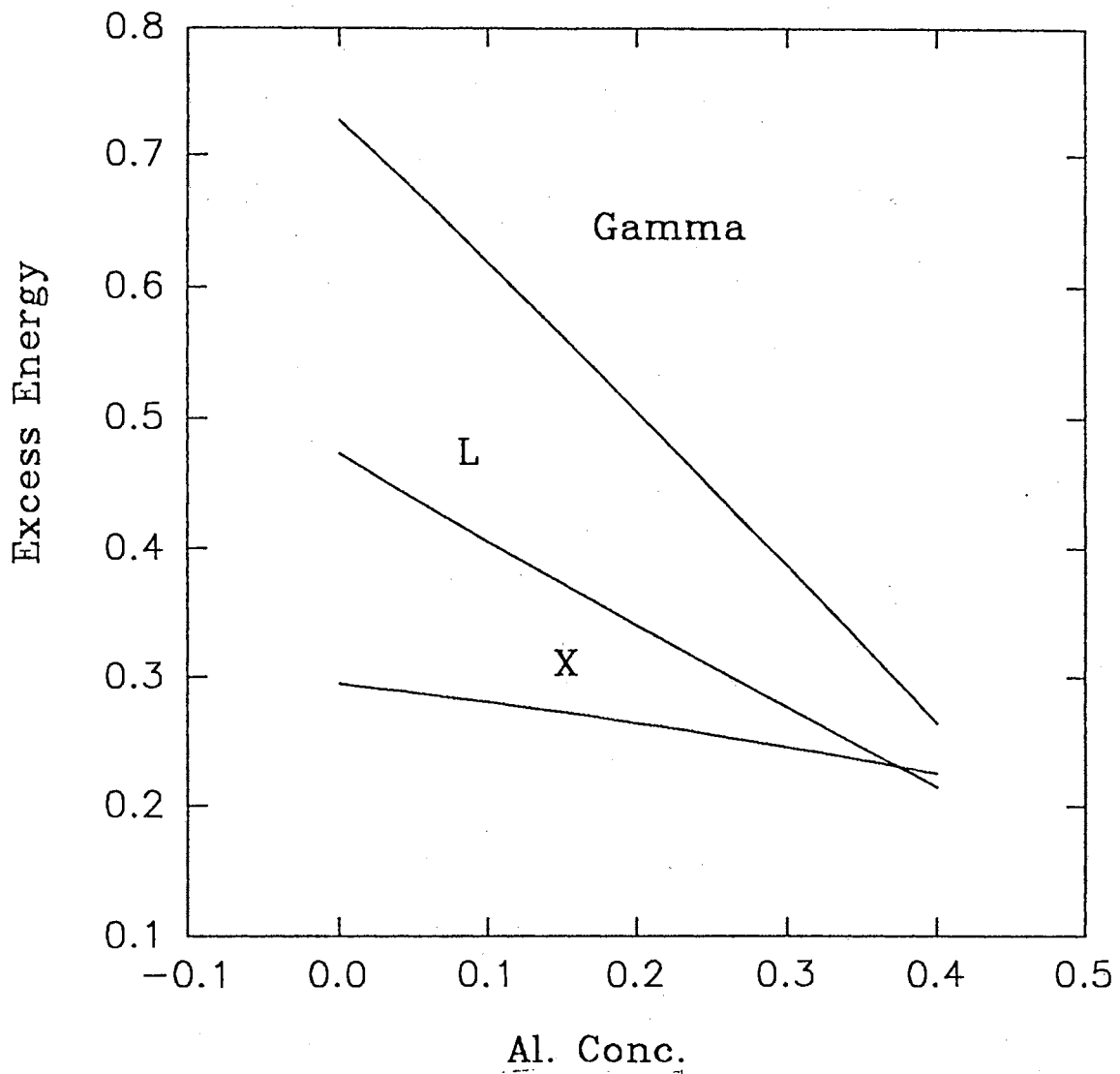


Figure 35. Excess energy of electrons in the  $\Gamma$ , X, and L valleys which are photoexcited from the heavy-hole valence band with photon energies of 2.33 eV.



TABLE VII  
PL ENERGY AND CORRESPONDING CONCENTRATIONS

Sample #	$E_{\text{PL}} + E_{\text{b}}$ (eV)	x
GaAs Ref.	1.517	0
3614	1.568	0.035
901103	1.603	0.06
901110	1.657	0.10
901117	1.738	0.16
910320	1.815	0.21
901125	1.899	0.28
910225	1.938	0.31
910230	1.959	0.32
3620	1.974	0.33
901135	2.046	0.39

measurements at 20K and using the following equation for the direct band gap given by [106];

$$E_{PL} + E_b = E_{GaAs} + 1.45x - 0.25x^2 \quad (38)$$

The exciton binding energy,  $E_b$  is approximately 4 meV in GaAs, and is assumed to be nearly the same in the alloys. In the experiments, the hot phonon generation rate was determined for GaAs and all GaAs-like modes. Several of the AlAs-like modes were studied and identical results can be obtained from either of the two modes in the alloy. Therefore, only the GaAs-like modes will be discussed. The picosecond Stokes and anti-Stokes Raman signal at a temperature of 20K is plotted in figure 36 for an  $Al_{0.17}Ga_{0.83}As$  alloy.

### Experimental Results

In figure 37, the dependence of  $N_q$  on the laser power,  $P$  is plotted for several samples in this study. At low  $P$ , the signal-to-noise ratio is smaller such that less weight is given to these points in showing the linear dependence of  $N_q$  with  $P$ . The  $\partial N_q / \partial P$ 's relative to GaAs for the different alloy samples in our series can be determined from the likes of figures 37 and are shown in figure 38 as the circles for both GaAs-like (filled) and AlAs-like (dashed) phonon modes. A rapid decrease of more than two orders of magnitude in  $\partial N_q / \partial P$  of the GaAs-like modes is observed when  $x$  is increased from 0 to 0.39. To explain these results simple calculations of  $N_q$  for a given pulse-width and photon energy can be performed. Since  $N_q$  is linear with

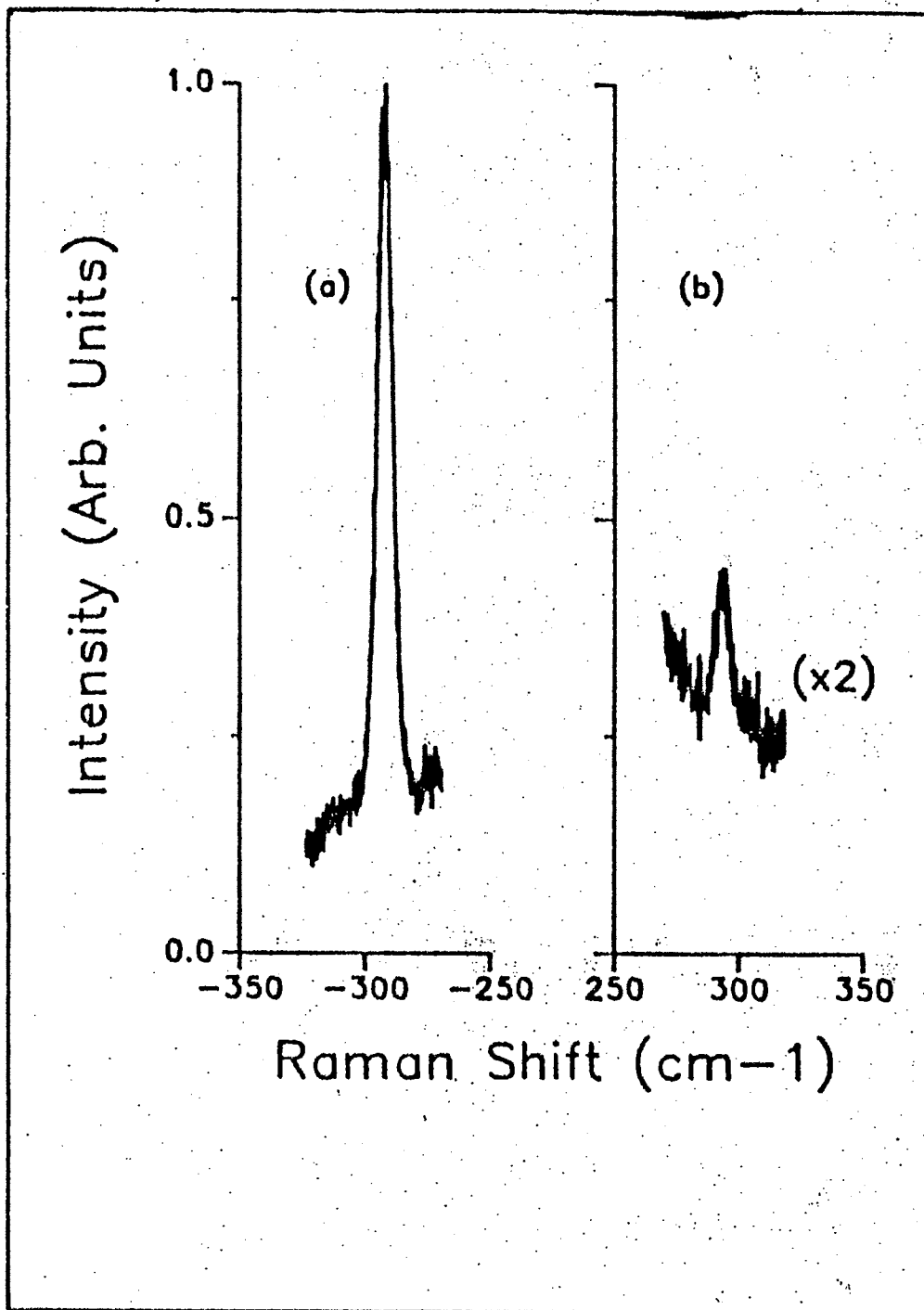


Figure 36. Picosecond Raman spectra taken from an  $\text{Al}_{0.17}\text{Ga}_{0.83}\text{As}$  alloy. The experimental hot phonon occupation number is determined through the ratio of the (a) Stokes and (b) anti-Stokes intensities.

P, the ratio of  $\partial N_q / \partial P$  between an  $\text{Al}_x\text{Ga}_{1-x}\text{As}$  alloy and GaAs is certainly equivalent to the same ratio of calculated  $N_q$ 's. Therefore experimental values of  $\partial N_q / \partial P$  can be directly compared with calculated values of  $N_q$  for a series of samples.

## Theory and Discussion

There are a couple of effects that will reduce the hot phonon generation efficiency, although the contributions from these effects are too small to explain our results. For instance, the penetration depth of a photon at 2.33 eV will be reduced by merely 40 % as  $x$  increases from 0 to 0.39 [111]. The number of GaAs-like LO phonon modes will decrease with increasing  $x$  since there exist more AlAs-like modes with larger  $x$  when the total number of modes is fixed [91]. This effect will at most reduce  $\partial N_q / \partial P$  by a factor of two between  $x=0$  and  $x=0.39$ .

To understand the cause of this rapid decrease, first consider a simple cascade model which includes intervalley scattering but excludes the electrons from the split-off hole bands. This model results in virtually identical  $\partial N_q / \partial P$  throughout our samples. This is because one can normally expect a production efficiency of  $\approx \tau_{\text{inter}} / (\tau_{\text{inter}} + \tau_{\text{intra}})$  LO phonons per electron for electrons which are excited from the light- and heavy-hole bands.  $\tau_{\text{inter}}$  and  $\tau_{\text{intra}}$  are the intervalley and intravalley scattering times respectively at the point of photoexcitation. Since the excess energy of these electrons above the L and X valley minima do not change appreciably as  $x$  varies from 0 to 0.39, (see figure 35) the intervalley scattering rates are expected to be a slowly varying function of  $x$ . Combined with the almost constant Fröhlich scattering

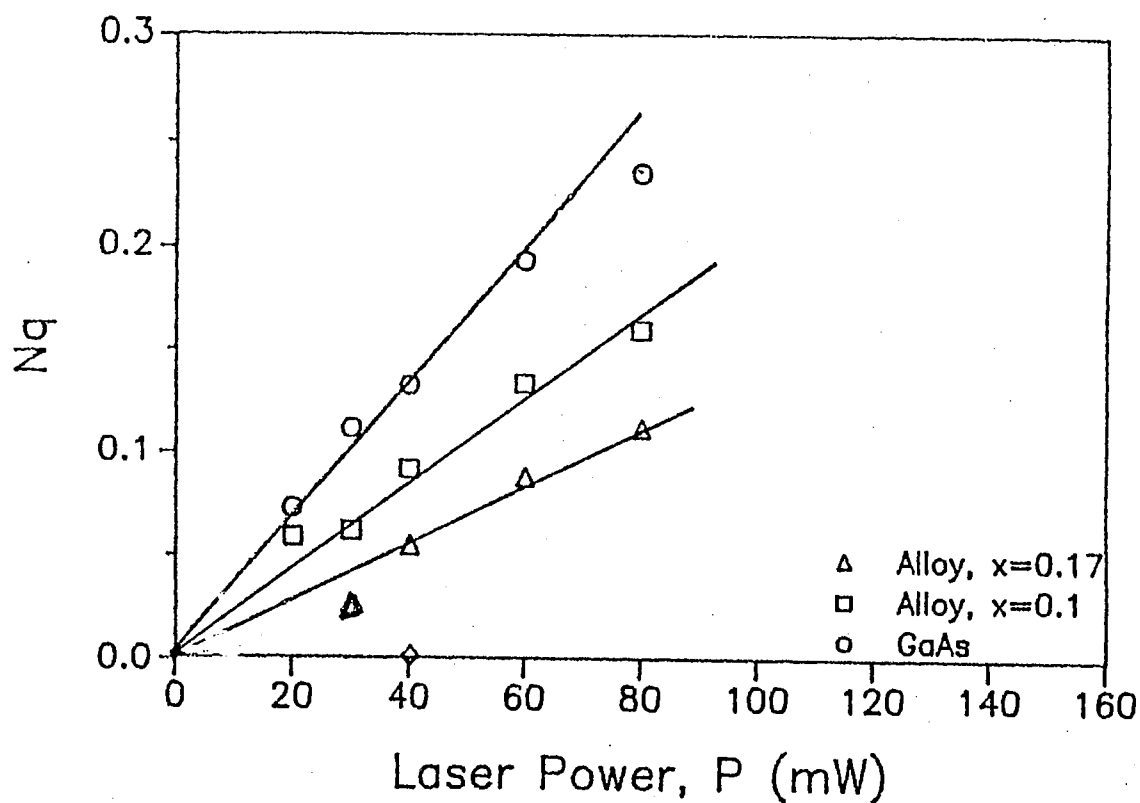


Figure 37. The experimental values of  $N_q$  versus laser power,  $P$  for several samples used in this study. The linear dependence is a consequence of the relatively low photoexcited carrier densities as well as the narrow pulse width. The data points at low power are subject to larger error because of the relatively low signal-to-noise ratio.

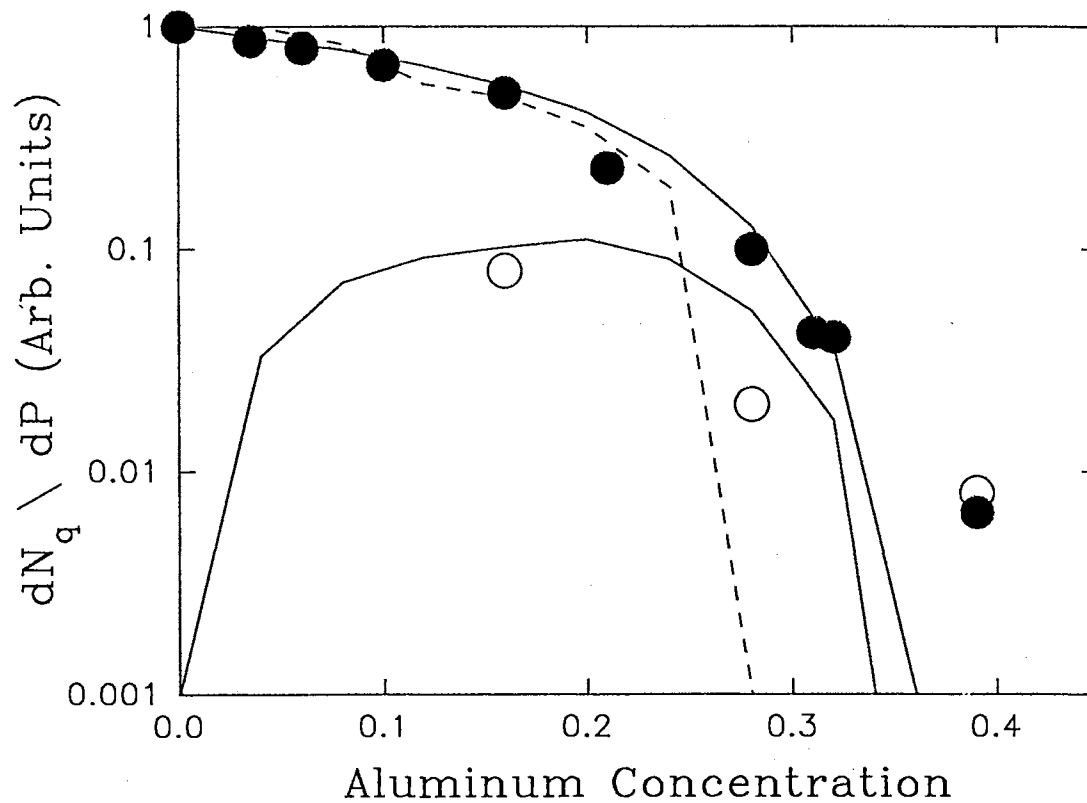


Figure 38. Relative slopes of  $N_q$  versus  $P$  taken from plots similar to that of figure 37. The filled circles represent the GaAs-like modes and the open circles are for the AlAs-like modes. The data is fit from theoretical calculations of  $N_q$  assuming only those electrons which originate from the split-off hole band. The cascade model is predicted the fit (GaAs-like) given by the dashed line, whereas the fit predicted by the instantaneous thermalization model is given by the solid line.

rate, this results in a virtually unchanging production efficiency of LO phonons as a function of  $x$ . Clearly, the two orders of magnitude decrease in the phonon generation efficiency cannot be explained with this model.

The conclusion is that the rapid decrease in the  $dN_q / dP$  is due to the decrease in the number of electrons in the  $\Gamma$  valley that do not participate in the intervalley scattering and to the reduction of excess energies with increasing  $x$ . Electrons which scatter to the L or X valleys will return to the  $\Gamma$  valley with a time constant of  $\sim 2.5$  psec at room temperature [103]. This scattering time becomes appreciably longer, at least by a factor of 2, when the lattice temperature is lowered to cryogenic temperatures [111]. This is because the zone-edge phonon populations vanish at low temperature. Therefore, within our pulse width, the sources of these  $\Gamma$  valley electrons are the electrons excited from the split-off hole band and the electrons from the light- and heavy-hole bands that remain in the  $\Gamma$  valley due to electron-electron or electron-hole scattering to lower energy points. There is no simple way to estimate the relative contribution of these two sources. However, the number the electrons excited from the split-off band is expected to be larger than that due to carrier-carrier collisions at the carrier densities we use in GaAs [112].

A production efficiency of much less than 1 LO phonon per electron is expected from the electrons which may emit a phonon before scattering into satellite valleys. This is because of the relatively fast intervalley scattering rates compared to that of the intravalley Fröhlich interaction at a photon energy  $> 2$  eV [100,102-104]. On the other hand, the electrons photoexcited from the split-off hole band can emit as

many as 8 LO phonons inside the  $\Gamma$  valley of GaAs. Actually, only about 5 of these LO phonons can be Raman active since the  $q$  of the phonons is much larger when emitted by the cooling of electrons near the  $\Gamma$  valley minimum. Therefore, most of the reduction in the  $\partial N_q / \partial P$  between GaAs and  $\text{Al}_{0.39}\text{Ga}_{0.61}\text{As}$  can be accounted for from simply considering the electrons which are photoexcited from the split-off hole band. This can be easily visualized from the schematic diagrams in figures 39 and 40. Figure 39 depicts the situation when GaAs is photoexcited by 2.33 eV photons, whereas figure 40 is the same situation for the alloy with  $x=0.39$ . In both cases, electrons with sufficient energy to undergo the intervalley scattering emit at most one LO phonon. On the average, they emit much less than one LO phonon per electron. The electrons from the split-off hole band can emit many LO phonons as described in figure 40, since they do not have enough energy to participate in the intervalley scattering process. The experimentally observed rapid decrease in the phonon generation efficiency of more than a factor of 10 between  $x=0.28$  and  $x=0.39$  may also be explained once we realize that the split-off hole band is the main source of the electrons that generate Raman active hot phonons. Assuming parabolic bands, the minimum energy required to emit a Raman active LO phonon is given by

$$E_{\text{min}} = \frac{(E_q + E_{\text{LO}})^2}{4 E_q} \quad (39)$$

$$E_q = \frac{\hbar^2 q^2}{2 m^*}$$

where  $q$  is the phonon wavevector and  $E_{\text{LO}} = 36.6$  meV [85]. At  $x=0.28$ , the excess energy of photoexcited electrons is approximately 110 meV, which is near the



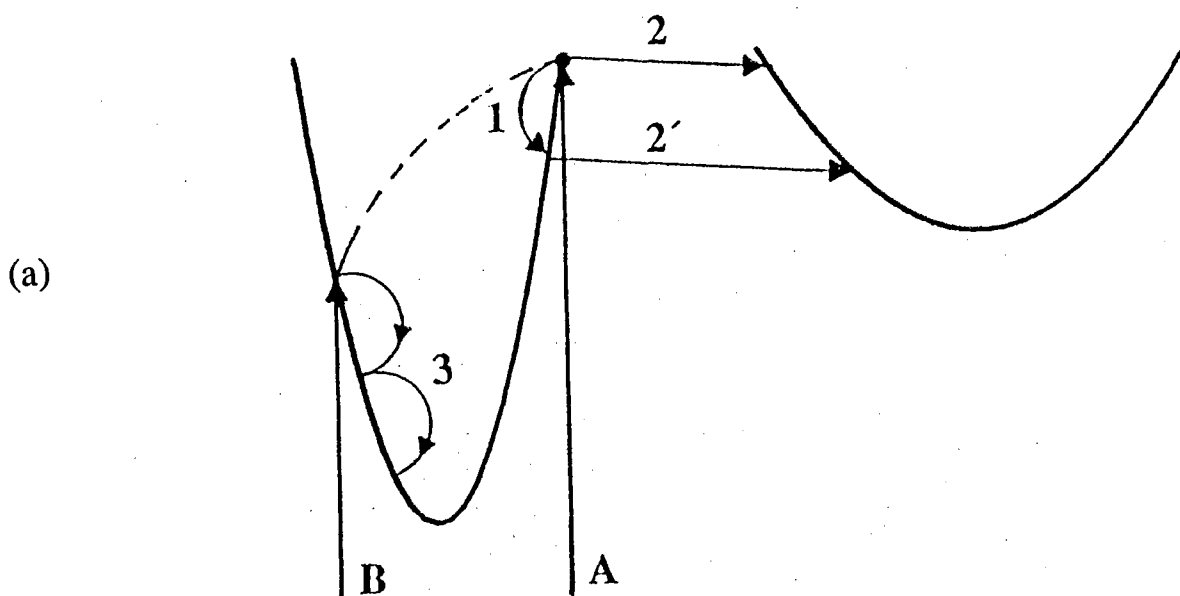


Figure 39. Schematic diagram representing the hot phonon generation by electrons from various hole bands in GaAs. Arrow A denoted the photoexcitation from the light- and heavy-hole bands, whereas arrow B denotes photoexcitation from the split-off hole band. Arrow 1 represents hot phonon generation by electrons from the light- and heavy-hole bands. Arrows 2 and 2' represent the intervalley scattering of these electrons, whereas the broken arrow depicts the scattering of these electrons by carrier-carrier collisions to the lower energy  $\Gamma$  points. The hot phonon generation by the electrons from the split-off hole band is represented by arrow 3. Since the electrons from the split-off hole band do not participate in the intervalley scattering because of lower excess energy, they remain in the  $\Gamma$  valley to generate most of the Raman active hot LO phonons.

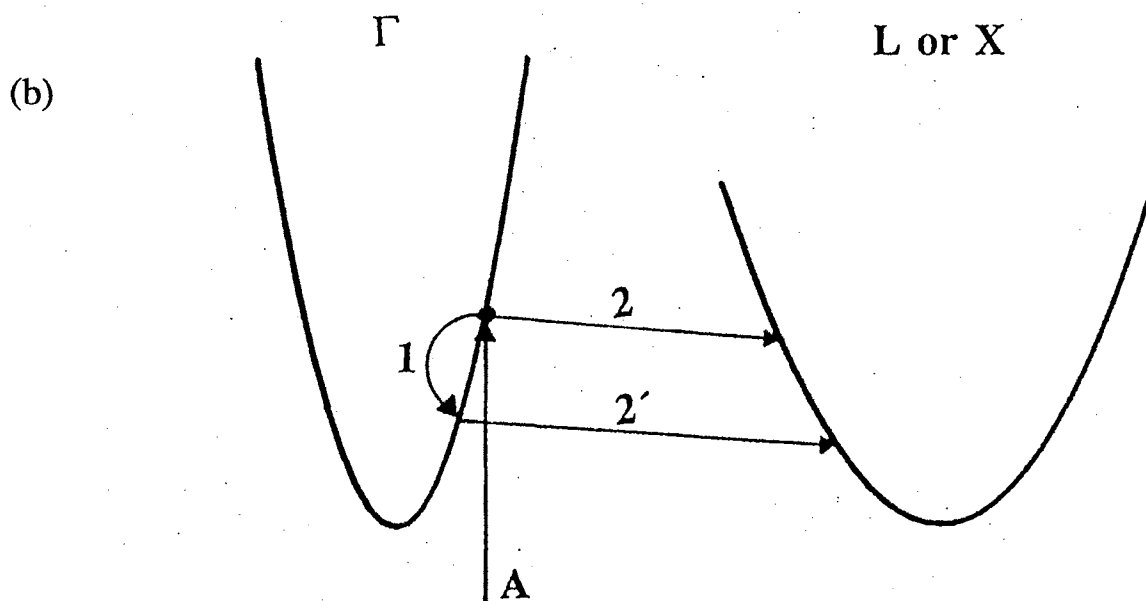


Figure 40. Schematic diagram representing hot phonon generation in  $\text{Al}_{0.39}\text{Ga}_{0.61}\text{As}$  where the minima of the  $\Gamma$ , L, and X valleys are almost degenerate. Because of the larger band gap (2.02 eV), no electrons from the split-off hole band are excited into the  $\Gamma$  valley. All photoexcited electrons can undergo intervalley scattering. As a result the total hot phonon occupation number observed at this alloy concentration is about 2% of the bulk GaAs value. The arrows in this figure have the same meaning as in figure 39.

minimum energy required to generate the Raman active hot LO phonons. Thus, below  $x=0.28$  only those electrons that have larger energy than 110 meV as a result of thermalization can generate Raman active hot phonons. The cascade model using only electrons from the split-off hole band is not in good agreement with our experimental results. The calculated  $N_q$ 's from this model decrease faster with increasing  $x$ . Since the cascade model assumes a mono-energetic distribution of electrons,  $N_q$  will rapidly decrease with lower excess energy. A relative comparison of  $N_q$  calculated by the cascade model can easily be computed from only the excess energy and relative fraction of GaAs-like modes. The calculated  $N_q$  as a function of  $x$  using the cascade model is shown as the dashed line in figure 38. On the other hand, instantaneous thermalization gives rise to a spread in the hot electron distribution which causes  $N_q$  to be less sensitive of changing excess energies. This is especially so when the average energy of the hot electron distributions are near 110 meV.

To test the validity of this conclusions, a fit between the experimental data and a simple analytical model that assumes an instantaneous thermalization of electrons from the split-off band is performed. This assumption is valid since electrons in the  $\Gamma$  valley thermalize on a time scale of 100 fs, which is shorter than our pulse width [99]. Since we conclude that almost all of the photoexcited electrons originating from the light- and heavy-hole bands rapidly transfer to the satellite valleys before emitting any LO phonons, since only the split-off hole band is considered in the calculation of  $N_q$ . From the joint density of states in GaAs at photon energies of 2.33 eV, it can be determined that approximately 23% of the total photoexcited electron density

$(\sim 10^{17} \text{cm}^{-3})$  comes from the split-off hole band. Because of this relatively small electron concentration a Boltzman distribution of hot electrons given by;

$$f(E) = \frac{n \exp\left[-\frac{E}{KT}\right]}{\int_0^{\infty} \rho(E) \exp\left[-\frac{E}{KT}\right] dE} \quad (40)$$

$$= \exp\left[\frac{\mu - E}{KT}\right]$$

can be assumed. The chemical potential is  $\mu$  and  $\rho(E)$  is the conduction band density of states. The time evolution, governed by the Fröhlich interaction, of a hot electron distribution and the corresponding hot phonon occupation is described by Boltzmanns equations [95].

The Boltzmann equation for an electron at time  $t$  is given by;

$$\begin{aligned}
\frac{\partial f(\vec{k}, t)}{\partial t} = & \frac{2\pi}{\hbar} \sum_{\vec{q}} |\langle \vec{k}, N_{\vec{q}} + 1 | H_F | \vec{k} + \vec{q}, N_{\vec{q}} \rangle|^2 \delta(E_{\vec{k}} - E_{\vec{k} + \vec{q}} + \hbar\omega_{LO}) \\
& \times f(\vec{k} + \vec{q}, t) [1 - f(\vec{k}, t)] \\
& + |\langle \vec{k}, N_{\vec{q}} - 1 | H_F | \vec{k} - \vec{q}, N_{\vec{q}} \rangle|^2 \delta(E_{\vec{k}} - E_{\vec{k} - \vec{q}} - \hbar\omega_{LO}) \\
& \times f(\vec{k} - \vec{q}, t) [1 - f(\vec{k}, t)] \\
& - |\langle \vec{k} - \vec{q}, N_{\vec{q}} - 1 | H_F | \vec{k}, N_{\vec{q}} \rangle|^2 \delta(E_{\vec{k} - \vec{q}} - E_{\vec{k}} + \hbar\omega_{LO}) \\
& \times f(\vec{k}, t) [1 - f(\vec{k} - \vec{q}, t)] \\
& - |\langle \vec{k} - \vec{q}, N_{\vec{q}} + 1 | H_F | \vec{k}, N_{\vec{q}} \rangle|^2 \delta(E_{\vec{k} + \vec{q}} - E_{\vec{k}} - \hbar\omega_{LO}) \\
& \times f(\vec{k}, t) [1 - f(\vec{k} + \vec{q}, t)]
\end{aligned} \tag{41}$$

where  $H_F$  is the Fröhlich Hamiltonian and  $E_{\vec{k}}$  is the energy of an electron in state  $\vec{k}$ .

The four terms in equation (41) correspond to:

- first term  $\rightarrow$  phonon emission by electrons in state  $\vec{k} + \vec{q}$ ,
- second term  $\rightarrow$  phonon absorption by electrons in state  $\vec{k} - \vec{q}$ ,
- third term  $\rightarrow$  phonon emission by electrons in state  $\vec{k}$ ,
- fourth term  $\rightarrow$  phonon absorption by electrons in state  $\vec{k}$ .

The Boltzmann equation for the electrons is coupled to an equation for the phonon occupation number given by;

$$\begin{aligned}
 \frac{\partial N_{\vec{q}}}{\partial t} = & \frac{2\pi}{\hbar} \sum_{\vec{k}} [ |\langle \vec{k} - \vec{q}, N_{\vec{q}} + 1 | H_F | \vec{k}, N_{\vec{q}} \rangle|^2 \delta(E_{\vec{k} - \vec{q}} - E_{\vec{k}} + \hbar\omega_{LO}) \\
 & \times f(\vec{k}, t) [1 - f(\vec{k} - \vec{q}, t)] \\
 & - |\langle \vec{k} + \vec{q}, N_{\vec{q}} - 1 | H_F | \vec{k}, N_{\vec{q}} \rangle|^2 \delta(E_{\vec{k} + \vec{q}} - E_{\vec{k}} - \hbar\omega_{LO}) \\
 & \times f(\vec{k}, t) [1 - f(\vec{k} + \vec{q}, t)] ] \\
 & - \frac{N_{\vec{q}}}{\tau_{\vec{q}}}
 \end{aligned} \tag{42}$$

The three terms in equation (42) refer to:

first term  $\rightarrow$  emission of LO phonons by electrons,

second term  $\rightarrow$  absorption of LO phonons by electrons,

third term  $\rightarrow$  phenomenological damping of LO phonons due to other decay processes.

Since our experimental pulsewidth ( $\sim 1.5$  psec) is less than the LO phonon lifetime (5-7 psec) the third term is excluded in the calculations. The matrix element for the Fröhlich interaction is given by [95];

$$|\langle \vec{k}, N_{\vec{q}} + 1 | H_F | \vec{k} + \vec{q}, N_{\vec{q}} \rangle|^2 = \frac{2\pi\hbar^2 e^2 \xi}{Vm^* Q^2} (N_{\vec{q}} + 1) \tag{43}$$

where the macroscopic electric field associated with the LO phonon is given by;

$$\xi = \frac{m^* e^2 \hbar \omega_{LO}}{\hbar^2} \left[ \frac{1}{\epsilon_\infty} - \frac{1}{\epsilon_0} \right] \quad (44)$$

This equation is valid only for electrons with s-like symmetry [95]. Assuming that the distribution functions are isotropic in momentum space and that the electron distribution is nondegenerate, Collins and Yu derive the following decoupled equations from equations (41) and (42) [95]. These are given by;

$$\frac{\partial N_q}{\partial t} = \frac{2 m^* e \xi}{\hbar^3 q^3} \int_{E_{\min}}^{\infty} f(E_k, t) dE_k \quad (45)$$

and

$$\begin{aligned} \frac{\partial f(E_k, t)}{\partial t} &= \frac{e \xi}{\sqrt{2 m^* E_k}} f(E_k + \hbar \omega_{LO}, t) \ln \left( \frac{\sqrt{E_k + \hbar \omega_{LO}} + \sqrt{E_k}}{\sqrt{E_k + \hbar \omega_{LO}} - \sqrt{E_k}} \right) \\ &- \frac{e \xi}{\sqrt{2 m^* E_k}} f(E_k, t) \ln \left( \frac{\sqrt{E_k} + \sqrt{E_k - \hbar \omega_{LO}}}{\sqrt{E_k} - \sqrt{E_k - \hbar \omega_{LO}}} \right) \end{aligned} \quad (46)$$

Where  $E_{\min}$  is defined in equation (35) and its  $q$  dependence comes from the nature of the Fröhlich interaction and conservation of momentum for the electron transition from  $E(\mathbf{k} + \mathbf{q}) \rightarrow E(\mathbf{k})$  [95]. The calculation shown in figure 38 for the instantaneous thermalization model, band non-parabolicity was included. The effects of band nonparabolicity complicate the forms of equation (45) and equation (46). Because of this, they will not be reproduced here but are given by equation (26) and equation (27) in reference 95. The nonparabolicity of the  $\Gamma_1$  conduction band has two effects on the theoretical calculation, one is to increase the scattering rate and the other is to change

the photon energy for which intervalley scattering begins [95]. An effect of band nonparabolicity of the valence bands is to include a term in the polar scattering rate due to electrons having an admixture of p-like symmetry [95].

Since split-off hole band electrons generate nearly all of the  $\Gamma$  valley hot phonons only the effects of emission and absorption of LO phonons on the hot electron distribution are considered. The effects of intervalley scattering of these electrons are negligible. In our calculation an optical pulse with a  $\text{sech}^2$  profile having a FWHM of 1.5ps is assumed. In the program calculation, the build-up of  $N_q$  is summed over increments of the pulse with times similar to that for electron-phonon scattering. The effects of changing effective masses and penetration depths with increasing  $x$  have been considered in a separate calculation and has small effects on the results [112]. The fit denoted as the (broken curves) in figure 38 is remarkably good considering the simplicity of the model. This fit has been obtained without having to include localization of LO phonons due to alloy potential fluctuations. Since localization tends to decrease the phonon generation efficiency our results might suggest that no significant localization of LO phonons due to alloying exist. This is consistent with the experimental work of reference 91, however, that work only considered alloy concentrations up to  $x=0.24$ .

Since the contributions to  $N_q$  from the other hole bands have been excluded, our model yields  $N_q=0$  at  $x=0.39$  for both GaAs-like and AlAs-like phonon modes. At this concentration no electrons can be excited into the conduction band from the split-off band at a photon energy of 2.33 eV. A combined  $\partial N_q/\partial P$  of 2% that of GaAs for



the GaAs-like plus AlAs-like LO phonons is observed at this concentration. Since nearly all of the photoexcited electrons are scattered into the satellite valleys, this small efficiency is interpreted as being due to the electrons that emit one LO phonon before transferring to the satellite valleys. If such effects as the changing band structure, and the penetration depth on  $x$  are considered, then only 6% of the total  $\partial N_q/\partial P$  in GaAs will be due to those electrons which emit one LO phonon before undergoing intervalley scattering. This small contribution from the light- and heavy-hole bands on  $\partial N_q/\partial P$  suggest that the intervalley scattering to the L or X valley is much faster than the intravalley Fröhlich scattering. This is in good agreement with the recently determined ultrafast intervalley scattering time using 6 fs pulses [105]. In reference 105, the intervalley scattering rate in GaAs was determined to be approximately 20 fs. This was measured with lower photon energies ( $\sim 2$  eV) but at higher temperature (300 K) than ours. These two effects tend to cancel each other due to the decrease in the band gap at higher temperatures. If we use 200 fs as our intravalley scattering time, then we can expect the generation of  $\approx 20/(200 + 20)$  LO phonons per electron from the electrons which are excited from the light- and heavy-hole bands. Our results might not directly support the ultrafast intervalley scattering rates of reference 105. This is because the phonon production efficiency using 200 fs of electron-LO phonon interaction time might not be valid in this low density regime when the spatial coherence of the photoexcited electron-hole pair is most likely broken by the intervalley scattering. This is because the Fröhlich scattering time of 200 fs is for the electron, not for the electron-hole pair. The LO phonon emission by the

electron-hole pair before they lose their coherence is not well known.

Our results demonstrate that under certain experimental conditions (photon energy, carrier density, optical pulse duration) it is necessary to include photoexcited electrons from the split-off hole bands together with intervalley scattering in the analysis of time resolved Raman spectra. Since previous experiments have often excluded these effects those results may need reconsideration. For instance, in the analysis of the data in reference 96, both intervalley scattering and the split-off hole band contributions have been ignored, but the electron-phonon interaction time in this experiment is in good agreement with the theoretically predicted value. However, the 2 ps rise time of the anti-Stokes Raman signal might reflect the time constant for the L- $\Gamma$  scattering of the electrons at room temperature [103]. In a ps Raman scattering experiment used to determine the intervalley scattering rates in GaAs, the analysis excluded the electrons from the split-off hole bands [101]. The intervalley scattering rates were mainly determined by the reduction in the hot LO phonon production efficiency as the photon energy increased. This is because of the increasing intervalley scattering rates with larger carrier excess energies and populations. The pulse width in this experiment was about 4 ps, so the electrons returning to the  $\Gamma$  valley from the L and X valleys are an important source in generating the  $\Gamma$  valley Raman active hot phonons. Since the number and excess energy of electrons excited from the split-off hole band increases with increasing photon energy, the deformation potentials estimated in reference 101 are expected to be less than the real values. Since electrons in the  $\Gamma$ -valley thermalize very quickly, (within 100 fs with carrier

densities as low as  $10^{17} \text{ cm}^{-3}$ ) the instantaneous thermalization model is more appropriate than the cascade model for almost all excitation densities used in time resolved Raman experiments [102,103]. This is because in most of these experiments the rise time is typically 1-2 ps when optical pulses near 1 ps are used.

## CHAPTER V

### CONCLUSIONS

Optical properties of thin barrier GaAs/Al<sub>x</sub>Ga<sub>1-x</sub>As superlattice have been investigated using various spectroscopic techniques involving tunable dye lasers. These techniques include photoluminescence (PL), photoluminescence excitation (PLE), and resonant Raman scattering (RRS). A series of high quality MBE grown superlattices were designed with constant aluminum concentration and well widths, while the barrier widths varied. The sample parameters in this series were carefully chosen to study the effects of well-to-well coupling over the range from no coupling (isolated quantum wells) to very strong coupling (superlattice). This allowed for a systematic investigation of the effects of well-to-well coupling on excitonic spectra. One of the primary interests of this work is on the effects of subband dispersion which is a manifestation of the well-to-well coupling.

In chapter II, the effects of subband dispersion on excitonic line narrowing observed by PLE spectroscopy was presented. It was shown that the inhomogeneous line broadening mechanism caused by random monolayer fluctuations in the well and barrier widths had little to no effect in strongly coupled superlattices resulting in a dramatic exciton line narrowing with a decrease in the barrier width. Using a multiple scattering theory based on a Greens function technique in the coherent potential

approximation, the experimentally observed linewidths of the  $n=1$  heavy- (1HH) and light-hole (1LH) excitons were correctly predicted. This work demonstrated that the inhomogeneous broadening induced by the structural disorder associated with MBE growth was proportional to the combined electron and hole density of states. Since the density of states in a superlattice decreases with increasing subband dispersion, the effect of well-to-well coupling is to reduce inhomogeneous broadening caused by structural disorder.

In chapter III, the combined techniques of PL, PLE, and RRS were used to investigate properties associated with the combined subband structure of the  $n=1$  electron and hole states. It was shown that the near energetic overlap of the 1LH with the  $n=1$  heavy-hole subband in a thin barrier superlattice could result in a Fano-type resonance. The effect of this resonance together with subband dispersion was suggested to result in additional structure in photoluminescence spectra as well as a dramatic reduction in the 1LH exciton intensity relative to that of the 1HH exciton observed by PLE spectroscopy. In addition, multiple resonant Raman scattering allowed by the subband dispersion along the  $z$ -direction was used to describe the subband structure of the  $n=1$  electron, heavy- and light-hole states. The identification of the structures which appear in phonon assisted excitation spectra involved the unique properties of excitons, carriers, and phonons in coupled quantum well structures.

Finally, in chapter IV a picosecond Raman scattering technique was used to investigate the possibility of LO phonon localization in a wide range of  $\text{Al}_x\text{Ga}_{1-x}\text{As}$

alloys covering the entire direct band gap regime. It was shown that localization of LO phonons due to alloy potential fluctuations does not exist. Moreover, the importance of the split-off hole band and the initial relaxation of hot carriers in GaAs within the first few picoseconds after photoexcitation was thoroughly discussed. In particular, nearly all photoexcited carriers quickly transfer from the  $\Gamma$ -valley to the L and X satellite valleys where they remain. The only  $\Gamma$ -valley electrons capable of initial generation of hot LO phonons in GaAs originate from the split-off hole band.

## REFERENCES

1. E.O. Göbel, K. Ploog, *Prog. Quant. Electr.* **14**, 289 (1990).
2. L. Esaki, R. Tsu, *IBM J. Res. Develop.* **14**, 61 (1970).
3. F. Capasso, K. Mohammed, A.Y. Cho, *IEEE J. Quantum Electron.* **QE22**, 1853 (1986).
4. C. Weisbuch, R.C. Miller, R. Dingle, A.C. Gossard and W. Wiegmann, *Solid States Commun.* **37**, 219 (1981).
5. M. Tinkham, *Group Theory and Quantum Mechanics* (McGraw-Hill, New York, 1964).
6. *Landölt-Borstein*, edited by Madelung, New Series, Group 3, Vol. 22a (Springer, Berlin, 1988).
7. H.C. Casey Jr. and M.B. Panish, *Heterostructure Lasers* (Academic, New York, 1978).
8. D.S. Chemla, D.A.B. Miller, P.W. Smith, *Opt. Engng.* **24**, 556 (1985).
9. R. Dingle, W. Wiegmann, C.H. Henry, *Phys. Rev. Lett.* **33**, 827 (1974).
10. G. Bastard, J.A. Brum, R. Ferreira, *Solid State Physics* **44**, p.229, Eds. H. Ehrenreich, and D. Turnbull, Academic Press (1991).
11. G. Bastard, *Wave Mechanics Applied to Semiconductor Heterostructures*, Les Editions de Physique, Les Ulis, Halsted Press, New York, 1988.
12. H.I. Ralph, *Sol. Stat. Commun.* **3**, 303 (1965).
13. R.L. Greene, K.K. Bajaj, D.E. Phelps, *Phys. Rev. B* **29**, 1807 (1984).
14. A. Baldereschi, and N.C. Lipari *Phys. Rev. B* **3**, 439 (1971).
15. R.C. Miller, D.A. Kleinman, W.T. Tsang, A.C. Gossard, *Phys. Rev. B* **24**, 1134 (1981).

16. P. Dawson, K.J. Moore, G. Duggan, H.I. Ralph, C.T.B. Foxon, *Phys. Rev. B* **34**, 6007 (1986).
17. D.C. Reynolds, K.K. Bajaj, C. Leak, G. Peters, W. Theis, P.W. Yu, K. Alavi, C. Colvard, I. Shidlovsky, *Phys. Rev. B* **37**, 3117 (1988).
18. A. Chomette, B. Lambert, B. Deveaud, F. Clerot, A. Regreny, G. Bastard, *Europhys. Lett.* **4**, 461 (1987).
19. E.S. Koteles, J.Y. Chi, *Phys. Rev. B* **37**, 6332 (1988).
20. L.W. Molenkamp, G.E.W. Bauer, R. Eppenga, C.T. Foxon, *Phys. Rev. B* **38**, 6147 (1988).
21. K.J. Moore, G. Duggan, K. Woodbridge, C. Roberts, *Phys. Rev. B* **41**, 1090 (1990).
22. H. Chu, Y.C. Chang, *Phys. Rev. B* **36** 2946 (1987).
23. J.J. Song, P.S. Jung, Y.S. Yoon, H. Chu, Y.C. Chang, C.W. Tu, *Phys. Rev. B* **39**, 5562 (1989).
24. S. Hong and J. Singh, *J. Appl. Phys.* **62**, 1994 (1987).
25. A. Honold, L. Schultheis, J. Kuhl and C.W. Tu, *Phys. Rev. B* **40**, 6442 (1989).
26. H. Qiang, F.H. Pollak, C.M. Sotomayor Torres, W. Leitch, A.H. Kean, M.A. Stroscio, G.J. Iafrate, K.W. Kim, *Appl. Phys. Lett.* **61**, 1411 (1992).
27. D.F. Welch, G.W. Wicks and L.F. Eastman, *Appl. Phys. Lett.* **46**, 991, (1985).
28. J. Singh, K.K. Bajaj, S. Chaudhuri, *Appl. Phys. Lett.* **44**, 805 (1984).
29. J. Sing and K.K. Bajaj, *Appl. Phys. Lett.* **48**, 1077 (1986); *Appl. Phys. Lett.* **44**, 1075 (1984); *J. Appl. Phys.* **57**, 5433 (1985).
30. E.F. Schubert, E.O. Göbel, Y. Horikoshi, K. Ploog and H.J. Queisser, *Phys. Rev. B* **30**, 813 (1984).
31. C. Weisbuch, R. Dingle, A.C. Gossard and W. Wiegmann, *Solid State Commun.* **38**, 709 (1981).
32. B. Deveaud, J.Y. Emery, A. Chomette, B. Lambert, M. Baudet, *Superlattices and Microstructures* **1**, 205 (1985).



33. D.C. Reynolds, K.K. Bajaj, C.W. Litton, P.W. Yu, J. Singh, W.T. Masselink, R. Fischer and H. Morkoç, *Appl. Phys. Lett.* **46**, 51 (1985); *J. Vac. Sci. Technol. B* **3**, 1061 (1985).
34. C.A. Warwick, W.Y. Jan and A. Ourmazd, *Appl. Phys. Lett.* **56**, 2666 (1990).
35. R.F. Kopf, E.F. Schubert, T.D. Harris and R.S. Becker, *Appl. Phys. Lett.* **58**, 631 (1991).
36. M. Tanaka and H. Sakaki, *J. of Crystal Growth* **81**, 153 (1987).
37. C.W. Tu, R.C. Miller, B.A. Wilson, P.M. Petroff, T.D. Harris, R.F. Kopf, S.K. Sputz and M.G. Lamont, *J. of Crystal Growth* **81**, 159 (1987).
38. P.S. Jung, J.M. Jacob, J.J. Song, Y.C. Chang and C.W. Tu, *Phys. Rev. B* **40**, 6454 (1989).
39. J.J. Song, J.M. Jacob, J.F. Zhou, S.J. Hwang, P.S. Jung, Y.C. Chang and C.W. Tu, *SPIE Proceedings from the conference on Quantum Well and Superlattice Physics III*, **1263**, 344 (1990).
40. M. Krahl, J. Christen, D. Bimberg, G. Weimann and W. Schlapp, *Appl. Phys. Lett.* **52**, 798 (1988).
41. C. Weisbuch, R. Dingle, P.M. Petroff, A.C. Gossard and W. Wiegmann, *Appl. Phys. Lett.* **38**, 840 (1981).
42. H. Morkoç, T.J. Drummond and R. Fischer, *J. Appl. Phys.* **53**, 1030 (1982).
43. A. Ourmazd, D.W. Taylor, J. Cunningham and C.W. Tu, *Phys. Rev. Lett.* **62**, 933 (1989).
44. A. Ourmazd, W.T. Tsang, J.A. Rentschler and D.W. Taylor, *Appl. Phys. Lett.* **50**, 1417 (1987).
45. R.L. Greene and K.K. Bajaj, *Solid State Commun.* **45**, 831 (1983).
46. E.S. Koteles, D.A. Owens, D.C. Bertolet and K. M. Lau, *Phys. Rev. B* **38**, 10139 (1988).
47. J.N. Schulmann

48. R.J. Elliott, J.A. Krumhansl, and P.L. Leath, *Review of Mod. Phys.* **46**, 465 (1974).
49. G. Rickayzen in *Green's Functions and Condensed Matter*, Academic Press, London (1980).
50. P.L. Taylor in *A Quantum Approach to the Solid State*, Prentice Hall, Inc., New Jersey, (1970) pp. 283-310.
51. D.W. Taylor, *Phys. Rev.* **156**, 1017 (1967).
52. B. Velicky, S. Kirkpatrick, and H. Ehrenreich, *Phys. Rev.* **176**, 747 (1968).
53. P. Soven, *Phys. Rev.* **156**, 1017 (1967).
54. A.B. Chen, *Phys. Rev. B* **7**, 2230 (1973).
55. K. Huang, B. Zhu, and H. Tang, *Phys. Rev. B* **41**, 5825 (1990).
56. G. Wen and Y.C. Chang, *Phys. Rev. B* **45**, 13562 (1992).
57. W. Kauschke, A.K. Sood, M. Cardona, and K. Ploog, *Phys. Rev. B* **36**, 1612 (1987).
58. A.K. Sood, J. Menéndez, M. Cardona, and K. Ploog, *Phys. Rev. Lett.* **54**, 2111 (1985).
59. D. Olego and M. Cardona, *Solid Stat. Comm.* **39**, 1071 (1981).
60. B. Zhu, K. Huang, and H. Tang, *Phys. Rev. B* **40**, 6299 (1989).
61. J.E. Zucker, A. Pinczuk, D.S. Chemla, A. Gossard and W. Wiegmann, *Phys. Rev. Lett.* **51**, 1293 (1983).
62. C. Trallero-Giner, A. Cantarero, M. Cardona, and M. Mora, *Phys. Rev. B* **45**, 6601 (1992).
63. N. Kobayashi, T. Toriyama, and Y. Horikoshi, *Appl. Phys. Lett.* **50**, 1811 (1987).
64. J. E. Zucker, A. Pinczuk, D.S. Chemla, A. Gossard, and W. Wiegmann, *Phys. Rev. Lett.* **53**, 1280 (1984).

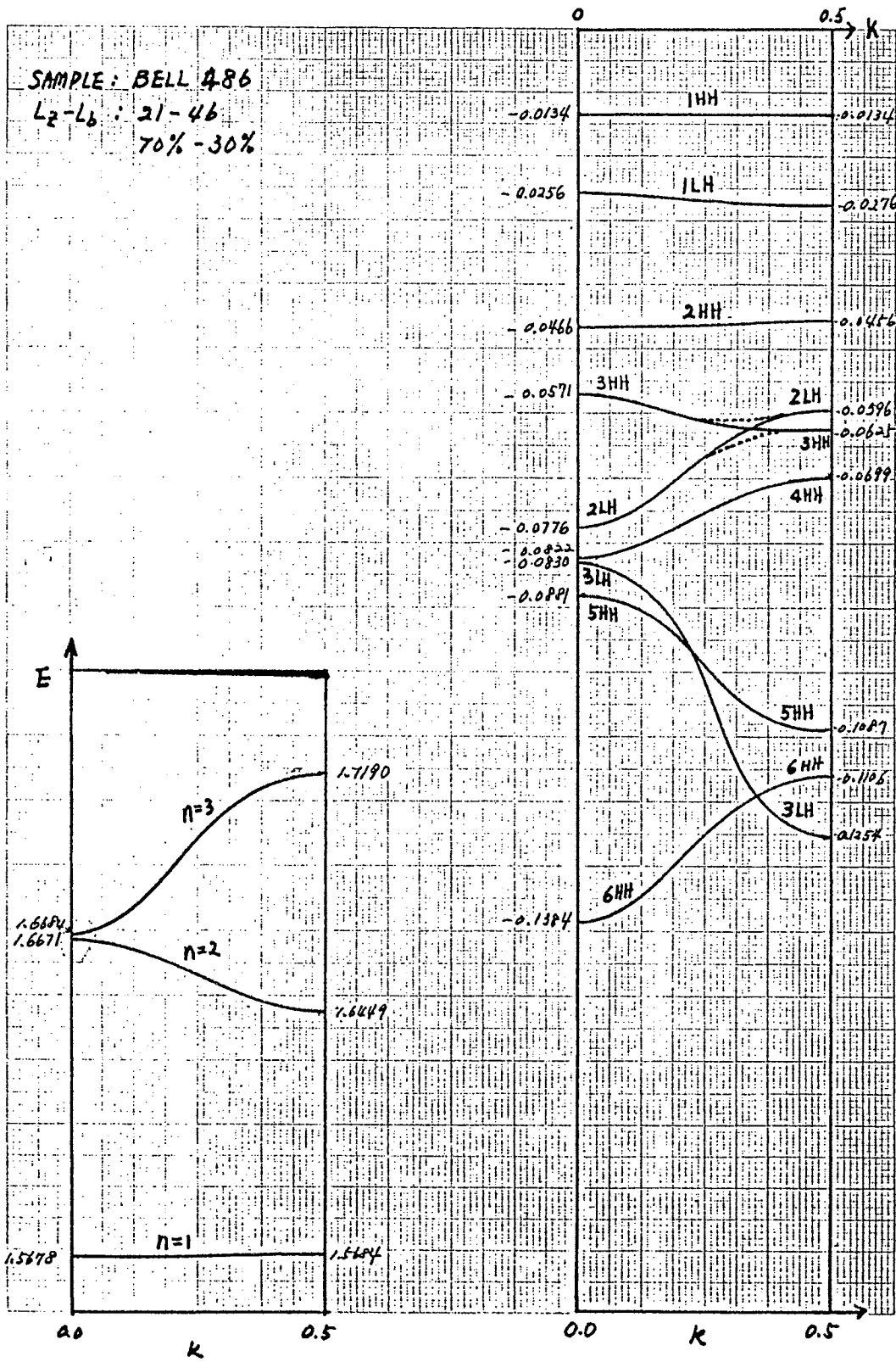
65. A.J. Shields, M. Cardona, R. Nötzel, and K. Ploog, Phys. Rev. B **46**, 10490 (1992).
66. A.A. Gogolin and E.I. Rashba, Solid Stat. Commun. **19**, 1177 (1976).
67. A.K. Sood, J. Menéndez, M. Cardona, and K. Ploog, Phys. Rev. Lett. **54**, 2115 (1985).
68. A. Alexandrou, M. Cardona, and K. Ploog, Phys. Rev B **38**, 2196 (1988).
69. D.A. Kleinman, R.C. Miller, and A.C. Gossard, Phys. Rev. B **35**, 664 (1987).
70. R.C. Miller, D.A. Kleinman, C.W. Tu, and S.K. Sputz, Phys. Rev. B **34**, 7444 (1986).
71. R.C. Miller, D.A. Kleinman, and A.C. Gossard, Soli. Stat. Commun. **60**, 213 (1986).
72. A.K. Sood, J. Menéndez, M. Cardona, and K. Ploog, **32**, 1412 (1985).
73. Y. Liu, R. Sooryakumar, E.S. Koteles, and B. Elman, Phys. Rev. B **43**, 6832 (1991).
74. A. Alexandrou and M. Cardona, Soli. Stat. Commun. **64**, 1029 (1987).
75. J. Menéndez, J. of Luminescence **44**, 285 (1989); M.V. Klein, IEEE J. Quant. Electron. **QE-22**, 1760 (1986); M. Cardona, Superlattices and Microstructures **5**, 27 (1989).
76. G. Weber, Phys. Rev. B **46**, 16171 (1992).
77. see references in OSU physics department qualifying exam of J.M. Jacob (1993).
78. D.S. Kim, A. Bouchalkha, J.M. Jacob, J.F. Zhou, and J.J. Song, Phys. Rev. Lett. **68**, 1002 (1992).
79. J.J. Song, J.F. Zhou, and J.M. Jacob in *Semiconductor Interfaces and Microstructures*, edited by Z.C. Feng, World Scientific, Singapore (1992) pp. 63-92.
80. U. Fano, Phys. Rev. **124**, 1866 (1961).
81. A. Pasquarello and L.C. Andreani, Phys. Rev. B **44**, 3162 (1991).

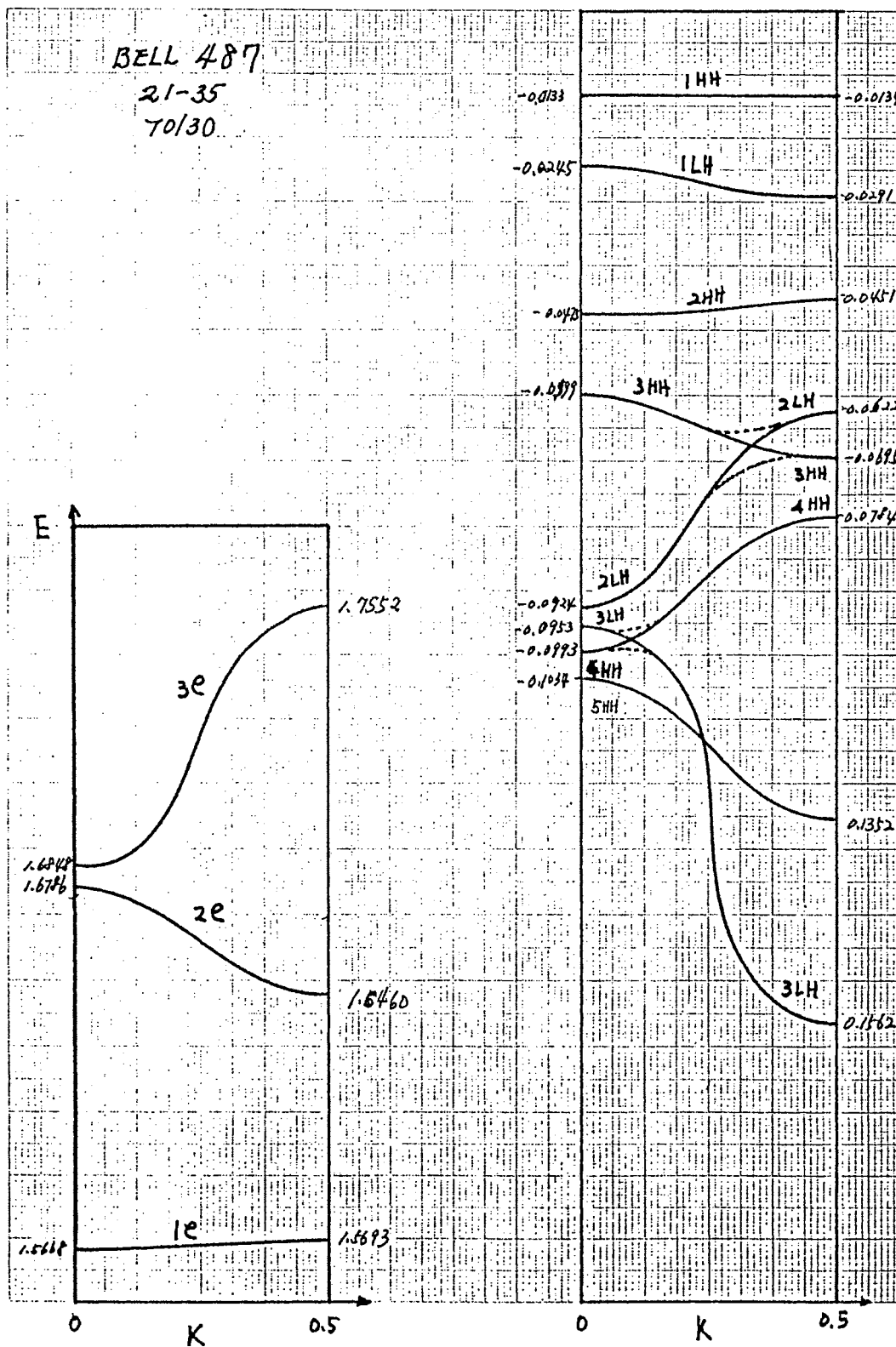
82. A. Hanold, T. Saku, Y. Horikoshi, and K. Köhler, *Phys. Rev. B* **45**, 6010 (1992).
83. A. Amith, *Phys. Rev.* **139**, A1624 (1965).
84. A.K. Saxena, *Phys. Rev. B* **24**, 3295 (1981).
85. A.K. Saxena and A.R. Adams, *J. Appl. Phys.* **58**, 2640 (1985).
86. P. Parayanthal and F.H. Pollak, *Phys. Rev. Lett.* **52**, 1822 (1984).
87. J.A. Kash, J.M. Hvam, J.C. Tsang, and T.F. Kuech, *Phys. Rev. B* **38**, 5776 (1988).
88. B. Jusserand, D. Paquet, and F. Mollot, *Phys. Rev. Lett.* **63**, 2397 (1989).
89. S. Baroni, S de Gironcoli, and P. Giannozzi, *Phys. Rev. Lett.* **65**, 84 (1990).
90. B. Jusserand, F. Mollot, L.C. Quagliano, G.L. Roux, and R. Planel, *Phys. Rev. Lett.* **67**, 2803 (1991).
91. J.A. Kash, S.S. Jha, and J.C. Tsang, *Phys. Rev. Lett.* **58**, 1869 (1987).
92. D.S. Kim and P.Y. Yu, in *Proceedings of SPIE Symposium on Ultrafast Laser Probe Phenomena in Bulk and Microstructure Semiconductors*, edited by R. R. Alfano (SPIE-The International Society for Optical Engineering, Bellingham, Washington, 1990), Vol.1282, p. 39.
93. D.S. Kim, A. Bouchalkha, J.M. Jacob, J.F. Zhou, and J.J. Song, *Phys. Rev. Lett.* **68**, 1002 (1992).
94. J.L. Birman, M. Lax, and R. Loudon, *Phys. Rev.* **145**, 620 (1966).
95. C.L. Collins and P.Y. Yu, *Phys. Rev. B* **30**, 4501 (1984).
96. J.A. Kash, J.C. Tsang, and J.M. Hvam, *Phys. Rev. Lett.* **54**, 2151 (1985).
97. M.C. Tatham, J.F. Ryan, and C.T. Foxon, *Phys. Rev. Lett.* **63**, 1637 (1989).
98. K.T. Tsen and H. Morkoç, *Phys. Rev. B* **38**, 5615 (1988).
99. D.Y. Oberli, D.R. Wake, M.V. Klein, J. Henderson, and H. Morkoç, *Phys. Rev. Lett.* **59**, 696 (1987).

100. D.S. Kim and P.Y. Yu, Phys. Rev. Lett. **64**, 946 (1990).
101. D.S. Kim and P.Y. Yu, Appl. Phys. Lett. **56**, 1570 (1990).
102. T. Elsaesser, J. Shah, L. Rota, and P. Lugli, Phys. Rev. Lett. **66**, 1757 (1991).
103. J. Shah, B. Deveaud, T.C. Damen, W.T. Tsang, A.C. Gossard, and P. Lugli, Phys. Rev. Lett. **59**, 2222 (1987).
104. D.J. Erskine, A.J. Taylor, and C.L. Tang, Appl. Phys. Lett. **45**, 54 (1984).
105. Y. -Y. Bigot, M.T. Portella, R.W. Schoenlein, J.E. Cunningham, and C.V. Shank, Phys. Rev. Lett. **65**, 3429 (1990).
106. N.C. Miller, S. Zemon, G.P. Werber, and W. Powazinik, J. Appl. Phys. **57**, 512 (1985).
107. D.S. Kim and P.Y. Yu, Appl. Phys. Lett. **56**, 2210 (1990).
108. D. Von der Linde, Phys. Rev. Lett. **44**, 1505 (1980).
109. K.T. Tsen and H. Morkoç, Phys. Rev. B **26**, 4770 (1982).
110. M.J. Rosker, F.W. Wise, and C.L. Tang, Appl. Phys. Lett. **49**, 1726 (1986).
111. P. Pearah, W.T. Masselink, J. Klem, T. Henderson, and H. Morkoç, Bull. Am. Phys. Soc. **30**, 604 (1985).
112. S. Zollner, S. Gopalan, and M. Cardona, J. Appl. Phys. **68**, 1682 (1990).
113. D.S. Kim, J.M. Jacob, J.F. Zhou, J.J. Song, H. Hou, C.W. Tu, and H. Morkoç, Phys. Rev. B **45**, 13973 (1992).
114. D.S. Kim and P.Y. Yu, Phys. Rev. B, **43**, 4158 (1991).
115. H.C. Casey Jr. and M.B. Panish, *Heterostructure Lasers*, Part A, (Academic Press, New York, 1978).
116. N. Lifshitz, A. Jayaraman, and R.A. Logan, Phys. Rev. B **21**, 670 (1980).
117. E.O. Kane, J. Phys. Chem. Solids, 249, (1957).
118. W.W. Rühle, K. Leo, and E. Bauser, Phys. Rev. B. **40**, 1756 (1989).

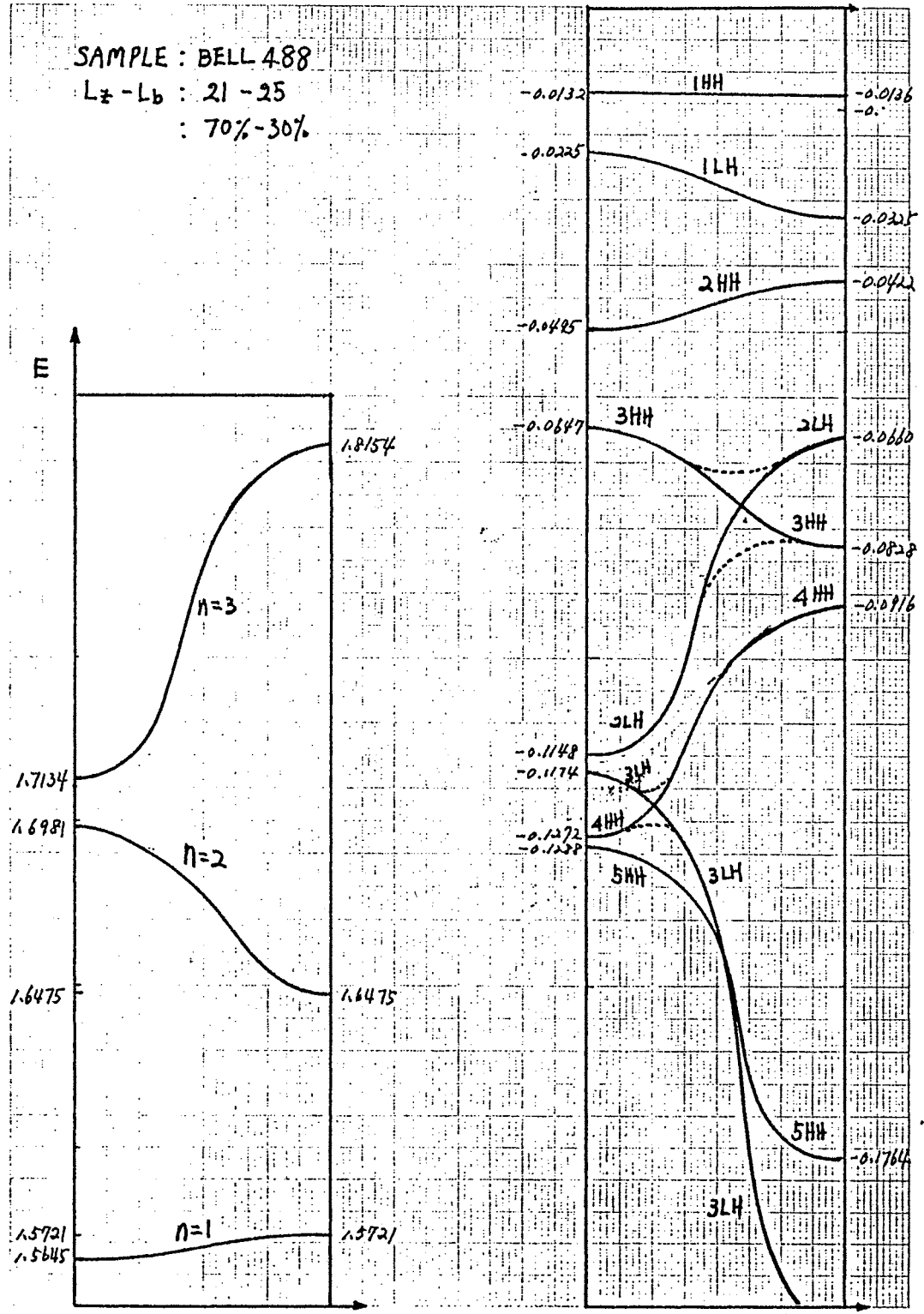
## APPENDIX A

### CALCULATED SUBBAND STRUCTURES FOR THE SERIES OF SUPERLATTICES STUDIED

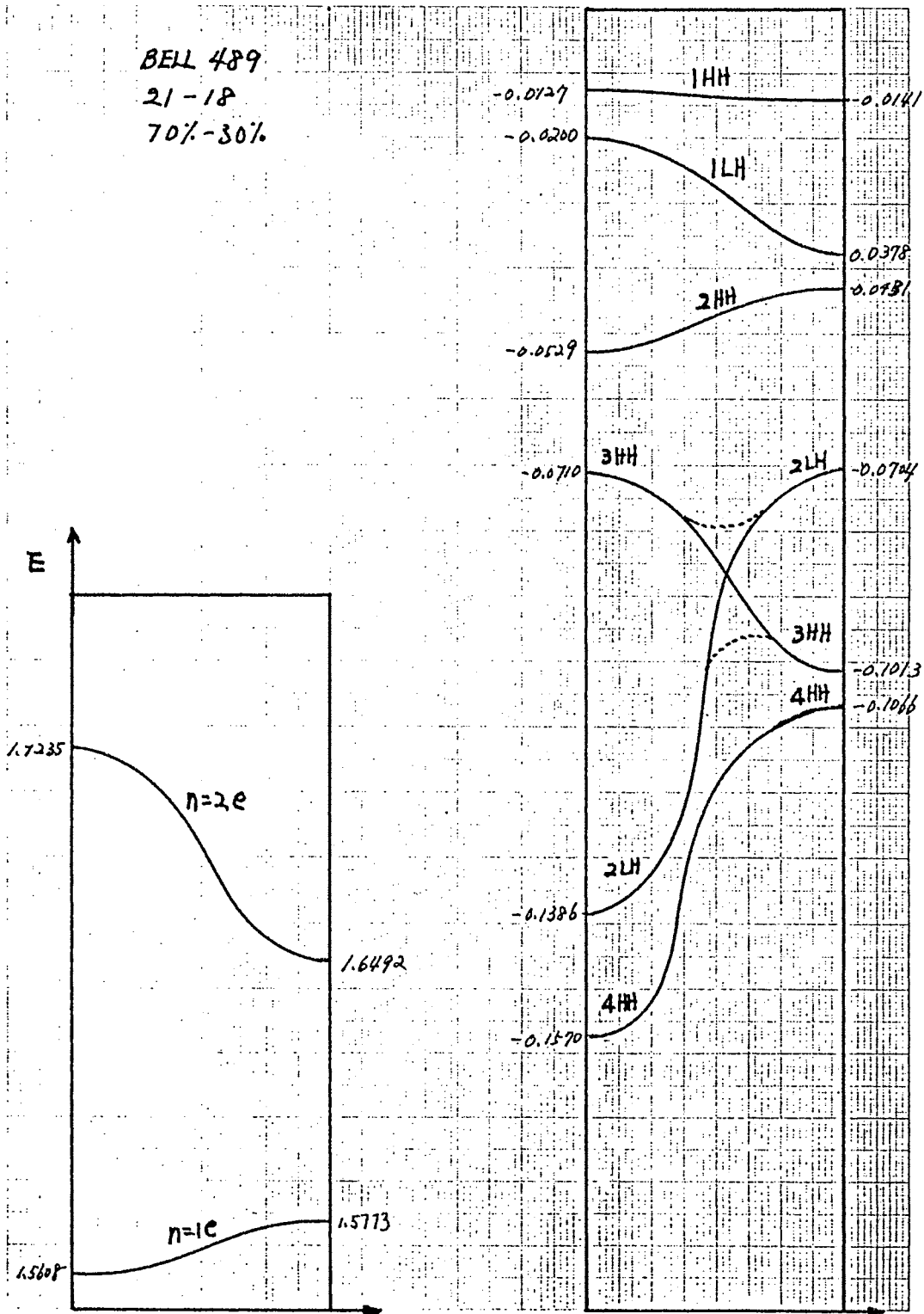


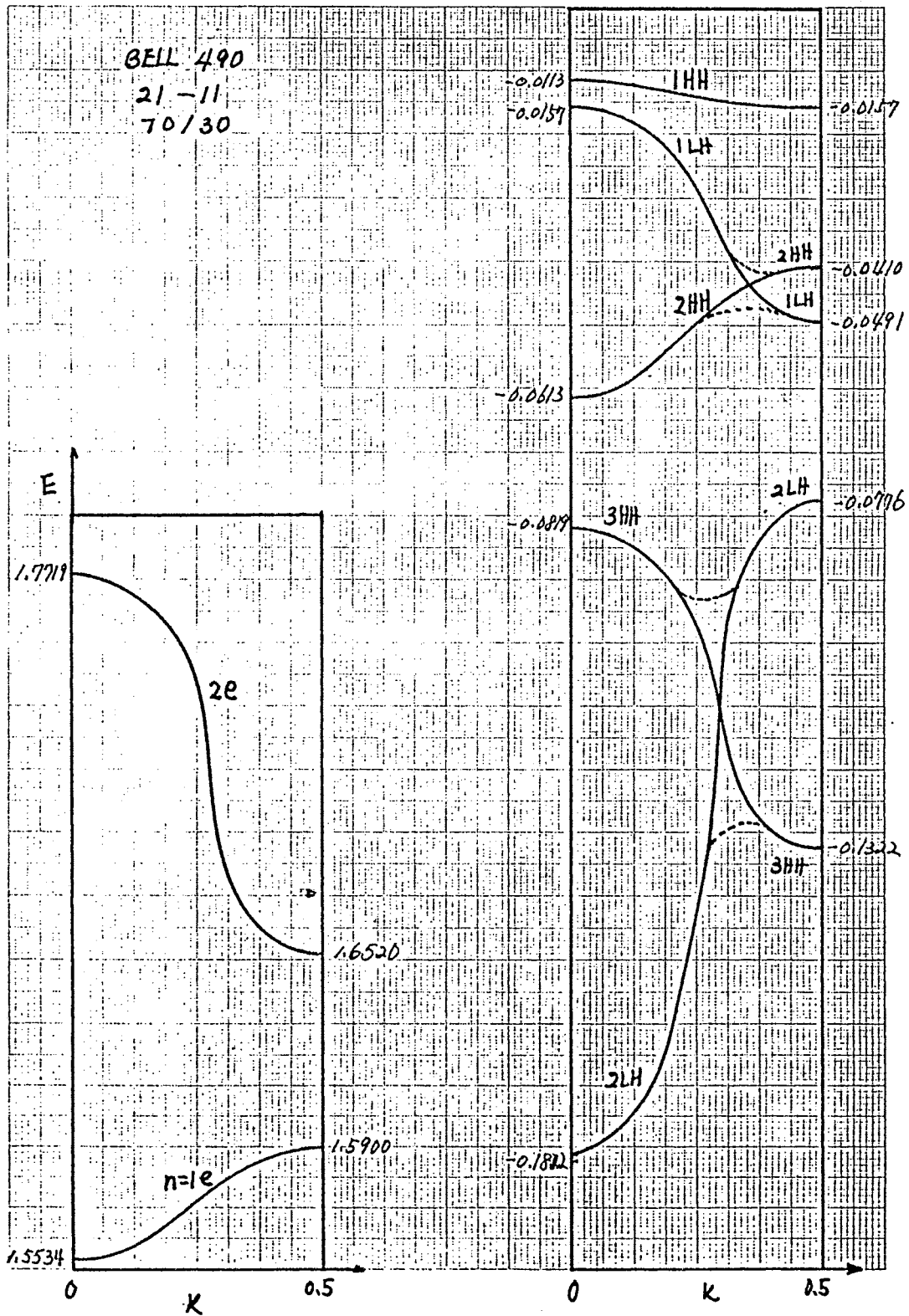






BELL 489  
 21-18  
 70%-30%





## APPENDIX B

### PROGRAM SOURCE CODE FOR HOT

### PHONON GENERATION IN

### Al<sub>x</sub>Ga<sub>1-x</sub>As ALLOYS.

```
program HOTPHONON (input,output);

{Calculates the hot phonon occupation number assuming that the electrons}
{instantaneously thermalize to a Boltzman distribution.}
{Considers only those electrons which originate from the}
{split-off hole band.}
{Takes into account nonparabolicity of the gamma valley conduction band.}

CONST  A = 0.577; B = 0.047;

VAR  dNq,no,pw,ti,q,xi,ex,di,int,FE1,FE2,E,FE,Nq,FET,kT,dn,Ep,Em,CE,CEp: real;
      CEm,Is,Ias,Eg,NNq,GE,GEEm,GEp,GE1,GEml,GEpl,fEp,fEn,DE,I1,I2:real;
      FE3,FE4,FE5,FE6,FE7,FE8:real;

      n,dnn,nn:array[0..500] of real;

      i,j,k,l,dt,En:integer;

      any:char;

begin
  writeln ('What is the total electron density?');
  readln (no);
  no:=no * 0.25; {Approx. 25% of total electron density comes from SOH band}
  writeln ('What is the FWHM of the laser pulse?');
  readln (pw);
  writeln ('What is the time interval of this calculation (fs)?');
  readln (ti);
  writeln ('What is the q-vector used in this calculation?');
  readln (q);

  {Determine the Gamma valley excess energy and AlGaAs band gap for different x}

  for i:= 0 to 9 do begin
    xi:= i * 0.04;
    if i=0 then ex:= 0.301;
    if i=1 then ex:= 0.267;
    if i=2 then ex:= 0.246;
    if i=3 then ex:= 0.216;
    if i=4 then ex:= 0.188;
    if i=5 then ex:= 0.162;
    if i=6 then ex:= 0.127;
    if i=7 then ex:= 0.093;
    if i=8 then ex:= 0.061;
    if i=9 then ex:= 0.040; {The actual value is 0.030 but I used}
                           {0.040 for calculation purposes.}
  end
end
```

```

kT:= (2/3)*ex; Eg:= 1.519 + 1.247 * xi;

{Calculate the total area under a Sech(x) squared pulse shape.}

int:= 0;
for dt:= trunc(-pw/ti) to trunc(pw/ti) do begin
  di:= 0.315/(exp(3.52*dt*ti/pw) + exp(-3.52*dt*ti/pw) + 2);
  int:= int + di;
end;

{Determine the chemical potential by integrating the product}
{of the density of states and Boltzman distribution using}
{Simpsons rule.}

FE1:=0; FE2:=0;

E:=(1/100)*(2*En);
FE:= (1 + 2*A*E + 3*B*E*E)*sqrt(E + A*E*E + B*E*E*E)*exp(-E/kT);
FE1:= FE1 + FE;
end;
for En:=1 to 99 do begin
  E:=(1/100)*(2*En);
  FE:= (1 + 2*A*E + 3*B*E*E)*sqrt(E + A*E + B*E*E)*exp(-E/kT);
  FE2:= FE2 + FE;
end;
FET:= (1/600)*(4*FE1 + 2*FE2);
WRITELN ("FET=" ,FET);

{Calculate the contribution of the electron density in the gamma valley}
{from each time interval of the pulse.}

for j:=0 to 500 do begin
  n[j]:= 0; dnn[j]:= 0; nn[j]:= 0;
end;
for dt:= trunc(-pw/ti) to trunc(pw/ti) do begin
  j:= trunc(pw/ti) + dt + 1;
  dn:= (no/int)*(0.315/(exp(3.52*dt*ti/pw) + exp(-3.52*dt*ti/pw) + 2)
);
  n[j]:= dn;
end;

{Determine the Gamma valley electron density at a given time which reflects}
{emission and absorption of hot phonons.}

FE3:= 0; FE4:= 0; nn[1]:=n[1];k:=0;
for k:= 1 to 2*trunc(pw/ti) + 1 do begin;
  for En:= 1 to 90 do begin
    E:=(1/100)*(2*En-1) + 0.037; Ep:= E + 0.037; Em:= E - 0.037;
    CE:=sqrt(1-0.5*(1+0.5*Eg/sqrt(0.5*Eg*Eg + E*51.4)));
    CEm:=sqrt(1-0.5*(1+0.5*Eg/sqrt(0.5*Eg*Eg + Em*51.4)));
    CEp:=sqrt(1-0.5*(1+0.5*Eg/sqrt(0.5*Eg*Eg + Ep*51.4)));
    GE:= E + A*E*E + B*E*E*E;
    GE1:= 1 + 2*A*E + 3*B*E*E;
    fEp:= nn[k]*exp(-Ep/kT)/(FET*5.98E25);
    fEn:= nn[k]*exp(-E/kT)/(FET*5.98E25);
    GEp:= Ep + A*Ep*Ep + B*Ep*Ep*Ep;
    GEp1:= 1 + 2*A*Ep + 3*B*Ep*Ep;
    GEm:= Em + A*Em*Em + B*Em*Em*Em;
    GEm1:= 1 + A*Em*2 + B*Em*Em*3;
    DE:= 1.107E37*GE1*sqrt(GE)*1.602E-19*sqrt(1.602E-19);
    FE:= 294.29/(sqrt(1.602E-19))*sqrt(1/GE)*(GEp1*fEp*
ln((sqrt(GEp) + sqrt(GE))/(sqrt(GEp) - sqrt(GE)))*
(1 - (CE*CEm)/ln((sqrt(GEp) + sqrt(GE))/(sqrt(GEp) - sqrt(GE)))) -
GEm1*fEn*ln((sqrt(GE) + sqrt(GEm))/(sqrt(GE) - sqrt(GEm))))*
(1 - (CE*CEm)/ln((sqrt(GE) + sqrt(GEm))/(sqrt(GE) - sqrt(GEm)))))))*DE;
    FE3:=FE3 + FE;
  end;
end;

```

```

for En:= 1 to 89 do begin
  E:=(1/100)*(2*En) + 0.037; Ep:= E + 0.037; Em:= E - 0.037;
  CE:=sqrt(1-0.5*(1+0.5*Eg/sqrt(0.5*Eg*Eg + E*51.4)));
  CEm:=sqrt(1-0.5*(1+0.5*Eg/sqrt(0.5*Eg*Eg + Em*51.4)));
  CEp:=sqrt(1-0.5*(1+0.5*Eg/sqrt(0.5*Eg*Eg + Ep*51.4)));
  GE:= E + A*E*E + B*E*E*E;
  GE1:= 1 + 2*A*E + 3*B*E*E;
  fEp:= nn[k]*exp(-Ep/kT)/(FET*5.98E25);
  fEn:= nn[k]*exp(-E/kT)/(FET*5.98E25);
  GEp:= Ep + A*Ep*Ep + B*Ep*Ep*Ep;
  GEp1:= 1 + 2*A*Ep + 3*B*Ep*Ep;
  GEm:= Em + A*Em*Em + B*Em*Em*Em;
  GEm1:= 1 + 2*A*Em + 3*B*Em*Em;
  DE:= 1.107E37*GE1*sqrt(GE)*1.602E-19*sqrt(1.602E-19);
  FE:= 294.29/(sqrt(1.602E-19))*sqrt(1/GE)*(GEp1*fEp*
ln((sqrt(GEp) + sqrt(GE))/(sqrt(GEp) - sqrt(GE))))*
(1 - (CE*CEm)/ln((sqrt(GE) + sqrt(GEm))/sqrt(GE) - sqrt(GE)))) -
GEm1*fEn*ln((sqrt(GE) + sqrt(GEm))/sqrt(GE) - sqrt(GEm))))*
(1 - (CE*CEm)/ln((sqrt(GE) + sqrt(GEm))/sqrt(GE) - sqrt(GEm)))))*DE;
  FE4:= FE4 + FE;
end;
dnn[k]:= 1/600*(4*FE3 + 2*FE4)*ti;
nn[k+1]:= dnn[k] + nn[k] + n[k+1];
end;

{Calculate Nq by integrating dNq/dt from Eq1 to infinity using simpsons rule.}

FE5:=0; FE6:=0; Nq:=0; FE7:=0; FE8:=0;
for l:= 1 to (2*trunc(pw/ti) + 1) do begin
  for En:= 1 to 100 do begin
    E:= (2*En/100) + 0.14;
    Em:= E - 0.037;
    FEn:= (nn[l]*exp(-E/kT))/(FET*5.98E25);
    GE1:= 1 + 2*A*E + 3*B*E*E;
    GEm1:= 1 + 2*A*Em + 3*B*Em*Em;
    FE:= (1.08E33*1.602E-19)/(q*q*q)*GEm1*GE1*FEn*1E25;
    FE5:= FE + FE5;
  end;
  for En:= 1 to 99 do begin
    E:= (2*En - 1)/100 + 0.14;
    Em:= E - 0.037;
    FEn:= (nn[l]*exp(-E/kT))/(FET*5.98E25);
    GE1:= 1 + 2*A*E + 3*B*E*E;
    GEm1:= 1 + 2*A*Em + 3*B*Em*Em;
    FE:= (1.08E33*1.602E-19)/(q*q*q)*GEm1*GE1*FEn*1E25;
    FE6:= FE + FE6;
  end;
  I1:= (1/600)*(4*FE5 + 2*FE6);
  for En:= 1 to 100 do begin
    E:= (1/100)*2*En + 0.14;
    Em:= E - 0.037;
    CE:= sqrt(1 - (0.5*Eg)/sqrt((0.5*Eg*Eg) + (E*51.4)));
    CEm:= sqrt(1 - (0.5*Eg)/sqrt((0.5*Eg*Eg) + (Em*51.4)));
    GE:= E + A*E*E + B*E*E*E;
    GEm:= Em + A*Em*Em + B*Em*Em*Em;
    GE1:= 1 + 2*A*E + 3*B*E*E;
    GEm1:= 1 + 2*A*Em + 3*B*Em*Em;
    FEn:= (nn[l]*exp(-E/kT))/(FET*5.98E25);
    FE:= (3.595E22/q)*((GEm1*GE1)/(sqrt(GEm)*sqrt(GE)))*CE*CEm*FEn;
    FE7:= FE + FE7;
  end;

```

```

for En:= 1 to 99 do begin
  E:=(1/100)*(2*En-1) + 0.14;
  Em:= E - 0.037;
  CE:= sqrt(1 - (0.5*Eg)/sqrt((0.5*Eg*Eg) + (E*51.4)));
  CEm:= sqrt(1 - (0.5*Eg)/sqrt((0.5*Eg*Eg) + (Em*51.4)));
  GE:= E + A*E*E + B*E*E*E;
  GEm:= Em + A*Em*Em + B*Em*Em*Em;
  GE1:= 1 + 2*A*E + 3*B*E*E;
  GEm1:= 1 + 2*A*Em + 3*B*Em*Em;
  FEn:=(nn[1]*exp(-E/kT)/(FET*5.98E25));
  FE:= (3.595E22/q)*((GEm1*GE1)/(sqrt(GEm)*sqrt(GE)))*CE*CEm*FEn;
  FE8:= FE + FE8;
end;
I2:= (1/600)*(4*FE7 + 2*FE8);
dNq:= (I1 - I2)*ti*1E-10;
Nq:= Nq + dNq;
end;

writeln ('Nq= ',Nq);
writeln ('dnn= ',dnn[(2*trunc(pw/ti) + 1)]);
writeln ('n= ',nn[(2*trunc(pw/ti)+1)]);
end;
end.

```

2

VITA

JOHN MATTHEW JACOB

Candidate for the degree of

Doctor of Philosophy

Thesis: OPTICAL PROPERTIES OF THIN BARRIER GaAs-Al<sub>x</sub>Ga<sub>1-x</sub>As  
SUPERLATTICES

Major Field: Physics

Biographical:

Personal Data: Born in Bogalusa, Louisiana, February 14, 1965, the son of Roy A. and Gerri K. Jacob.

Education: Graduated from Lake Hamilton high School, Percy, Arkansas, May, 1983; received Bachelor of Art Degree in physics from Hendrix college, Conway, Arkansas, May, 1987; completed the requirements for Doctor of Philosophy Degree at Oklahoma State University, Stillwater, Oklahoma, July, 1993.